

2. EXPLANATORY NOTES¹

Shipboard Scientific Party²

OPERATIONS

Site Locations

At all Leg 202 sites, Global Positioning System (GPS) coordinates from precruise site surveys were used to position the vessel on site. The only seismic system used during the leg was the 3.5-kHz profiler, which was monitored on the approach to each site to compare the seismic characteristics of the sediments with those from the precruise survey. Once the vessel was positioned at a site, the thrusters were lowered and a reference beacon was deployed. Although the automated station keeping system of the vessel usually uses GPS data, the beacon provides a backup reference in case of problems with the transmission of satellite data. The final site position was the mean position calculated from the GPS data collected over the time that the site was occupied. At the end of operations at a site, the beacon was retrieved and the thrusters were retracted before the vessel proceeded to the next site at full speed.

Drilling Operations

Two coring systems were used during Leg 202: the advanced piston corer (APC) and the extended core barrel (XCB). The APC is a “cookie-cutter” type system that cuts cores with minimal coring disturbance. The drill pipe is pressured up until the failure of one or two shear pins that hold the inner barrel attached to the outer barrel. The inner barrel strikes out and cuts the core. The driller can detect a successful cut, or “full stroke,” on the pressure gauge on the rig floor. Whenever possible, the APC was used because it yields the least disturbed cores.

When “APC refusal” occurs in a hole before the target depth is reached, the XCB is used to advance the hole. The XCB is a rotary system with a small cutting shoe that extends below the large rotary bit.

¹Examples of how to reference the whole or part of this volume.

²Shipboard Scientific Party addresses.

The smaller bit can cut a semi-indurated core with less torque and fluid circulation than the main bit and thus optimizes recovery. If the formation becomes even more indurated, the rotary core barrel (RCB), which is the most conventional drilling system, is used but was not needed on Leg 202.

Both the APC and XCB systems use the same bottom-hole assembly (BHA), and switching from one to the other does not require a pipe trip. The standard BHA used at all Leg 202 sites comprised an 11⁷/₁₆-in APC/XCB rotary bit, a bit sub, a seal bore drill collar, a landing saver sub, a modified top sub, a modified head sub, a nonmagnetic drill collar, five 8¼-in drill collars, a tapered drill collar, six joints of 5½-in drill pipe, and one crossover sub. A lockable float valve was used instead of the standard float assembly if the possibility of logging existed.

APC refusal is conventionally defined in two ways: (1) the piston fails to achieve a complete stroke (as determined from the pump pressure reading) because the formation is too hard and (2) excessive force (>60 klb) is required to pull the core barrel out of the formation. In the case where full stroke can be achieved but excessive force cannot retrieve the barrel, the core barrel can be “drilled over” (i.e., after the inner core barrel is successfully shot into the formation, the rotary bit is advanced to total depth in order to free the APC barrel). This strategy allows a hole to be advanced much farther with the APC, the favorite drilling tool. A total of 101 core barrels were drilled over during Leg 202, which is a record number for one leg.

Each cored interval was about 9.5 m long, which is the length of a core barrel. In some cases, the drill string was drilled or “washed” ahead without recovering sediments to advance the drill bit to a target depth where core recovery needed to be resumed. Such advances were necessary in multiple holes at a site to ensure that coring gaps in one hole were covered by cored intervals in adjacent holes. The amount of advance was typically 1–4 m and accounted for drilling depth shift caused by tides, heave, and other factors (see also “[Composite Section](#),” p. 4).

Drilled and cored intervals are referred to in meters below rig floor (mbrf), which are measured from the dual elevator stool (DES) on the rig floor to the bottom of the drill pipe. In the case where sediments of substantial thickness cover the seafloor (as at all sites during Leg 202), the mbrf depth of the seafloor is determined with a mudline core, assuming 100% recovery for the cored interval in the first core. If the first core recovered a full barrel of sediment (it “missed the mudline”), the seafloor reference depth of a previous or later hole was used. Water depth was calculated by subtracting the distance between the DES and sea level (typically 10–11 m, depending on a ship’s load at a given time) from the mbrf depth. The water depth determined in this way (drill string measurement) usually differs from precision depth recorder measurements by a few to several meters. The meters below seafloor (mbsf) depths of core tops are calculated by subtracting the seafloor depth in mbrf from the core top depth in mbrf. The core top datums from the driller are the ultimate depth reference for any further depth calculation procedures.

Core Handling and Analysis

As soon as cores arrived on deck, gas void samples and headspace samples were taken by means of a syringe, if applicable, for immediate analysis as part of the shipboard safety and pollution prevention program. Core catcher samples were taken for biostratigraphic analysis.

When the core was cut in sections, whole-round samples were taken for shipboard interstitial water examinations. In addition, headspace gas samples were immediately taken from the ends of cut sections and sealed in glass vials for light hydrocarbon analysis.

Before splitting, whole-round core sections were run through the multisensor track (MST) and thermal conductivity measurements were taken. The cores were then split into working and archive halves, from bottom to top, so investigators should be aware that older material could have been transported upward on the split face of each section. The working half of each core was sampled for both shipboard analysis (i.e., physical properties, carbonate, and bulk X-ray diffraction mineralogy) and shore-based studies. Shipboard sampling was kept at a minimum during Leg 202 to allow construction of a detailed sampling plan after the composite section was built (see “[Composite Section](#),” p. 4). The archive half sections were scanned on the digital imaging system (DIS), measured for color reflectance on the archive multisensor track (AMST), described visually and by means of smear slides, run through the cryogenic magnetometer, and finally photographed with both black-and-white and color film a whole core at a time. Close-up photographs were taken of particular features for illustrations in site summary reports, as requested by scientists.

Both halves of the core were then put into labeled plastic tubes, sealed and transferred to cold storage space aboard the ship. The last few hundred meters of core were stored in the unrefrigerated hold because we ran out of refrigerated space. At the end of the leg, the cores were transferred from the ship into refrigerated trucks and to cold storage at the Gulf Coast Core Repository of the Ocean Drilling Program (ODP) in College Station, Texas.

Curatorial Procedures and Sample Depth Calculations

Numbering of sites, holes, cores, and samples followed the standard ODP procedure. A full curatorial identifier for a sample consists of the following information: leg, site, hole, core number, core type, section number, and interval in centimeters measured from the top of the core section. For example, a sample identification of “202-1239A-1H-1, 10–12 cm” would represent a sample removed from the interval between 10 and 12 cm below the top of Section 1 of Core 1 (H designates that this core was taken with the APC system) of Hole 1239A during Leg 202.

Cored intervals are also referred to in “curatorial” mbsf. The mbsf of a sample is calculated by adding the depth of the sample below the section top and the lengths of all higher sections in the core to the core top datum measured with the drill string. A soft to semisoft sediment core from less than a few hundred meters below seafloor expands upon recovery (typically 10%–15%), so the recovered interval does not match the cored interval. In addition, a coring gap typically occurs between cores, as shown by composite depth construction (see “[Composite Section](#),” p. 4) (i.e., some cored interval was lost during recovery or was never cut). Thus, a discrepancy exists between the drilling mbsf and the curatorial mbsf. For instance, the curatorial mbsf of a sample taken from the bottom of a core is larger than that from a sample from the top of the subsequent core, where the latter does correspond to the drilled core top datum.

During Leg 202, multiple APC holes (typically three) were drilled at a site to construct a continuous composite section. This resulted in a

“meters composite depth” scale for each site that accommodates core expansion and drilling gaps through interhole correlation of closely spaced measurements of core physical properties (see “[Composite Section](#),” p. 4).

COMPOSITE SECTION

Stratigraphers have demonstrated that a continuous sedimentary section is rarely recovered from a single ODP borehole because core-recovery gaps occur between successive APC and XCB cores despite 100% or more nominal recovery (Ruddiman et al., 1987; Hagelberg et al., 1995). Construction of a complete section, referred to as a splice, requires combining stratigraphic intervals from two or more holes cored at the same site. To maximize the probability of bridging core-recovery gaps in successive holes, the depths below the seafloor from which cores are recovered are offset between the holes. This practice ensures that most inter-core intervals missing within a given hole are recovered in at least one of the adjacent holes. On Leg 202, we found that two complete holes and a third partial hole were usually needed to recover a complete section in the APC portion of a site.

Our composite section and splice construction methodology follows one which has been successfully employed during a number of legs (e.g., Hagelberg et al., 1992; Curry, Shackleton, Richter, et al., 1995; Jansen, Raymo, Blum, et al., 1996; Lyle, Koizumi, Richter, et al., 1997; Gersonde, Hodell, Blum, et al., 1999, Wang, Prell, Blum, et al., 2000). The construction and verification of a complete composite stratigraphic section requires the construction of a variety of depth scales (Table T1) that are described below.

Composite Depth Scale

Before a splice can be constructed, the cores from the various holes must be stratigraphically correlated with each other. Such correlation enables development of a composite depth scale referred to as meters composite depth (mcd). This mcd scale differs from the traditional (hole specific) depth scale, called the meters below seafloor (mbsf) scale. The latter is based on the length that the drill string is advanced on a core-by-core basis but may be inaccurate because of ship heave (which is not compensated for in APC coring), tidal variations in sea level, and other sources of error. In contrast, the mcd scale is built by assuming that the uppermost sediment (commonly referred to as the mudline) in the first core from a given hole is the sediment/water interface. This core becomes the “anchor” in the composite depth scale and is typically the only one in which depths are the same on both the mbsf and mcd scales. From this anchor, core logging data are correlated among holes downsection. For each core, a depth offset (a constant) that best aligns the observed lithologic variations to the equivalent cores in adjacent holes is added to the mbsf depth in sequence down the holes.

Depth offsets are often chosen to optimize correlation of specific features that define splice levels in cores from adjacent holes. In a few cases (e.g., Site 1233), we constructed an alternate (secondary) splice to accommodate high-resolution sampling. Such secondary splices require the definition of secondary mcd scales to optimize splice levels. When calculating mcd of samples, it is important to use the composite depth scale that is compatible with the splice.

T1. Depth scales used to construct composite sections, p. 65.

The length of the mcd scale at a given site is typically ~10% to 20% greater than the length of the cored section in any one hole as indicated by the mbsf scale. This expansion is commonly attributed to sediment expansion resulting from elastic rebound, stretching during the coring process, gas expansion during the core recovery process, and other factors (e.g., Moran, 1997).

Composite Depth Construction

For Leg 202, the mcd scale and the splice are based on the stratigraphic correlation of data from the whole-core Oregon State University (OSUS) Fast Track (hereafter referred to as Fast Track), the MST, and the AMST. Core-logging data were collected at 2.5-, 5-, or 10-cm intervals. We used magnetic susceptibility (the data are referred to as OSUS-MS if collected using the Fast Track or MST-MS if collected using the MST), gamma ray attenuation (GRA) bulk density, natural gamma radiation (NGR), and reflectance (L^* , a^* , and b^*). All of these measurements are described in “**Physical Properties**,” p. 16.

The raw stratigraphic data were imported into the shipboard Splicer software program (version 2.1) and culled as necessary to avoid incorporating anomalous data influenced by edge effects at section boundaries. Splicer was used to assess the stratigraphic continuity of the recovered sedimentary sequences at each drill site and to construct the mcd scale and splice. Splicer enables the construction of a composite depth scale for each hole at a given site by depth-shifting individual cores to maximize the correlation of core logging data.

Because depth intervals within cores are not squeezed or stretched by Splicer, all correlative features cannot be aligned. Stretching or squeezing between cores from different holes may reflect small-scale differences in sedimentation and/or distortion caused by the coring and archiving processes. The tops of APC cores are generally stretched and the bottoms compressed, although this is lithology dependent. In addition, sediment (especially unconsolidated mud, ash, sand, and gravel) occasionally falls from higher levels in the borehole onto the tops of cores as they are recovered, and as a result the top 20–100 cm of many cores is not reliable.

Correlations among cores from adjacent holes are evaluated visually and statistically (by cross-correlation within a 2-m depth interval). Depth-shifted data are denoted by mcd. A table is presented in each site chapter that summarizes the depth offsets for each core. These tables are necessary for converting mbsf to mcd scales. The mcd for any point within a core equals the mbsf plus the cumulative offset. Correlation at finer resolution is not possible with Splicer since depth adjustments are applied linearly to individual cores; no adjustments, such as squeezing and stretching, are made within cores. Such fine-scale adjustment is possible postcruise (e.g., Hagelberg et al., 1995).

Ideally, the base of the mcd scale is the bottom of the deepest core recovered from the deepest hole (e.g., Site 1233). In practice, however, the base often occurs where core recovery gaps align across all holes or the data quality does not allow reliable correlations between holes. Cores below this interval cannot be directly tied into the overlying and continuous mcd. However, below the base of the continuous mcd, cores from two or more holes can sometimes be correlated with each other (e.g., Site 1234) to create a floating splice. At other sites, we used the observation that the differential depth offset within the correlated interval was relatively constant (i.e., the growth in the cumulative offset, the

difference between mbsf and mcd for a particular core, was linear) to assign cores below the splice a depth offset (e.g. Site 1238) by extrapolation using a growth factor (GF). GF is defined as the ratio of apparent length of sediment (using the mcd scale) to the drilled interval, as $mcd/mbsf$, within a defined interval. This extrapolation strategy was adopted when three conditions were met. First, the correlated interval represented at least one-half of the drilled interval. Second, the spliced interval had a linear growth in cumulative offset. Third, the entire sediment section had a shared lithology, because we found that lithology tended to determine the size of coring offset and associated change in GF. If any of these conditions was not met, then an mcd was assigned to the section below the splice by adding the greatest cumulative offset to the first core below the splice and, working downhole, appending cores using the drilled interval if recovery was 100% or the recovered interval if recovery was >100% (e.g., Site 1232).

Corrected Composite Depth

We also provide corrected meters composite depth (cmcd) in our depth conversion tables. This scale is intended to correct the mcd scale for empirically observed core expansion. A cmcd datum is produced by dividing mcd by GF over a sufficiently long interval so that random variations in drill pipe advance due to ship heave, tides, and other factors are negligible. This operation produces a complete stratigraphic sequence that is the same length as the total depth cored. The cmcd scale is a close approximation of the actual drilling depth scale. Because the cmcd scales are not archived in the Janus database, in most cases we found it most practical to plot data on the mcd scale and to correct linear sedimentation rates (LSRs) and mass accumulation rates (MARs) by dividing by the average GF within each interval.

Splice

The splice is a composite core section representing the complete stratigraphy at a site. It is composed of core sections from adjacent holes so that coring gaps in one hole are filled with core intervals from an adjacent hole. The splice does not contain coring gaps, and an effort has been made to minimize inclusion of disturbed sections. The shipboard splice is ideally suited to guide core sampling for detailed paleoceanographic studies. A table and a figure are presented in each site chapter that summarize the intervals from each hole used to construct the splice. Additional splices may be constructed postcruise as needed. (e.g., Site 1233).

The choice of tie points (and hence of a splice) is a somewhat subjective exercise. Our method in the construction of a splice followed three rules. First, where possible we avoided using the top and bottom 1 m of cores, where disturbance resulting from drilling artifacts (even if not apparent in core logging data) was most likely. Second, we attempted to incorporate those realizations of the stratigraphic section that were most representative of the holes recovered. Third, we tried to minimize tie points in order to simplify sampling.

Core-Log Integration

At Sites 1238, 1239, and 1241, logging operations produced data sets that were of sufficient quality to allow for core-log integration. Log data

are provided with a depth scale referred to as meters logging depth (mld). This depth scale is constructed using the time at which the logging tool is raised from the bottom of the hole, the rate at which it is raised, and the time at which it crosses the sediment/water interface. Core-log integration produces yet another depth scale, estimated log depth (eld). This depth scale is constructed by correlating physical properties measurements of cores made using the MST with those made in the drill hole using logging tools. This depth scale has the advantage of correcting for stretching and squeezing within cores. It has the disadvantage of typically beginning at ~100 mbsf, where the drill pipe is positioned during logging operations. Where available and where logging data are of sufficient quality, eld is the best estimate of in situ depth and so is ideal for calculating MARs.

To determine eld, logging and whole-core MST data were imported into the Sagan software package (version 1.2) and culled and smoothed as necessary to ensure that bad data were not included in the integration (see explanation in the Splicer discussion in [“Composite Depth Construction,”](#) p. 5) and that the log and core data were compatible. Because core logging data, in general, have a higher resolution than downhole log data, it is necessary to smooth the core logs before comparing them with downhole logs. Sagan allows the correlation of individual cores within different holes with the data series recovered from logging. We used NGR and GRA bulk density measurements made in the borehole and in the laboratory for core-log comparison. Sagan allows the user to shift depths and to linearly stretch or squeeze the entire recovered sequence and then to shift depth, and to stretch or squeeze individual cores in user-defined increments until acceptable core-log integration is established. We attempted, whenever possible, to minimize the number of tie points used to tie a single core to the log. For sites where core-log integration was attempted (Sites 1238 and 1239), we provide supplementary data files, which are Sagan eld tables (see the [“Supplementary Material”](#) contents list). These tables, when loaded into Sagan, allow the user to assign eld to any sample(s) with a previously assigned mcd or mbsf.

Fast Track

The use of the Fast Track was a major innovation during Leg 202. Because throughput on the track was extremely high (15 min per core in its fastest mode or 45 min per core in high-resolution mode), it was able to keep pace with most drilling operations and thus allowed for real-time evaluation of the position of coring gaps in the composite section. This helped us to make rapid drilling adjustments aimed at ensuring the recovery of a complete stratigraphic section. It also allowed us to run the MST at a slower rate, to optimize data quality (longer measurement time yielding greater analytic precision and, in many cases, higher depth resolution) because we did not need its data to assess recovery of a complete section at most sites. We recommend a second whole-core measurement track optimized for speed of analysis on future high-recovery paleoceanographic legs. Ideally, this track would have a magnetic susceptibility and a GRA densitometer so that the data type most appropriate to the sedimentary setting could be utilized.

micrite, or other authigenic components, the 10%–25% abundance range would be acknowledged by using the suffix “with.” For example, an unconsolidated sediment containing 45% nannofossils, 30% clay minerals, 10% micrite, 10% foraminifers, and 5% feldspar would be described as a foraminifer-bearing clayey nannofossil ooze with micrite. Although sedimentary components ranging from 10%–25% are reflected in the sediment name in the description column as “-bearing,” these components are not designated in the graphic lithology column. These naming conventions follow the ODP sediment classification scheme of Mazzullo et al. (1988) with the exception that during Leg 202 a separate “mixed sediment” category was not distinguished. Chemical sediments generally were not encountered during Leg 202 except as accessory minerals and nodules, and therefore, this category is not addressed below. Micrite, which may be formed by local recrystallization or by precipitation from solution, was frequently encountered during Leg 202 and is included below within the discussion of nonpelagic carbonates and authigenic minerals.

Granular sediments were subdivided on the basis of composition and abundance of different grain types estimated from visual examination of the core, smear slides, thin sections, and by shipboard measurements of carbonate content (see “**Sedimentary Inorganic Carbon and Organic Carbon, Nitrogen, and Sulfur Concentrations,**” p. 34) and shipboard X-ray diffraction (XRD) analyses. Sediments containing >50% silt- and sand-sized volcanic grains were classified as ash layers. Larger volcanic clasts (breccia) were not encountered except as fragments of basalt at or near the base of drilled sections. Size divisions for grains are those of Wentworth (1922) (Fig. F2). Size-textural qualifiers were not used for pelagic sediment names (e.g., nannofossil clay implies that the dominant component is detrital clay, rather than clay-sized nannofossils).

Grain Types

Grain types in granular sediments and rocks were classified according to depositional origin and mineralogy: (1) pelagic calcareous, (2) pelagic siliceous, (3) nonpelagic calcareous, and (4) siliciclastic particles. Their definitions are as follows:

1. Pelagic grains are fine-grained skeletal debris produced within the upper part of the water column in open-marine environments by
 - a. Calcareous microfauna and microflora (foraminifers, pteropods, and nannofossils and associated organisms) and
 - b. Siliceous microfauna and microflora (radiolarians and diatoms and associated organisms).

2. Nonpelagic grains are particles deposited in hemipelagic and periplatform environments and consist of the following:
 - a. Calcareous skeletal and nonskeletal grains and fragments (e.g., bioclasts, peloids, and micrite) (note that the term “micrite” is used to define fine calcareous particles (<30 μm) of indeterminate origin; such particles can be either recrystallized nannofossils or nonpelagic bank-derived calcareous mud in pelagic lithologies);

F2. Grain size divisions for sedimentary rocks, p. 52.

Millimeter (mm)	Microcentimeter (μm)	Phi (φ)	Wentworth size class	Rock type
4000	—	—	Boulder	Conglomerate Breccia
200	—	—	Subboulder	
64	—	—	Subgranule	
4	—	—	Granule	
—	250	—	Very coarse sand	Sandstone
—	150	—	Coarse sand	
10	—	—	Medium sand	
1/4	—	—	Fine sand	
1/8	—	—	Very fine sand	Siltstone
1/16	—	—	Coarse silt	
1/32	—	—	Medium silt	
1/64	—	—	Fine silt	
1/128	—	—	Very fine silt	Claystone
1/256	—	—	Very coarse clay	
1/512	—	—	Coarse clay	
1/1024	—	—	Fine clay	
—	0.0006	—	Clay	Claystone
—	0.0002	—	Very fine clay	

- b. Siliciclastic grains comprising minerals and rock fragments of terrigenous origin that were eroded from plutonic, sedimentary, and metamorphic rocks; and
- c. Siliceous clastic grains comprising glass shards, rock fragments, and mineral crystals that were produced by volcanic processes.

Granular Sediment and Rock Classification Scheme

Variations in the relative proportions of the five grain types described above define four major classes of granular sediments and rocks: calcareous and siliceous pelagic, nonpelagic calcareous, siliciclastic, and mixed.

Pelagic sediments and rocks contain 60% or more pelagic grains and 40% or less nonpelagic calcareous and siliciclastic grains. Nonpelagic calcareous sediments and rocks include 60% or more nonpelagic calcareous grains and 40% or less pelagic plus nonpelagic siliciclastic grains. Siliciclastic sediments and rocks are composed of 60% or more siliciclastic grains and 40% or less pelagic plus nonpelagic calcareous grains. For mixtures of pelagic and nonpelagic calcareous grains, we used the classification scheme of Dunham (1962) (Fig. F3). For mixtures of siliciclastic, biogenic, and other sediments, we followed the procedures outlined in Table T2.

Principal Names

Sediments and rocks were named solely on the basis of composition and texture. Within each class, granular sediments and rocks were classified using a principal name and major and minor modifiers. Principal names define the degree of consolidation (firmness) and granular sediment class. Composition is the most important classifier for pelagic and siliciclastic sediments and rocks (Table T2), whereas texture is more significant for the classification of nonpelagic calcareous sediments and rocks (Fig. F3).

Compositions and textures of cored sediments and rocks were determined on board ship by (1) unaided visual observation, (2) visual observation using a hand lens, and (3) visual estimates in smear slides, and coarse fractions were verified with the aid of a microscope. Calcium carbonate content was estimated qualitatively in smear slides and quantitatively by coulometric analysis (see “Geochemistry,” p. 32). Selected samples were also examined in thin section and by XRD.

Firmness

Firmness of recovered materials was defined as in Gealy (1971). Three classes of firmness were used to describe calcareous sediments and rocks:

Unlithified: soft sediments that have little strength and are readily deformed under the pressure of a fingernail or the broad blade of a spatula. This corresponds to the term “ooze” for pelagic calcareous sediments. In nonpelagic calcareous sediments, the modifier “unlithified” is used (e.g., unlithified packstone).

Partly lithified: firm but friable sediments that can be scratched with a fingernail or the edge of a spatula blade. The term “chalk” is used for firm or friable pelagic calcareous material. In nonpel-

F3. Limestone classification, p. 53.

Abitronous limestones: Original components not organically bound during deposition					
Less than 10% grains >2 mm			More than 10% grains >2 mm		
Contains lime mud (<30 µm)		No lime mud			
Mud supported		Grain supported		Matrix supported	
>10% grains 0.03-2.0 mm	<10% grains 0.03-2.0 mm			Grain (>2 mm) supported	
Mudstone	Wackestone	Packstone	Grainstone	Floatstone	Rudstone

T2. Sediment nomenclature, Leg 202, p. 66.

agic calcareous sediment, the modifier “partially lithified” is used (e.g., partially lithified grainstone).

Lithified: hard, nonfriable cemented rock, difficult or impossible to scratch with a fingernail or the edge of a spatula. The term “limestone” (lithified ooze) is used for pelagic calcareous material. In nonpelagic calcareous material, a modified Dunham (1962) classification (see “**Nonpelagic and Mixed Pelagic and Nonpelagic Calcareous Sediments and Rocks,**” p. 11) is used.

Two classes of firmness were used to describe siliciclastic sediments and rocks:

Soft: Sediment core can be split with a wire cutter. Soft terrigenous sediment, pelagic clay, and transitional calcareous sediments are termed sand, silt, or clay.

Hard: The core is hard (i.e., consolidated or well indurated) if it must be cut with a hand or diamond saw. For these materials, the suffix “-stone” is added to the soft-sediment name (e.g., sandstone, siltstone, and claystone). Note that this varies from terms used to described nonpelagic calcareous sediments, for which the suffix “-stone” has no firmness implications.

Pelagic Sediments and Rocks

Principal names used to describe pelagic sediments and rocks from Leg 202 are as follows:

1. Pelagic clay: unconsolidated authigenic pelagic material (>15%) and siliceous pelagic sediment (lithified examples are termed “pelagic claystone”);
2. Ooze: unconsolidated calcareous and/or siliceous pelagic sediment;
3. Chalk: firm pelagic sediment composed predominantly of calcareous pelagic grains;
4. Limestone: hard pelagic sediment composed predominantly of calcareous pelagic grains; and
5. Chert: vitreous or lustrous, conchoidally fractured, highly indurated rock composed predominantly of authigenic silica.

Nonpelagic and Mixed Pelagic and Nonpelagic Calcareous Sediments and Rocks

Nonpelagic calcareous sediments and rocks were classified using a modification of the original Dunham (1962) classification in conjunction with depositional textures described by Embry and Klovan (1971) (Fig. F3):

1. Mudstone: mud-supported fabric with <10% grains and grains <2 mm in size;
2. Wackestone: mud-supported fabric with >10% grains and grains <2 mm in size;
3. Packstone: grain-supported fabric with intergranular mud and grains <2 mm in size;
4. Grainstone: grain-supported fabric with no mud and grains <2 mm in size;
5. Floatstone: matrix-supported fabric with grains >2 mm in size;

6. Rudstone: grain-supported fabric with grains >2 mm in size;
7. Boundstone: components organically bound during deposition;
8. Bafflestone: formed by organisms that act as baffles;
9. Bindstone: formed by organisms that encrust and bind; and
10. Framestone: formed by organisms that build a rigid framework.

Sediments and rocks that consist of a mixture of pelagic and nonpelagic calcareous grains and contain aragonite and/or magnesian calcite (confirmed by XRD analysis) were (1) described lithologically using the classification scheme explained above for nonpelagic calcareous sediments and rocks and (2) labeled additionally as periplatform oozes and periplatform chalks (e.g., Schlager and James, 1978).

Siliciclastic Sediments and Rocks

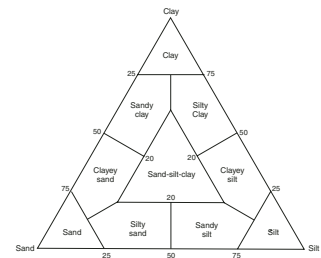
For siliciclastic sediments and rocks, texture is the main criterion for the selection of a principal name. The Udden-Wentworth grain-size scale (Wentworth, 1922) (Fig. F2) defines the grain-size ranges and the names of the textural groups (gravel, sand, silt, and clay) and subgroups (fine sand, coarse silt, etc.). When two or more textural groups or subgroups are present, the principal names appear in order of increasing abundance. Eight major textural categories can be defined on the basis of the relative proportions of sand, silt, and clay (Fig. F4). Distinguishing between some size categories is difficult (e.g., silty clay and clayey silt) without accurate measurements of weight percentages. The terms “conglomerate” and “breccia” are the principal names of gravels with well-rounded and angular clasts, respectively.

Major and Minor Modifiers

To describe the lithology of the granular sediments and rocks in greater detail, the principal name of a granular-sediment class is preceded by major modifiers and followed by minor modifiers (Table T2). Minor modifiers are preceded by the term “-bearing.” The most common uses of major and minor modifiers are to describe the composition and textures of grain types that are present in major (25%–40%) and minor (10%–25%) proportions in addition to the principal sediment. In addition, major modifiers can be used to describe grain fabric, grain shape, and sediment color. The composition of pelagic grains can be described in greater detail with the major and minor modifiers “nannofossil,” “foraminifer,” “calcareous,” and “siliceous.” The terms “calcareous” and “siliceous” are used to describe sediments that are composed of calcareous or siliceous pelagic grains of uncertain origin. The compositional terms for nonpelagic calcareous grains include the following major and minor modifiers as skeletal and nonskeletal grains:

1. Bioclast (or bioclastite): fragment of skeletal remains (specific names, such as “molluscan” or “algal,” also can be used);
2. Ooid (or oolite): spherical or elliptical nonskeletal particles <2 mm in diameter, having a central nucleus surrounded by a rim with concentric or radial fabric;
3. Pisolite: spherical or ellipsoidal nonskeletal particle, commonly >2 mm in diameter, with or without a central nucleus but displaying multiple concentric layers of carbonate;
4. Pellet (-al): fecal particles from deposit-feeding organisms;
5. Peloid (pel-): micritized carbonate particle of unknown origin;

F4. Siliciclastic textural classification, p. 54.



6. Intraclast: reworked carbonate sediment/rock fragment or rip-up clast consisting of the same lithology as the host sediment;
7. Lithoclast: reworked carbonate-rock fragment consisting of a different lithology than the host sediment; and
8. Calcareous, dolomitic, aragonitic, sideritic: the mineral composition of carbonate muds or mudstones (micrite) of nonpelagic origin.

The textural designations for siliciclastic grains utilize standard major and minor modifiers, such as “gravel(-ly),” “sand(-y),” “silt(-y),” and “clay(-ey).” The character of siliciclastic grains can be described further by mineralogy using modifiers such as “quartz,” “feldspar,” “glauconite,” “mica,” “lithic,” or “calcareous.”

Sediment Core Description

Preparation of Surfaces of Core Halves

The standard method of splitting cores by pulling a wire lengthwise through the center tends to smear the cut surface of soft sediments and obscure fine details of lithology and sedimentary structure. When necessary during Leg 202, specific intervals of the archive halves of cores were carefully scraped with a stainless steel or glass scraper to prepare the surface for unobscured sedimentologic examination and digital imaging. Scraping was done parallel to bedding with a freshly cleaned tool to prevent cross-stratigraphic contamination.

Sediment Barrel Sheets

Detailed sedimentologic observations and descriptions were recorded by hand for individual cores using handwritten visual core description (VCD) sheets. These observations were synthesized for each core in the computer-formatted sediment core description forms (Fig. F5) (AppleCORE “barrel sheets”). Exceptions to the standard ODP conventions adopted by the Leg 202 Scientific Party are described in the following sections.

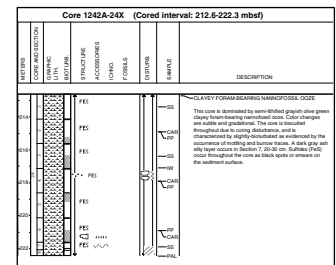
Lithologic Description Text

The lithologic description that appears on each core description form (barrel sheet) consists of two parts: (1) a heading that lists the major sediment lithologies observed in the core and (2) a more detailed description of the sediments, including location in the core of significant features. Descriptions and locations of thin, interbedded, or minor lithologies, color, samples, coring conditions, and so on, are included in the text.

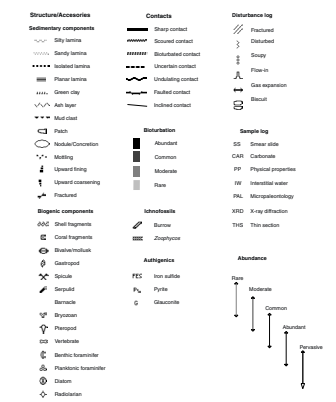
Graphic Lithology Column

Sediment types determined from the above classification scheme are represented graphically in the “Graphic Lithology” column of the barrel sheets using the symbols illustrated in Figure F6. A maximum of three different lithologies (for interbedded sediments) or three different components (for mixed sediments) can be represented within the same core interval. Minor lithologies present as thin interbeds within the major lithology are shown by a dashed vertical line dividing the litholo-

F5. Example of an AppleCORE barrel sheet, p. 55.



F6. Key to symbols on the barrel sheet, p. 56.



gies. Percentages are rounded to the nearest 10%, and lithologies that constitute <10% of the core are generally not shown but are listed in the “Lithologic Description” section. In some cases (e.g., distinctive ash layers) individual occurrences of minor lithologies are included graphically in the lithology column. Intervals that are a few centimeters or greater in thickness can be portrayed accurately in this column. Contact types (e.g., sharp, scoured, and gradational) are also shown within the “Graphic Lithology” column.

Bioturbation

Visible bioturbation was classified into five intensity levels based on the degree of disturbance of the physical sedimentary structures (Fig. F6):

1. Absent: no bioturbation; all physical sedimentary structures are preserved.
2. Rare: isolated trace fossils; up to 10% of physical sedimentary structures are disrupted.
3. Moderate: ~10%–40% disrupted physical sedimentary structures; burrows are generally isolated but may overlap locally.
4. Common: ~40%–60% bioturbated; only the last vestiges of physical sedimentary structures are discernible.
5. Abundant: bedding completely disturbed; burrows are still intact in places.

These categories are based on the five ichnofossil indices (ii1–ii5) of Droser and Bottjer (1986) and are illustrated with graphic symbols in the “Bioturbation” column. Visual recognition of bioturbation was often limited in homogeneous sediments, particularly in very dark siliciclastic clays and white calcareous oozes.

Sedimentary Structures

The locations and types of sedimentary structures visible on the prepared surface of the archive half of cores are shown in the “Structure” column of the core description form. The column is divided into three vertical areas for symbols. The symbols on the left side of the “Structure” column indicate the bedding characteristics (including color banding) of the sediment. We followed a slightly amended version of McKee and Weir (1953) to distinguish thicknesses of bedding units, whether identified by composition, texture, or color. Stratigraphic units are very thick bedded (or banded) if >100 cm in thickness, thick bedded (30–100 cm), medium bedded (10–30 cm), and thin bedded (<10 cm) in thickness. Finer millimeter-scale layers were described as laminae, although they were only rarely encountered during Leg 202. The abundance of visually detectable bioturbation is shown in the central portion of the “Structure” column of the barrel sheet as described above. The symbols on the left side of the “Structure” column indicate the location of individual bedding features and any other sedimentary features such as scours and ash layers, ripple laminations, ichnofossils, or shell fragments. Lithologic accessories in the center portion include diagenetic features such as nodules and sulfides. Fossils, shell fragments, and ichnofossils are included on the right side. The symbols used to designate the structures found in Leg 202 are shown in Figure F6.

Sediment Disturbance

Drilling-related sediment disturbance that persists over intervals of ~20 cm or more is recorded in the “Disturbance” column using the symbols shown in Figure F6. The degree of drilling disturbance is described for soft and firm sediments using the following categories:

1. Slightly disturbed: Bedding contacts are slightly deformed.
2. Moderately disturbed: Bedding contacts have undergone extreme bowing.
3. Highly disturbed: Bedding is completely deformed as flow-in, coring/drilling slough, and other soft sediment stretching and/or compressional shearing structures attributed to coring/drilling. The particular type of deformation may also be noted (e.g., flow-in, gas expansion, etc.).
4. Soupy: Intervals are water saturated and have lost all aspects of original bedding.

The degree of fracturing in indurated sediments and igneous rocks is described using the following categories:

1. Slightly fractured: core pieces in place and broken.
2. Moderately fractured: core pieces are in place or partly displaced, and original orientation is preserved or recognizable (drilling slurry may surround fragments, that is, drilling/coring “biscuits” are evident).
3. Highly fractured: core pieces are probably in correct stratigraphic sequence (although they may not represent the entire sequence), but original orientations are lost.
4. Drilling breccia: the core is crushed and broken into many small and angular pieces, with original orientation and stratigraphic position lost; often drilling breccia is completely mixed with drilling slurry.

Samples

The positions of samples taken from each core for analysis are indicated by letters in the “Sample” column of the core description form as follows: SS (smear slide), PAL (micropaleontology), CAR (carbonate), PP (physical properties), XRD (X-ray diffraction), THS (thin section), and IW (interstitial water). In most cases, samples were coordinated to provide data from the same horizon. Typically, CAR and PP samples were taken at 74–76 cm in each section of cores from the first long hole at each site, typically hole “A.” Smear slides were also generally taken at 75 cm in Sections 1 and 3 in the archive half of these cores, and additional SS samples were taken in order to capture the range of lithologies present.

Color

The color of the sediments was determined qualitatively using Munsell Color Company (1994) soil color charts and rock color charts (Rock-Color Chart Committee, 1991). When portions of the split core surface required cleaning with a stainless steel or glass scraper, this was done prior to color assessment. The assigned colors were then entered in the “remarks” field of the barrel sheet.

Automated measurements using the Minolta spectrophotometer provided quantitative color measurements (see “Physical Properties,” p. 16). Observations of the damp core surface were made as soon as possible after the core was split. Note that many surficial oxidation reactions are completed within seconds after splitting organic-rich cores of reduced sediment, and others proceed over the course of 1–2 hr. The surface colors documented here are not necessarily identical to those of the pristine, unoxidized sediment prior to the exposure to atmospheric oxygen, or to the stable “equilibrium” colors reached after complete surface oxidation.

Smear Slides

Smear slide samples were taken from the archive halves. For each sample, a small amount of sediment was removed with a wooden toothpick, dispersed evenly in deionized water on a 1-in × 3-in glass slide, and dried on a hot plate at a low setting. A drop of mounting medium and a 1-in × 1-in cover glass was added, and the slide was placed in an ultraviolet light box for ~30 min. Once fixed, each slide was scanned at 100×–200× with a transmitted light petrographic microscope using an eyepiece micrometer to assess grain-size distributions in clay (<4 μm), silt (4–63 μm), and sand (>63 μm) fractions. The eyepiece micrometer was calibrated once for each magnification and combination of ocular and objective, using an inscribed stage micrometer.

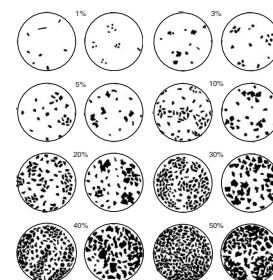
The volume percent technique (Fig. F7) was often employed as an intermediate step toward calculating relative proportions of each grain size and type. Note that smear slide analyses tend to underestimate the abundance of sand-sized and larger grains (e.g., foraminifers, radiolarians, and siliciclastic sand) because these are difficult to incorporate into smear. At the same time, clay-sized biosilica, being transparent and isotropic, are very difficult to quantify. Clay minerals, micrite, and nanofossils can also be difficult to distinguish at the very finest (<~4 μm) size range. After scanning for grain-size distribution, several fields were examined at 200×–500× for mineralogical and microfossil identification. Standard petrographic techniques were employed to identify the commonly occurring minerals and biogenic groups, as well as important accessory minerals and microfossils.

Smear slide analysis data tables are included in this volume. These tables include information about the sample location, whether the sample represents a dominant (D) or a minor (M) lithology in the core, and the estimated percentages of sand, silt, and clay, together with all identified components.

PHYSICAL PROPERTIES

Physical properties were measured on core material recovered during Leg 202 in order to (1) provide data for the correlation of cores among holes at any given site for the construction of complete stratigraphic sequences; (2) detect changes in sediment properties that could be related to lithologic changes, diagenetic features, or consolidation history; (3) provide the dry density records needed for computing mass accumulation rates; (4) identify natural and/or coring-induced discontinuities (e.g., gaps and hiatuses); and (5) provide data to aid interpretation of seismic reflection and downhole geophysical logs.

F7. Comparison chart for volume percentage estimation, p. 58.



Magnetic susceptibility (MS), GRA bulk density, compressional wave velocity (V_p), and NGR were measured on the whole-core MST. Thermal conductivity (TC) was also measured on whole-round cores. Split-core measurements on the working half of core included V_p with the ODP P -wave sensor number 3 (PWS3) and moisture and density (MAD). Color reflectance (CR), magnetic susceptibility point sensor (MSP) measurements, and digital imaging were performed on the archive-half cores.

Magnetic susceptibility was also measured with the OSUS Fast Track, installed during Leg 202 specifically for the fast logging of whole-round core sections immediately after recovery. These measurements aided real-time stratigraphic correlation without being limited by the time constraints of MST measurements.

The shipboard party decided to integrate sedimentological and physical properties observations into the “Lithostratigraphy” sections of the site chapters. This was compatible with and thought to promote the primary objective of the physical properties program, to aid lithologic characterization of sediment sections.

Oregon State University Magnetic Susceptibility Fast Track Sampling Strategy

Rapid stratigraphic correlation of cores from adjacent holes and real-time feedback to drillers for recovering complete stratigraphic sections at all sites (see “**Stratigraphic Correlation**,” p. 9, in “Operational Innovations” in the “Leg 202 Summary” chapter and “**Composite Section**,” p. 4) were major cruise objectives. The OSUS automated, dedicated track for rapid measurement of magnetic susceptibility was therefore installed during Leg 202 to provide a proxy of sediment variability to the stratigraphic correlators without delay. It uses a Bartington MS2 susceptibility meter (108-mm loop diameter) that was zeroed before a section scan, but no drift correction was applied. The usual sampling interval was 5 cm. Many sediment intervals recovered during Leg 202 had little terrigenous material, and the 1-s integration time setting (~15-min logging time per core) provided insufficient signal resolution. We therefore measured mostly with the 10-s integration time setting, which increased the logging time to ~40 min per core. However, this was still fast enough to keep up with core recovery under most circumstances and significantly faster than the MST logging time, which was set to gather the best possible data with the four sensors as described below.

Multisensor Track Sampling Strategy

Magnetic susceptibility and GRA bulk density were measured non-destructively on all whole-round core sections with the MST. NGR was measured on most core sections, but the sensor had to be turned off to save core logging time for some intervals. Compressional wave velocity was measured on most core sections, but the sensor was turned off when acoustic coupling proved insufficient (gassy sediment) or when core disturbance was too pervasive to give a reliable signal.

Sampling intervals and periods were the same for all sensors for any one core in order to optimize MST performance. At some sites, comparison with downhole Formation MicroScanner (FMS) data shows that bulk density variability in the sediment could potentially be resolved at subcentimeter resolution. However, the limits of instrument performance combined with the time constraints from coring operations did

not allow sampling at 1 cm or less. Sampling intervals were therefore set at 2.5 or 5 cm, depending on time availability, with most cores measured at 5-cm intervals. These particular intervals are common denominators of the distances between the instruments installed on the MST (30–50 cm) and allow truly simultaneous measurements and therefore optimal use of total measurement times.

Sampling periods varied from 3 to 5 s, depending on total time available, with most cores measured at 5 s per sample. Longer sampling times would have been desirable to improve the NGR and MS signal but were not possible given the rate of core recovery.

The total time availability for MST logging at a site was predicted based on operational time estimate for the site, subsequent transit time, and any other time available before core was on deck at the subsequent site. Sampling parameters were then optimized to use the total available time (e.g., 2.5 cm and 5 s [~ 2 hr/core]; 5 cm and 5 s [~ 1.2 hr/core]; 5 cm and 3 s [fast logging, ~ 0.9 hr/core]).

Archive Multisensor Track Sampling Strategy

Two instruments were mounted on the AMST: the Minolta photo-spectrometer measuring diffuse color reflectance and an MSP. CR was measured at 2.5 cm throughout Leg 202 cores. MSP measurements were taken only at the first two sites (1232 and 1233), when it became clear that the measurement was too slow to be accommodated in the time available. The present AMST configuration requires that CR and MSP runs must be taken one after the other. A measurement system that allows simultaneous measurement of CR and MSP would be needed to make MSP measurements feasible.

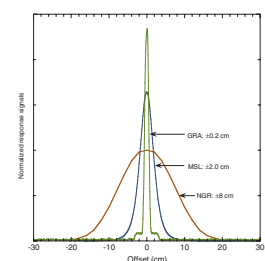
Magnetic Susceptibility

Magnetic susceptibility is the degree to which a material can be magnetized in an external magnetic field. It provides information on the magnetic composition of the sediments that often can be related to mineralogical composition (e.g., terrigenous vs. biogenic materials) and/or diagenetic overprinting (e.g., Thompson and Oldfield, 1986). Magnetite and a few other iron oxides with ferromagnetic characteristics have a specific MS several orders of magnitude higher than clay, which has paramagnetic properties. Carbonate, silica, water, and plastics (core liner) have small negative values of MS. Sediments rich in biogenic carbonate and opal therefore have generally low MS, even negative values, if practically no clay or magnetite is present. In such cases, measured values approach the detection limit of MS meters.

MS was measured with the Bartington Instruments MS2C system on both the MST and the OSUS track and with the MS2f on the AMST track in some intervals at Sites 1232 and 1233 (the MS2f is not discussed here). The Bartington system applies a low field (~ 50 mT) with an inducing field frequency of 0.565 kHz. It provides a low-sensitivity setting of 1.0 (instrument integration time of 1 s) and 0.1 (integration time of 10 s). The MST uses an 8-cm nominal diameter loop (88-mm coil), which yields a Gaussian response function with full width at half maximum (FWHM) value of ~ 8 cm (Fig. F8). The OSUS system featured a 10-cm nominal diameter loop (108 mm coil) with a FWHM of 9 cm.

The output of the MS meters can be set to centimeter-gram-second (cgs) units or International System (Système International [SI]) units, and the ODP standard is the SI setting. However, to actually obtain the

F8. FWHM of the GRA, MSL, and NGR, p. 59.



dimensionless SI volume-specific magnetic susceptibility values, the instrument units stored in the ODP database must be multiplied by a correction factor to compensate for instrument scaling and the geometric ratio between core and loop dimensions. For a standard APC core diameter of 66 mm and loop diameters of 88 mm (MST) and 108 mm (OSUS Fast Track), these correction factors are 1.46×10^{-6} and 0.79×10^{-6} , respectively, as read from a graph in the Bartington operation manual.

The ratio (~1.86) of these two Bartington compensation factors should represent the factor necessary to convert OSUS Fast Track values to MST values. To test this, we ran a small magnetically susceptible calibration ring through both tracks and calculated the integrals under the response curves (Table T3; Fig. F9). The ratio of the integrals was 1.685. We also compared the instrument values from many core measurements taken on both tracks during Leg 202. The ratios between measured values ranged from 0.5 to 2.0 and averaged ~1.5. The variability in the ratio is thought to be related to the different shapes of the response curves resulting from different loop diameters.

A common operational problem with the Bartington meter is that 1-s measurements are rapid but not precise enough for biogenic-rich sediments, and the 10-s measurements are much more precise but take a prohibitively long time to measure at the desired sampling interval of 2.5 to 5 cm. The MST program was therefore equipped with the option to average any number of 1-s measurements, and we usually averaged five measurements. The OSUS track did not have this option and was mostly run with 10-s integration time.

Gamma Ray Attenuation Bulk Density

Bulk density reflects the combined effect of variations in porosity, grain density (dominant mineralogy), and coring disturbance. Porosity is mainly controlled by lithology and texture (e.g., clay, biogenic silica, and carbonate content, and grain size and sorting) and compaction and cementation. In homogeneous pelagic and hemipelagic sediments drilled during Leg 202, bulk density was often a function of the relative amount of calcareous nannofossils and diatoms, which resulted in significant fabric and thus porosity variations as well as grain density variations.

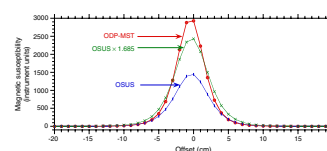
The GRA densitometer consists of a 10-mCi ^{137}Cs capsule as the gamma ray source, with the principal energy peak at 0.662 MeV, and a scintillation detector. The narrow collimated peak is attenuated as it passes through the center of the core. Incident photons are scattered by the electrons of the sediment material by Compton scattering. The attenuation of the incident intensity (I_0) is directly related to the electron density in the sediment core of diameter (D), which can be related to bulk density given the average attenuation coefficient (in micrometers) of the sediment (Evans, 1965; Harms and Choquette, 1965). Since the attenuation coefficient is similar for most common minerals and aluminum for practical purposes, bulk density is obtained through direct calibration using aluminum rods of different diameters mounted in a core liner that is filled with distilled water. The GRA densitometer has a spatial resolution of <1 cm (Fig. F8).

P-Wave Velocity

P-wave velocity in marine sediments varies with the lithology, porosity or bulk density, state of stress such as lithostatic pressure, fabric or

T3. Magnetic susceptibility signal response, p. 67.

F9. Response curves for two magnetic susceptibility sensor loops, p. 60.



degree of fracturing, degree of consolidation and lithification, occurrence and abundance of free gas and gas hydrate, and other properties. *P*-wave velocity was measured with two systems during Leg 202, with the MST-mounted *P*-wave logger (PWL) on whole-round cores (Schultheiss and McPhail, 1989) and with the PWS3 on split cores. The *P*-wave sensors number 1 and 2 (PWS1 and PWS2), transducer pairs built into pairs of knifelike probes that are inserted into soft sediment, were not used during Leg 202. All ODP *P*-wave piezoelectric transducers transmit a 500-kHz compressional wave pulse through the core at a repetition rate of 1 kHz.

Traveltime is determined by the software, which automatically picks the arrival of the first wavelet to a precision of 50 ns. It is difficult for an automated routine to pick the first arrival of a potentially weak signal with significant background noise. The search method applied skips the first positive amplitude and finds the second positive amplitude using a detection threshold limit (DTL), typically set to 30% of the maximum amplitude of the signal. Then it finds the preceding zero crossing and subtracts one period to determine the first arrival. To avoid extremely weak signals, minimum signal strength (MSS) can be set (typically to 0.02 V) and weaker signals are ignored. To avoid cross-talk signals at the beginning of the record from the receiver, a delay (typically set to 0.01 ms) can be set to force the amplitude search to begin in the quiet interval preceding the first arrival. In addition, a trigger (typically 4 V) is selected to initiate the arrival search process, and the number of waveforms to be stacked (typically 5) can also be set. Length of the travel path is determined by linear voltage differential transducers.

The *P*-wave velocity systems require two types of calibration, one for the displacement of the transducers and one for the time offset. For the displacement calibration, five acrylic standards of different thickness are measured and the linear voltage-distance relationship determined using least-squares analyses. For the time offset calibration, room-temperature water in a plastic bag is measured multiple times with different transducer displacements. The inverse of the regression slope is equal to the velocity of sound in water, and the intercept represents the delay in the transducers.

In cases of bad acoustic coupling between the sediment and the liner, the PWL generally does not provide accurate velocity values. The system is, therefore, most useful in undisturbed APC cores, and values become highly questionable when gas is present in the sediment. A correction for the core liner, which is made of Tenite with a sonic velocity of 1987 m/s, is applied routinely. This is accomplished by subtracting the total liner thickness (2.54 mm for split cores and 5.12 mm for whole cores) from the transducer displacement measurement and subtracting the calculated transit time based on the sonic velocity in Tenite from the measured transit time.

Natural Gamma Radiation

Terrigenous sediment is often characterized by NGR from K and Th, which are present mostly in clays but can also originate from heavy minerals or lithic grains. Uranium often dominates the NGR in carbonate-rich sediments with little terrigenous input. Uranium concentration is largely controlled by organic matter flux to the seafloor and the existing redox conditions there. It is also mobile and can migrate to certain layers and diagenetic horizons. In biogenic oozes, such as those drilled

during Leg 202, U records may be used as indicators of production and/or preservation of organic matter.

The natural gamma ray system consists of four shielded scintillation counters with 3 in × 3 in doped sodium iodide crystals, arranged at 90° from each other in a plane orthogonal to the core track. The FWHM of the NGR response curve is ~17 cm (Fig. F8), an interval that could be considered a reasonable sampling interval. Measurement precision is a direct function (inverse of square root) of the total counts (N), accumulated for one measurement, according to Poisson's Law of random counting error. N is the product of the intrinsic activity of the material measured and the total measurement time. Therefore, one would always want to maximize the measurement time to improve data quality. Unfortunately, time constraints on core logging during the cruise do not permit long counting times. Furthermore, NGR is measured every 5 cm (same sampling interval as other MST measurements for optimal MST efficiency) and, therefore, only for a short time (typically 5 s). It may be necessary, particularly in low-activity material, to integrate (or smooth) several adjacent measurements to reduce the counting error to an acceptable level. Five-point smoothing is a reasonable data reduction in view of the relatively wide response curve of the sensors. (See Blum, 1997, for more detailed discussions).

Thermal Conductivity

TC estimates were needed to calculate downhole temperature from measurements taken with the APC temperature (APCT) tool and will be required for the estimation of heat flow. TC was therefore mainly measured in intervals where downhole temperature measurements were taken, using whole-round cores and the needle probe method in full-space configuration.

We used the Teka TK04 measurement system, which employs the transient linear heat source method with a needle probe that is inserted into the soft sediment (ASTM, 1993; Blackwell, 1954; DeVries and Peck, 1958; Von Herzen and Maxwell, 1959; Vacquier, 1985). The TK04 uses an automated routine to find the conductivity by least-squares fitting to the measured temperature time series. The probes were calibrated with a Macor ceramic standard with a value of 1.61 W/(m·K). Measured values were low in the high-porosity sediments recovered during Leg 202, ranging between 0.8 and 1.2 W/(m·K).

Moisture and Density

Water (moisture) content, bulk density, grain density, dry density, porosity, and void ratio are solid to interstitial water phase relationships in sediments calculated routinely in the ODP Janus database from the measurement of wet and/or dry mass and wet and/or dry volume (ASTM, 1990), according to equations given in Blum (1997). These phase relationships are useful for general lithologic characterization, calculation of mass accumulation rates, and calibration of GRA bulk density records measured at much higher depth resolution.

Samples of ~10 cm³ were taken from the working-half sections with a piston minicorer and transferred into 10-mL glass vials. Usually, one sample per section was taken at a fixed location (75 cm) in each section coincident with the location of the PWS3 sonic velocity measurements, carbonate and total organic content samples, and smear slide samples. The sampling program was usually completed in the most complete

hole at a site, and gaps were filled with measurements from other holes from that site if warranted. Wet and dry masses were determined with twin balances that allow for compensation of the ship's heave gravitational effect on the balance and give a precision better than 1%. The samples were dried in a convection oven at a temperature of 105°–110°C for a period of 24 hr. Dry volume was measured with a helium-displacement Quantachrome Penta-Pycnometer with an uncertainty of <0.02 cm³. Five measurements were averaged for each sample.

Color Reflectance Spectrophotometry

Sediment color primarily reflects the composition of the sediment and is affected by some other properties such as moisture, sediment grain size, and split-core surface texture (Balsam et al., 1997). The plastic film put over the sediment to protect the instrument also affects the reflectance spectra collected (Balsam et al., 1997). Quantitative, high-resolution measurement of color has the advantage over visual color description of providing measurements compatible with other physical properties measurements and allowing rigorous data analyses and sediment classification based on color. Some sediment components significantly influence sediment color, such as calcium carbonate representing the relative amount of major biogenic components, iron oxides that may indicate eolian origin, organic matter that may be used as a proxy for paleocean productivity, or chlorite as an indicator of diagenetic alteration. Such components can be (semi)quantitatively recognized in the color spectrum in its derivative values (Deaton and Balsam, 1991; Balsam et al., 1995, 1997, 1998; Balsam and Deaton, 1996; Balsam and Wolhart, 1993; Balsam and Damuth, 2000; Giosan, 2001) or in color parameters calculated from the spectrum, such as L*a*b*, which define a lightness-chroma color space.

During Leg 202, raw reflectance spectra were used to identify absorption features typical for organic pigments and first derivatives of the spectra were used to detect goethite and hematite. Semiquantitative estimates of chlorins and hematite contents were obtained from their characteristic features expressed in the raw spectra and their first derivative, respectively. Both spectra and derivatives were employed in a multiple regression between direct geochemical measurements and reflectance spectroscopy data for estimating carbonate and total organic carbon (TOC) contents. Reflectance input data included 31 raw reflectance values over the visual spectrum (400–700 nm) at a 10-nm interval and their first derivatives with respect to wavelength. Regression equation terms were selected with a stepwise procedure, and they were retained in the equations only if significant above a 95% level. Using this technique in real time during the cruise promotes understanding of the relationship between sediment composition and physical properties and allows detection of variability in carbonate and TOC that cannot be measured rapidly at high resolution.

Diffuse reflectance of visible light was routinely measured using the Minolta CM-2000 spectrophotometer mounted on the AMST. This instrument measures light at visible wavelengths (400–700 nm) in 31 intervals of 10 nm (ASTM, 1985). A black-and-white calibration was performed every day.

Split cores were covered with clear plastic wrap and placed on the AMST. A laser detector mounted on the AMST creates a log of the split-core surface height and ensures gentle and complete contact of the integration sphere with the sediment surface and skipping of empty inter-

vals. Small cracks and surface irregularities may go undetected, however, and the data may contain spurious measurements that should be eliminated from the data set before use.

DIGITAL IMAGING SYSTEM

A new ODP DIS, which was custom-fabricated by Geotek Ltd., was installed in November 2001, prior to Leg 199. Following tests on Legs 199–201, the system was upgraded with new software in March 2002 during the port call in Valparaiso, Chile. Leg 202 was the first cruise to use the DIS routinely, and ~7 km of core was analyzed, creating ~15 GB of image data. Procedures for the reduction and use of image data were adopted and developed based on these upgrades and as needed based on a variety of tests made during Leg 202. Some problems were discovered as a result of these activities, yielding some recommendations to aid in planning and implementation of future upgrades to the DIS.

System Description

In the ODP DIS system, as many as four core sections are loaded onto stationary rails, and the camera system moves along each section in an automated sequence. The ODP DIS uses a proprietary Geoscan line-scan camera assembled by Geotek. The camera includes three 1024-pixel charge coupled device (CCD) arrays, one for each color, red, green, and blue (RGB). The camera is located above the light source and views the core through a slot in the top of the light housing. Light reflected from a core surface passes through a standard Pentax lens, and is split into three paths by a beam splitter. The three beams then pass through dichroic interference filters designed to pass blue (<515 nm), green (515–585 nm), and red (>585 nm), respectively, before falling on the CCD detectors located at the focal plane of the lens. The blue channel receives 50% of the total light collected (because the CCD detector is less efficient at short wavelengths), whereas the green and red channels each receive 25% of the light collected. Each CCD array has 8-bit precision (i.e., values from 1 to 256), so when the three color channels are combined the total color precision is 24-bit.

Two high-frequency fluorescent tubes oriented across the cores on either side of the image line illuminate the sediment cores. This lighting system is intended to flood the core with uniform light and to minimize shadows caused by microtopography on the core surface. The bright light source was generally assumed to overpower any ambient laboratory light. However, preliminary evidence during Leg 202 indicated that ambient laboratory light, which varies with position in the DIS, contaminated some images. The shipboard party therefore covered the porthole in the sediment laboratory and constructed a temporary cardboard cover for the DIS to shade the instrument from ambient light. Water on the surface of the split cores can cause specular reflections, which degrade the image by reflecting either ambient light or light from the fluorescent tubes directly to the camera.

The spectral response of the system is a function of the spectrum of the light source, which can evolve through time, the efficiency of the CCD arrays at different wavelengths, and the various optical components. Under typical conditions, the greatest efficiency of response for the Geotek system (i.e., field of >50% of peak efficiency) is ~450–505 nm for the blue channel, ~530–555 nm for the green channel, and

~605–630 nm for the red channel (Fig. F10). Spectral biases between the RGB bands are calibrated using external standards for dark current and white balance.

The housing for the light source is adjusted vertically to be as close as possible to the core surface (nominally 1 cm) so that the lighting will be as uniform and as bright as possible on the sediment surface, overpowering any ambient room light that varies depending on location in the system (e.g., from the top to the bottom of core sections) or through time (e.g., if a person walking by inadvertently shades the system from ambient light). The height of the camera assembly can be adjusted above the light housing so that the CCD array scans a width of ~9 cm and a split core section approximately fills the CCD array. The CCD array includes three reference pixels on the left side of each core section that are coated in an opaque (black) substance. These pixels are used for software adjustment of the time-variable zero value on all pixels (known as the dark current) due to thermal or electronic drift. Ideally, these calibration pixels are not affected by current in adjacent pixels, however, CCD arrays can be sensitive to pixel “bleed” effects if nearby pixels exceed saturation.

The spatial resolution of the DIS system depends on the height of the camera above the sediment, but it is nominally 100 pixels per centimeter in both the downcore and cross-core directions. Rulers are placed along the sediment cores and imaged to confirm depth calibrations.

Calibration Procedures

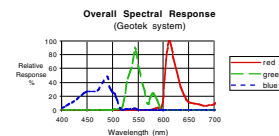
Focus and Aperture

After the geometry of the camera-core system was set, the camera was manually focused by ODP personnel (typically once per day) to maximize contrast on a sharp transition (black lines on color calibration card or sharp edge of the core liner). Given adequate depth of field (depending on aperture) the focus does not need to be reset for minor variations in the core surface. Aperture is set to maximize the dynamic range of the system for normal color variability in the cores to be measured, within the limits of needing reasonable depth of field to stay in focus. To set aperture, an RGB “scope” is used to display all 1024 pixel intensities over a relatively bright interval of core, and aperture is adjusted until one or more colors approaches but does not exceed color saturation (limited by 8-bit precision to values of 256 in each CCD). The aperture setting was entered manually into the program to allow for intensity normalization (see below). For each core section batch run, the operator monitored the intensities; if they decreased, the aperture was manually increased, and vice versa, and the new aperture setting was entered accordingly.

Black-and-White Calibration

Color calibration of each pixel occurs at the black (dark current) level by collecting data with the lens cap on and at the white (nominally 100% reflectance) level using a white ceramic tile. The camera travels a short distance across the tile to remove the effects of any dust, which could affect individual pixels. White calibration is a function of both aperture and integration time. Calibration need not be done at the same aperture setting as data collection as long as the aperture settings are entered accurately in the software. These settings are used to adjust

F10. Spectral response of the DIS system, p. 61.



pixel intensities based on the theoretical relation $I = 1/f^2$, and as a result, raw pixel intensity values can exceed the number 256. These aperture calibrations could be adjusted based on empirical analysis of gray-scale standards at different aperture settings, but such features were not implemented during Leg 202. Black-and-white calibration should be done as often as possible; ideally, between each group of core sections. In practice, manual calibrations were done roughly every 12 to 24 hr, usually associated with shift changes.

The constraints of 8-bit color resolution and the typical range of sediment color variations require frequent aperture adjustments. CCD saturation levels have to be monitored constantly by the operator, aperture adjustments have to be done manually, and the new setting has to be entered manually as well. Repeat scans were often necessary to obtain images with the appropriate aperture setting after inadequate images were discovered. More automation, such as automated aperture or exposure time adjustments (based on quick lightness scans over the cores) and/or oversaturation and low-intensity alerts, would enhance the operational efficiency of the system.

Measurement Procedures

Four sections at a time were placed in the DIS with the tops of sections against a rigid stop defined as zero depth in section, and a barcode label was scanned for entry of core identification information. All four sections were then scanned automatically by the system in ~20 min. Scanning generally occurred in parallel with description of other sections of the same core, and the digital images were therefore generated immediately before or after visual description and prior to analysis of full-color reflectance spectra on the AMST and intensity and direction of magnetic remanence with the cryogenic magnetometer.

Data Processing

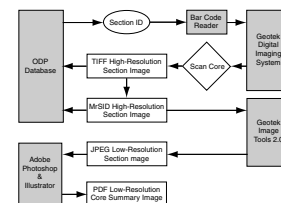
Curated Section Length

When a core is cut into sections on the catwalk, ODP personnel enters the “liner length” (usually 150 cm, except for the last section, which is typically shorter) for each section into the database. Unfortunately, data processing is sometimes complicated by the fact that a core section length does not stay the same: cores keep expanding during the core analysis process as a result of continuing gas escape, clay swelling, and/or elastic rebound, depending on lithology, hydrocarbon content, and drilling depth. The expanding core pushes the liner end caps out in a bulge, breaks the end cap’s acetone bond, or even extrudes above and beyond the end cap. By the time the Leg 202 cores were scanned, sections were typically 1–3 cm longer than the liner length. Since the objective was to scan the entire core, the DIS operator had to measure the “curated length” (at the time of scanning) and enter it as a measurement parameter into the instrument’s program. ODP personnel subsequently entered the curated section lengths into the database.

Data Products

Figure F11 illustrates the DIS image products that were created during Leg 202. The DIS saves image data in TIFF formats on a local computer. During acquisition, red, green, and blue pixel intensities can be

F11. Data products produced from the Geotek DIS system during Leg 202, p. 62.



averaged across user-defined intervals and saved as ASCII text RGB files. Because average values are saved as integers, some precision is lost in this operation. After some experimentation during Leg 202, we saved RGB summary data averaged over 0.1-mm depth increments, using 400 pixels in a stripe across the center of each core section, and then averaged these separately (using software written at sea) to intervals of 1 or 2 cm without truncating the resulting averages to integer values. Original TIFF and RGB files were archived at ODP.

The original TIFF images were compressed without loss of information using MrSID software, and these images were archived and were available online. From the MrSID files, the yeoperson created composite JPEG images of each core, which were saved as PDF images and distributed to the scientific party. These images substantially reduced the spatial resolution relative to the original TIFF images and were of an easily manageable size that proved to be very useful at sea for informal “second look” analysis and confirmation of core descriptions. Following Leg 202, the production of such “low-resolution” core summary images became an integral and direct output of the DIS system.

Image Artifacts

The first sets of Leg 202 digital core images revealed light-colored stripes across the image (3 pixels downcore) spaced very regularly at 5 mm or, in some cases, at 1 mm. The lines appeared to be an “overexposure” related to some kind of energy flux across the CCD array. These artifacts were caused by high contrast in the millimeter markings on the rulers placed along the edge of the cores. Oversaturation of image pixels adjacent to the opaque calibration pixels in the CCD array resulted in pixel “bleed” effects into the calibration pixels. The DIS interpreted this pixel bleed as thermal drift, and adjusted the image calibration accordingly, resulting in apparent overexposure. This problem was apparent when relatively low (open) aperture settings were used to image dark sediments.

Additional bright lines occurred in many images at 30-cm intervals. This artifact appears related to small variations in image integration time, as the DIS software transfers data from the camera to the computer every 30 cm and appears to stop the motor for a split second during the process. This software bug must be corrected by the manufacturer.

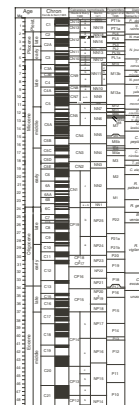
BIOSTRATIGRAPHY

We used the timescale of Berggren et al. (1995b) during Leg 202. The biostratigraphic zones/subzones of calcareous nannofossils, planktonic foraminifers, and diatoms are summarized in Figure F12. Detailed descriptions of the shipboard methods used for different groups of microfossils follow.

Calcareous Nannofossils

During Leg 202, we referred to the zonal schemes of Martini (1971) and Bukry (1973, 1975), code numbered by Okada and Bukry (1980). These zonations are regarded as a standard framework for the biostratigraphic subdivision of low-latitude Cenozoic marine sediments based on calcareous nannofossils, and some of these events are also identifi-

F12. Correlation of geomagnetic polarity timescale and biostratigraphic zonations, p. 63.



able in middle to high latitudes. In addition to the classical concept of first occurrences (FOs) and last occurrences (LOs) of index species, we used abundance variations of some taxa to improve the stratigraphic resolution of the Pleistocene interval. The top of the *Gephyrocapsa caribbeanica* acme zone, dated at 260 ka, is synchronous with the FO of *Emiliana huxleyi* (Pujos, 1988) and, thus, provides a useful alternative to identify the base of Martini's NN21 Zone. The ages of most calcareous nannofossil data employed to construct the Leg 202 age model for the Pliocene–Pleistocene interval come from the work of Raffi et al. (1993), Wei (1993), and Raffi and Flores (1995). For the Miocene, we followed the biochronology proposed by Raffi and Flores (1995) and made comparisons with the proposals of Backman and Raffi (1997) and Young (1998) (Table T4).

Methods

Standard smear slides were made for all samples using Norland optical adhesive as a mounting medium. Calcareous nannofossils were examined by means of a light-polarized microscope, at 1000× magnification. Unless otherwise noted, we followed taxonomic concepts summarized in Perch-Nielsen (1985). For morphometric concepts concerning the *Gephyrocapsa* group, we mainly followed Raffi et al. (1993). We also considered (1) *G. caribbeanica* (3–4 μm), whose acme is coincident with the FO of *E. huxleyi*, and (2) *Gephyrocapsa* sp. 3, whose FO is coincident with the reentrance of *Gephyrocapsa* medium (4–5.5 μm) in low-latitude regions (Raffi et al., 1993).

To assess nannofossil preservation, etching and overgrowth are the most important features. We ranked preservation with the following code system:

- G = good (little or no evidence of dissolution and/or secondary overgrowth of calcite; diagnostic characters fully preserved).
- M = moderate (dissolution and/or secondary overgrowth; partially altered primary morphological characteristics; however, nearly all specimens can be identified at the species level).
- P = poor (severe dissolution, fragmentation, and/or secondary overgrowth with primary features largely destroyed; many specimens cannot be identified at the species level and/or generic level).

Regarding relative abundance of individual species or morphotypes, five levels were considered:

- D = dominant (>10 nannoliths per field of view).
- A = abundant (1–10 nannoliths per field of view).
- C = common (1 nannolith per 2–10 fields of view).
- F = few (1 nannolith per 11–50 fields of view).
- R = rare (1 nannolith in >50 fields of view).

Total abundance of calcareous nannofossils for each sample was estimated as follows:

- VA = very abundant (>100 nannoliths per field of view).
- A = abundant (10–100 nannoliths per field of view).
- C = common (1–9 nannoliths per field of view).
- F = few (1 nannolith per 2–10 fields of view).

T4. Ages of calcareous nannofossil datum levels, p. 68.

- R = rare (1 nannolith in >10 fields of view).
B = barren.

Planktonic Foraminifers

Preliminary ages were assigned to core catcher samples. The zonal schemes of Berggren et al. (1995a, 1995b) were applied for the Cenozoic. The astrochronologically tuned planktonic foraminiferal ages of Berggren et al. (1995a, 1995b) were used from the Holocene to 4.70 Ma. The tuned ages of Chaisson and Pearson (1997), Pearson and Chaisson (1997), and Curry, Shackleton, Richter, et al. (1995) were used for 4.7–13.42 Ma. Ages older than 13.42 Ma were untuned and taken from Berggren et al. (1995b) and Berggren et al. (1995a) (Table T5). In addition to the above ages, we also used the LO (0.12 Ma) (Thompson et al., 1979) and FO (0.40 Ma) (Li, 1997) of pink *Globigerinoides ruber* as biostratigraphic references. Taxonomic concepts for Neogene and Paleogene taxa are illustrated in Kennett and Srinivasan (1983), Bolli and Saunders (1985), and Toumarkine and Luterbacher (1985).

T5. Ages of planktonic foraminifer datum levels, p. 69.

Methods

Unlithified to semilithified core sediment samples were soaked in tap water and then washed over a 63- μ m sieve. Lithified material was crushed to pea size, boiled in a solution of Calgon diluted to 1% by weight, then sieved and dried as before. Cleaned sieves were put into a sonicator for several minutes to avoid contamination between successive samples. Washed samples were examined under a binocular microscope.

Planktonic foraminiferal abundance in relation to total residue was categorized as follows:

- A = abundant (>30%).
C = common (10%–30%).
F = few (5%–10%).
R = rare (<5%).
P = only a few broken tests recorded in a sample.
B = barren.

Preservation was categorized as follows:

- VG = very good (no evidence of breakage or dissolution).
G = good (dissolution effects are rare; >90% of specimens unbroken).
M = moderate (dissolution damages, such as etched and partially broken tests, occur frequently; 30%–90% of specimens unbroken).
P = poor (strongly recrystallized or dominated by fragments or corroded specimens).

Planktonic foraminiferal species abundance in a random sample of 200–400 specimens from the >150- μ m size fraction was defined as follows:

- D = dominant (>30%).
A = abundant (10%–30%).
F = few (5%–30%).

- R = rare (1%–5%).
P = present (<1%).
B = barren.

Benthic Foraminifers

Benthic foraminifers provide limited biostratigraphic age control as currently applied to Leg 202 samples. Whenever possible, the LO of the benthic foraminifer *Stilostomella* was noted. Most species of this genus disappeared from the global ocean at different latitudes during the interval of 1.0–0.6 Ma (Hayward, 2001). For the Leg 202 sites, we used 0.65 Ma as the LO of *Stilostomella* (Hayward, 2001).

Benthic foraminifers were identified mainly to determine past changes in oxygenation and carbon flux, as these are main factors controlling abundance and species composition in deep-sea assemblages (Jorissen and Rohling, 2000). The generic classification of Loeblich and Tappan (1988) was used and updated in some instances. Taxonomic assignments follow Tjalsma and Lohmann (1983), van Morkhoven et al. (1986), Miller and Katz (1987), Thomas (1990), Katz and Miller (1991), Holbourn and Henderson (2002), and Kuhnt et al. (2002).

Methods

Benthic foraminifers were examined from core catcher samples used for planktonic foraminiferal studies. Relative percentages of benthic to planktonic tests were determined by counting specimens in four adjacent quadrants in three different locations on the tray. To assess assemblage composition and variability downhole, ~200 specimens from the >150- μ m fraction were picked from each core catcher sample and mounted onto slides prior to identification and counting, whenever time allowed. The fine fraction was cursorily checked for small taxa.

Preservation was categorized as follows:

- VG = very good (no evidence of breakage or dissolution).
G = good (>90% of specimens unbroken).
M = moderate (30%–90% of specimens unbroken).
P = poor (strongly recrystallized or dominated by fragments or corroded specimens).

Diatoms

Diatoms characterize fertile surface waters and are abundant and diverse both within 5° of the equator and along the western margin of South and Central America. Numerous diatom biostratigraphic studies have been completed for the equatorial Pacific (Kanaya, 1971; Muchina, 1971; Burckle, 1972, 1977a, 1977b, 1978; Bukry and Foster, 1973; Jousé, 1973; Burckle and Trainer, 1979; Barron, 1980, 1981, 1983, 1985a, 1985b, 1992; Sancetta, 1983; Baldauf, 1985; Baldauf and Iwai, 1995). The Neogene and Quaternary diatom zonation used for the low-latitude sites of Leg 202 was that proposed by Barron (1985a, 1985b) and modified by Baldauf and Iwai (1995). Table T6 lists diatom biostratigraphic events, paleomagnetic calibration, and age estimates based on Barron (1985a, 1992) and Shackleton et al. (1995) and used during this leg.

In the marginal upwelling regions, the input of new nutrients (Dugdale and Goering, 1967) generates extensive diatom blooms (Margalef,

T6. Ages of diatom datum levels,
p. 72.

1978) and an uncoupling between the primary and secondary producers (Hutchings et al., 1995) that results in significant export flux to the sediments (Berelson et al., 1987). As such, the diatom record should preserve a great deal of information related to past productivity conditions (Schrader and Sorknes, 1990; Abrantes, 2000). Besides the works of Schuette (1980) and Abrantes (1988), Abrantes and Moita (1999) have shown that upwelling assemblages are marked by the dominance of the genus *Chaetoceros*, which spores are generally well preserved in the sediments. Variations in diatom abundance, and in particular of the genus *Chaetoceros*, may be used to trace upwelling variability along the most marginal sites. Indications of cold- and warm-water masses are based on the presence of oceanic/pelagic species with specific temperature distribution. The presence of benthic diatoms will be noted in order to assess the amount of displacement of shallow (<100 m water depth) material.

Methods

Smear slides were examined on a routine basis for stratigraphic markers. When required (because of low concentration of specimens), samples were processed by boiling them in hydrogen peroxide and hydrochloric acid, then cleansing them of acid by centrifuging (at 1200 rpm for 2–4 min), decanting off the liquid, washing in distilled water, and repeating that cycle four or more times, following the procedures of Baldauf (1984).

To remove the clay-sized particles, the residue was carefully shaken in a mixture of 0.5% sodium pyrophosphate and the procedure of centrifuging and decanting was repeated three times. Strawn slides of the clean material were prepared using Norland optical adhesive and cured in ultraviolet light for 3 min.

The entire microscope slide was routinely examined on a Zeiss Axio-plan microscope equipped with differential interference contrast (DIC) at 630× magnification to check for the presence of biostratigraphic marker species. Taxonomic identifications were routinely checked at 1000× magnification.

Abundance of diatoms was based on the number of specimens observed per field of view at 630× and noted as follows:

- A = abundant (10 or more valves per field of view).
- C = common (1–9 valves per field of view).
- F = few (>1 valve per each vertical traverse but <1 specimen per field of view).
- R = rare (>3 valves on slide but <1 specimen per each vertical traverse).
- T = trace (<3 valves observed on slide and/or appearance of fragments).
- B = barren (no valves observed on slide).

Preservation of diatoms was determined qualitatively and recorded as follows:

- G = good (both thinly and heavily silicified forms; robust forms are present and no alteration of the frustules was observed).
- M = moderate (thinly silicified forms are present but exhibit some alteration).

P = poor (thinly silicified forms are rare or absent; robust forms dominate the assemblage).

PALEOMAGNETISM

Paleomagnetic studies aboard the *JOIDES Resolution* during Leg 202 comprised routine measurements of the natural remanent magnetization (NRM) of archive-half sections before and after alternating-field (AF) demagnetization and low-field magnetic susceptibility (k) measurements.

The remanent magnetization of the archive halves of all core sections was measured, unless precluded by drilling-related deformation. The number of demagnetization steps applied to each core section was controlled by time constraints and core flow through the laboratory with a two- or three-step demagnetization scheme (taking ~9–14 min) applied to most 1.5-m-long core sections. The standard three-step measurement scheme involved the measurement and stepwise demagnetization of the NRM and AF demagnetization at peak fields of 10- or 20-mT and 20- or 25-mT steps. The low maximum peak demagnetization fields ensure that the archive halves remain useful for shore-based high-resolution (U-channel) studies of magnetic remanence. The large leader and trailer distance (20 cm) was used to allow future deconvolution of the long-core data. For shipboard analysis, we masked measurements within 10 cm from the ends of each section.

Long-core remanence measurements and AF demagnetizations were performed using a long-core cryogenic magnetometer (2-G Enterprises model 760-R). This instrument is equipped with a direct-current superconducting quantum interference device (DC-SQUID) and has an in-line AF demagnetizer capable of reaching peak fields of 80 mT. The pickup coils of the cryogenic magnetometer have a width at half-height of <10 cm for all three axes, though they may sense a magnetization over an interval of 30 cm. Measurements were made at 5-cm sample intervals starting 20 cm above the core section top and ending 20 cm below the base. Background resolution is affected by the magnetization of the core liner of $\sim 8 \times 10^{-6}$ A/m. The standard ODP magnetic coordinate system was used (+x = vertical upward from the split surface of archive halves, +y = left hand split surface when looking upcore, and +z = downcore).

During APC coring, full orientation was attempted using the tensor orientation tool, which is rigidly mounted onto a nonmagnetic sinker bar attached to the top of the core barrel assembly. The tensor tool consists of three mutually perpendicular magnetic field sensors and two perpendicular gravity sensors. The information from both sets of sensors allows the azimuth and dip of the hole to be measured as well as azimuth of the APC core (the azimuthal reference line is the double orientation line on the core liner).

Where magnetic cleaning appears from shipboard data to have isolated the characteristic remanent magnetization (ChRM), paleomagnetic inclinations and/or declinations (depending on site latitude) were used to make an initial designation of magnetic polarity zones. The revised timescale of Cande and Kent (1995) was used as a reference for the ages of Cenozoic polarity chrons.

The magnetic susceptibility was measured for each whole-core section as part of the MST analyses. The MST susceptibility meter (a Bartington MS2C meter with an 88-mm coil diameter and a 0.565-kHz fre-

quency) was set on SI units, and the output values were stored in the Janus database. The width at half-height of the response function of the susceptibility coil is ~4 cm (Blum, 1997), although the sensing region corresponds to a volume of 166 g/cm³ of cored material. To convert the stored values to SI units of volume susceptibility, they should be multiplied by 10⁻⁵ and by a correction factor to take into account the volume of material that passed through the susceptibility coils. This factor for a standard ODP core is ~0.66, based on laboratory/ship comparisons.

When time allowed, the partially demagnetized NRM intensity of selected core intervals were normalized by whole-core magnetic susceptibility measured on the MST to assess the potential for deriving estimates of relative geomagnetic field paleointensity. Though far from an ideal method, shipboard normalization provides a quick test of a sediment's potential for shore-based paleointensity studies.

GEOCHEMISTRY

The geochemistry program included characterization of volatile gases, interstitial water, sedimentary inorganic carbon, organic carbon, nitrogen, and sulfur, and organic matter type and maturity. These analyses were carried out as part of the routine shipboard safety and pollution prevention requirements and to provide preliminary information for shore-based research.

Sediment Gases Sampling and Analysis

During Leg 202, the compositions and concentrations of volatile hydrocarbons and other gases in the sediments were monitored at typical intervals of one per core. Samples were obtained by two different methods. The routine headspace procedure (Pimmel and Claypool, 2001) involved placing approximately 5 cm³ of sediment sample in a 21.5-cm³ glass serum vial that was sealed with a septum and metal crimp cap and heated at 60°C for 30 min. A 5-cm³ volume of gas from the headspace in the vial was removed with a glass syringe for analysis by gas chromatography.

A second gas sampling procedure, the vacutainer method, was used for gas pockets or expansion voids that appeared in the core while it was still in the core liner. A device with a heavy-duty needle was used to penetrate the core liner, and an attached syringe was employed to collect the gas.

Headspace and vacutainer gas samples were both analyzed using a Hewlett-Packard 5890 II Plus gas chromatograph (GC) equipped with a 2.4 m × 3.2 mm stainless steel column packed with 80/100 mesh HayeSep S and a flame ionization detector (FID). This instrument quickly measures the concentrations of methane (C₁), ethane (C₂), ethene (C₂=), propane (C₃), and propene (C₃=). The gas syringe was directly connected to the GC via a 1-cm³ sample loop. Helium was used as the carrier gas, and the GC oven temperature was held at 90°C. Data were collected and evaluated with a Hewlett-Packard 3365 Chemstation data-handling program. Calibrations were done using Scotty IV analyzed gases, and gas concentrations were measured in parts per million by volume.

When high concentrations of C₂₊ hydrocarbons or of nonhydrocarbon gases such as H₂S or CO₂ were suspected, gas samples were analyzed

with the Natural Gas Analyzer (NGA), which routinely measures hydrocarbons through C_6 . The NGA system consists of a Hewlett-Packard 5890 II Plus GC equipped with multiport valves that access two different column and detector combinations. Hydrocarbons from methane to hexane were measured with a 60 m \times 0.32 mm DB-1 capillary column and an FID. The GC oven holding this column was heated from 80° to 100°C at 8°C/min and then to 200°C at 30°C/min. Nonhydrocarbon gases were isothermally analyzed at the same time using a sequence of packed columns (15-cm HayeSep R column connected to a 1-m molecular sieve column and a 2-m Poropak T column) and thermal conductivity detectors (TCDs). Helium was the carrier gas in both systems, and a Hewlett-Packard Chemstation was used for data acquisition and processing. Chromatographic response was calibrated against pre-analyzed standards. Gas contents are reported in parts per million by volume.

Interstitial Water Sampling and Chemistry

Interstitial waters were extracted from 5- to 10-cm-long whole-round sections that were cut and capped immediately after core retrieval on deck. In one hole at each site, samples were taken from each core for the upper 100 mbsf and, depending on the site and depth range, at intervals from every core to every second to third core thereafter to total depth. Occasionally, samples from more than one hole were treated as constituting a single depth profile using mcd as the depth reference. At Sites 1239 and 1240, interstitial water samples were taken more frequently (one per section for the upper 60 mbsf) for shore-based analyses of oxygen isotopes, deuterium, and chlorinity at high precision. Before squeezing, samples were removed from the core liner and the outside surfaces were carefully scraped off with spatulas to minimize potential contamination. Whole rounds were placed into a titanium and steel squeezing device and squeezed at ambient temperature with a hydraulic press. Interstitial water samples were collected in plastic syringes, filtered through 0.45- μ m Gelman polysulfone disposable filters, and stored in plastic sample tubes for shipboard analyses or archived in glass ampoules and/or heat-sealed acid-washed plastic tubes for shore-based analysis.

Interstitial water analyses followed the procedures outlined by Gieskes et al. (1991) and Murray et al. (2000) with modifications as indicated. Interstitial water samples were analyzed for salinity with a handheld refractometer; for pH and alkalinity by Gran titration with a Brinkman pH electrode and Metrohm autotitrator; for Cl^- concentrations by titration; for SO_4^{2-} concentrations by ion chromatography with a Dionex DX-120 ion chromatograph; for H_4SiO_4 , HPO_4^{2-} , and NH_4^+ concentrations by spectrophotometric methods with a Milton Roy Spectronic 301 spectrophotometer; for Na^+ , Mg^{2+} , Ca^{2+} , and K^+ by ion chromatograph (Site 1232) or by inductively coupled plasma-atomic emission spectroscopy (ICP-AES) with a Jobin Yvon JY2000; and for Mn^{2+} , Fe^{2+} , B , Sr^{2+} , Ba^{2+} , and Li^+ by ICP-AES. Sample and standard aliquots used for HPO_4^{2-} determinations were acidified with 1-N HCl to a pH <2 to avoid analytical artifacts related to the possible presence of hydrogen sulfide in interstitial water samples. ICP-AES techniques for the major cations Na^+ , Mg^{2+} , Ca^{2+} , and K^+ used dilutions of International Association of Physical Sciences Organization (IAPSO) standard seawater as calibration standards. Standards and samples were diluted 1:5 with

distilled water then 1:10 with a 2.5% HNO₃ (by volume) matrix solution with yttrium at 10 ppm as an internal standard. Because of the matrix influence of variable Na⁺ in IAPSO dilutions on K⁺ intensity, K⁺ calibration curves were constructed using only a blank and the 100% IAPSO dilution. ICP-AES techniques for the minor elements Mn²⁺, Fe²⁺, B, Sr²⁺, Ba²⁺, and Li⁺ were modified from those described by Murray et al. (2000) by preparing calibration standards in an acidified (2.5% HNO₃, by volume) sodium chloride matrix (35 g NaCl/L) and by using the 2.5% HNO₃ matrix solution with yttrium at 10 ppm as an internal standard to dilute standards and acidified interstitial water samples 1:10 for each analytical run.

IAPSO standard seawater was used for calibrating techniques when applicable. The accuracy of techniques was assessed by determining IAPSO or solutions of known composition as samples and calculating the measured/expected value as a ratio. The reproducibility of techniques, expressed as 1-σ relative standard deviations of means, was evaluated by replicate analyses of drift solutions similar in composition to samples, of IAPSO treated as a sample, and/or of samples both within a given analytical run and in different analytical runs (Table T7). Na⁺ was also determined by charge balance, neglecting contributions by ammonium and bromide, with the charge balance values reported here. Chemical data for interstitial water are reported in molar concentration units in each site report.

Sedimentary Inorganic Carbon and Organic Carbon, Nitrogen, and Sulfur Concentrations

Inorganic carbon concentrations were determined using a Coulometrics 5011 carbon dioxide coulometer equipped with a System 140 carbonate analyzer. One carbonate determination was performed typically for each 1.5-m section of core. Samples of ~15 mg of freeze-dried, ground sediment were reacted with 2-N HCl. The liberated CO₂ was backtitrated to a colorimetric end point. Calcium carbonate content, as weight percent, was calculated from the inorganic carbon (IC) content with the assumption that all inorganic carbon is present as calcium carbonate:

$$\% \text{CaCO}_3 = \% \text{IC} \times 8.33.$$

Ten replicate analyses of aliquots from a high calcium carbonate sample (202-1236A-3H-3, 74–75 cm) range from 95.5 to 96.1 wt% (mean = 95.8 wt%; standard deviation = 0.2 wt%) (Table T8).

Total carbon, total nitrogen, and total sulfur were determined using a Carlo Erba 1500 CNS Analyzer on a subset of the samples used for inorganic carbon determinations. Aliquots of 10 mg of freeze-dried, ground sediment with ~10 mg V₂O₅ oxidant were combusted at 1000°C in a stream of oxygen. Nitrogen oxides were reduced to N₂, and the mixture of N₂, CO₂, H₂O, and SO₂ gases was separated by GC and detection performed by TCD. The H₂ values are not useful because they represent hydrogen from both organic matter (OM) and (clay) minerals. All measurements were calibrated by comparison to pure sulfanilamide as standard. Contents of TOC, as weight percent, were calculated as the difference between total carbon (TC) and inorganic carbon (IC):

$$\% \text{TOC} = \% \text{TC} - \% \text{IC}.$$

T7. Interstitial water geochemical analysis, p. 73.

T8. Results of CaCO₃ replicate analyses, p. 74.

No formal assessment of analytical precision for organic carbon determinations by difference was made (e.g., by multiple measurements of a single sample). An earlier comparison of total organic carbon determinations by difference made shipboard with shore-based analysis of the same samples on the carbonate-free fraction found that shipboard organic carbon determinations for Iberia Abyssal Plain sediments (total organic carbon typically up to 1 wt%, some as high as 2.5 wt%) were systematically low relative to shore-based measurements (Meyers and Silliman, 1996). One-third of the samples agreed within 0.1 wt%, but differences ranged from <0.1 wt% to 0.5 wt% and occasionally much greater (1 wt% or more). Assuming that typical absolute error on calcium carbonate determinations is ± 0.2 wt% (see Table T8) (equivalent to an absolute error of about ± 0.02 wt% for inorganic carbon), estimates of possible errors in total carbon determinations allow the estimation of errors in total organic carbon. For example, a sample with 75 wt% calcium carbonate and 1 wt% total organic carbon would have absolute errors in total organic carbon of ± 0.03 – 0.10 wt% if total carbon determinations had relative errors of $\pm 0.02\%$ – 1.0% relative standard deviation. For a sample with 8.3 wt% calcium carbonate and 1.0 wt% total organic carbon, absolute errors would be ± 0.02 – 0.03 wt% for the same range of relative errors in total carbon determinations. The errors in total carbon are not defined, so these estimates of errors in total organic carbon by difference should be used only as a guide.

Organic matter atomic carbon/nitrogen ratios were calculated from TOC and total nitrogen concentrations to characterize the nature of the organic matter (i.e., to distinguish between marine and terrigenous sources) (Meyers, 1997).

The type of organic matter was characterized in a selected set of samples (organic carbon-rich sediments) by pyrolysis using a Delma Nermag Rock-Eval II pyrolysis system. This method is based on a whole-rock pyrolysis technique to identify the type and the maturity of the organic matter and to detect the petroleum potential of the sediments (Espitalié et al., 1986). The Rock-Eval system includes a temperature program that first releases volatile hydrocarbons (S_1 peak) at 300°C for 3 min. Then, hydrocarbons are released through thermal cracking of kerogens (S_2 peak) as the temperature is increased from 300° to 550°C at 25°C/min. S_1 and S_2 parameters are measured with an FID and are reported in milligrams per gram of sediment. The temperature at which the kerogen yields the maximum amount of hydrocarbons during the S_2 program provides T_{max} , a parameter that indicates the maturity of the organic matter. Between 300° and 390°C of the pyrolysis program, CO_2 released from the thermal degradation of organic matter (S_3 peak) is trapped and measured by TCD in milligrams per gram of sediment. Rock-Eval II parameters characterize organic matter by allowing the hydrogen index (HI; in milligrams of hydrogen per gram of organic carbon) to be calculated:

$$HI = S_2 \times 100/TOC.$$

Interpretation of Rock-Eval data is considered to be unreliable for samples containing <0.5 wt% TOC (Peters, 1986).

DOWNHOLE MEASUREMENTS

Downhole logs provide continuous in situ geophysical parameters within a borehole. These measurements are used to assess the physical, chemical, and structural characteristics of formations penetrated by drilling and thus provide a means of reconstructing the stratigraphy, lithology, and mineralogy of a sequence.

Well logging is typically undertaken in the deepest hole drilled at any one site. Where core recovery is poor or disturbed, downhole logs are often the most reliable source of information; where core recovery is good, core data can be correlated with log data to refine stratigraphy and unit characterization.

Downhole logging operations begin after the hole has been cored and flushed with a viscous drilling fluid. The drilling assembly is then pulled up to ~70 mbsf, and the logging tools are passed through the drill pipe into the open hole. The logging tools are joined together into tool strings so that compatible tools are run together. Each tool string is lowered separately to the base of the hole, and then measurement takes place as the tool string is raised at a constant rate between 275 and 500 m/hr (see “Downhole Measurements” in the individual site chapters). A wireline heave compensator is used to minimize the effect of the ship’s heave on the tool position in the borehole (Goldberg, 1990).

Tool String Configurations

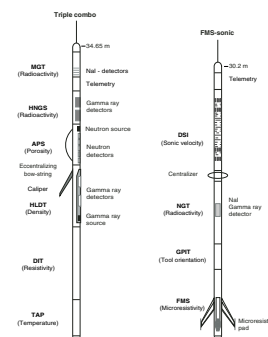
Two tool strings, composed of a variety of Schlumberger and Lamont-Doherty Earth Observatory (LDEO) tools, were deployed during Leg 202:

1. The triple combination (triple combo) tool string, which includes resistivity (Dual Induction Tool [DIT]), density (Hostile Environment Litho-Density Tool [HLDT]), and porosity (Accelerator Porosity Sonde [APS]), with two LDEO tools, the Multi-Sensor Spectral Gamma Ray Tool (MGT) for high-resolution gamma ray measurements and the high-resolution Temperature/Acceleration/Pressure (TAP) tool and
2. The Formation MicroScanner (FMS) for resistivity images of the borehole wall and the sonic velocity (Dipole Sonic Imager [DSI]) tool.

Each tool string contains a telemetry cartridge facilitating communication from the tools along the wireline (seven-conductor cable) to the Schlumberger Minimum Configuration Maxis (MCM) unit located on the drillship. A natural gamma radiation tool is also included on all tool strings in order to provide a common reference for correlation and depth shifting between multiple logging runs. Further tool details are found in Figure F13 and Table T9.

During each logging run, incoming data were recorded and monitored in real time on the MCM logging computer. The MGT is not a Schlumberger tool and cannot record data while the Schlumberger tools are active. Thus, the MGT requires separate passes for data acquisition, during which time control of the wireline transfers to the LDEO logger and data are recorded, in real time, on the specialized acquisition system in the downhole measurements laboratory.

F13. Tool strings run during Leg 202, p. 64.



T9. Specifications of logging tools, p. 75.

Logged Sediment Properties and Tool Measurement Principles

The main logs acquired by the tools are listed in Table T10. A brief description of the measurement methods and the logged properties is given below. More detailed information on individual tools and their geological applications may be found in Ellis (1987), Goldberg (1997), Lovell et al. (1998), Rider (1996), Schlumberger (1989, 1994), and Serra (1984, 1986, 1989).

Natural Radioactivity

Three wireline spectral gamma ray tools were used to measure and classify natural radioactivity in the formation: the Natural Gamma Ray Spectrometry Tool (NGT), the Hostile Environment Gamma Ray Sonde (HNGS) and the LDEO MGT. The NGT uses a sodium iodide scintillation detector and five-window spectroscopy to determine concentrations of K (in weight percent), Th (in parts per million), and U (in parts per million), the three elements whose isotopes dominate the spectrum of natural radiation. The HNGS is similar to the NGT, but it uses two bismuth germanate scintillation detectors for significantly improved tool precision. It also filters out gamma ray energies below 500 keV, eliminating sensitivity to bentonite or KCl in the drilling mud and improving measurement accuracy. Although the NGT response is sensitive to borehole diameter and the weight and concentration of bentonite or KCl present in the drilling mud, corrections for these effects are routinely made during processing at LDEO.

The MGT was developed by the LDEO Borehole Research Group to improve the vertical resolution of natural gamma ray logs by using an array of four short detector modules with 60-cm spacing. Each module comprises a small 2 in \times 4 in NaI detector, a programmable 256-channel amplitude analyzer, and an ^{241}Am calibration source. The spectral data are subsequently recalculated to determine the concentration of K, Th, and U radioisotopes or their equivalents. The spectral data from individual modules are sampled four times per second and stacked in real time based on the logging speed. This approach increases vertical resolution by a factor of two to three over conventional tools, while preserving comparable counting efficiency and spectral resolution. The radius of investigation depends on several factors: hole size, mud density, formation bulk density (denser formations display a slightly lower radioactivity), and the energy of the gamma rays (a higher-energy gamma ray can reach the detector from deeper in the formation). The MGT also includes an accelerometer channel to improve data stacking by the precise measurement of logging speed. Postcruise corrections for borehole size and tool sticking, based, respectively, on the caliper and acceleration data, are possible.

Formation density was determined with the HLDT. The tool contains a radioactive cesium (^{137}Cs) gamma ray source (622 keV) and far and near gamma ray detectors mounted on a shielded skid, which is pressed against the borehole. Gamma rays emitted by the source undergo Compton scattering, which involves the transfer of energy from gamma rays to the electrons in the formation via elastic collisions. The number of scattered gamma rays that reach the detectors is directly related to the density of electrons in the formation, which is in turn related to bulk density. Porosity may also be derived from this bulk density if the matrix (grain) density is known.

T10. Logging tool and measurement acronyms and units of measurement, p. 76.

The HLDT also measures photoelectric absorption as the photoelectric effect (PEF). Photoelectric absorption of the gamma rays occurs when they reach <150 keV after being repeatedly scattered by electrons in the formation. As the PEF depends on the atomic number of the elements in the formation, it also varies according to the chemical composition of the minerals present. For example, the PEF of calcite = 5.08 b/e⁻; illite = 3.03 b/e⁻; quartz = 1.81 b/e⁻; and kaolinite = 1.49 b/e⁻. Good contact between the tool and borehole wall is essential for acquisition of quality HLDT logs; poor contact results in an underestimation of density values.

Porosity

Formation porosity was measured with the APS. The sonde incorporates a minitron neutron generator that produces fast neutrons (14.4 MeV) and five neutron detectors (four epithermal and one thermal) positioned at differing intervals from the minitron. The measurement principle involves counting neutrons that arrive at the detectors after being slowed by neutron absorbers surrounding the tool. The highest energy loss occurs when neutrons collide with hydrogen nuclei, which have practically the same mass as the neutron (the neutrons simply bounce off heavier elements without losing much energy). If hydrogen concentration is low, as in low-porosity formations, neutrons can travel farther before being captured, and the count rates increase at the detector. The opposite effect occurs when the water content is high. However, because hydrogen bound in minerals such as clays or in hydrocarbons also contributes to the measurement, the raw porosity value is often an overestimate.

Upon reaching thermal energies (0.025 eV), the neutrons are captured by the nuclei of Cl, B, Cd, and other rare earth and trace elements with large capture cross sections, resulting in a gamma ray emission. This neutron capture cross section (Σf) is also measured by the tool.

Electrical Resistivity

The DIT was used to measure electrical resistivity. The DIT provides three measures of electrical resistivity, each with a different depth of investigation. The two induction devices (deep and medium depths of penetration) transmit high-frequency alternating currents through transmitter coils, creating magnetic fields that induce secondary currents in the formation. These currents produce a new inductive signal, proportional to the conductivity of the formation, which is measured by the receiving coils. The measured conductivities are then converted to resistivity (measured in ohm-meters). For the shallow penetration resistivity, the current necessary to maintain a constant voltage drop across a fixed interval is measured; it is a direct measurement of resistivity. Sand grains and hydrocarbons are electrical insulators, whereas ionic solutions and clays are more conductive. Electrical resistivity can therefore be used to evaluate porosity (via Archie's Law) if fluid salinity is known.

Temperature, Acceleration, and Pressure

Downhole temperature, acceleration, and pressure were measured with the LDEO high-resolution TAP tool run in memory mode. The tool uses fast- and slow-response thermistors to detect borehole fluid tem-

perature at two different rates. The fast-response thermistor detects small, abrupt changes in temperature, whereas the slow-response thermistor more accurately estimates temperature gradients and thermal regimes. A pressure transducer is used to activate the tool at a specified depth, typically 200 m above seafloor. A three-axis accelerometer measures tool movement downhole, providing data for analyzing the effects of heave on a deployed tool string. The acceleration log can aid in deconvolving heave effects postcruise.

The elapsed time between the end of drilling and the logging operation is generally not sufficient to allow the borehole to reach thermal equilibrium following circulation of the drilling fluid. Nevertheless, it is possible to identify abrupt temperature changes that may represent localized fluid flow into the borehole, indicative of fluid pathways and fracturing and/or breaks in the temperature gradient that may correspond to contrasts in permeability at lithologic boundaries.

Acoustic Velocity

The DSI measures the transit times between sonic transmitters and an array of eight receivers. It averages replicate measurements, thus providing a direct measurement of sound velocity through sediments that is relatively free from the effects of formation damage and borehole enlargement (Schlumberger, 1989). The tool contains the monopole transmitters found on most sonic tools but also has two crossed dipole transmitters, providing shear wave velocity measurement in addition to the compressional wave velocity, even in the slow formations typically encountered during ODP legs.

Formation MicroScanner

The FMS provides high-resolution electrical resistivity–derived images of the borehole (~30% of a 25-cm diameter borehole on each pass). The tool uses four orthogonal imaging pads, each containing 16 button electrodes that are pressed against the borehole wall during the recording (Fig. F13). A focused current is emitted from the button electrodes into the formation, with a return electrode near the top of the tool. The intensity of current passing through the button electrodes is measured and converted to an image.

With the FMS tool, features such as bedding, fracturing, slump folding, and bioturbation can be resolved, and spatially oriented images allow fabric analysis and bed orientations to be measured (Luthi, 1990; Lovell et al., 1998; Salimullah and Stow, 1992).

The maximum extension of the caliper arms is 15 in, so in holes or parts of holes where the diameter is larger the pad contact will be inconsistent and the FMS images may appear out of focus and too conductive. Irregular borehole walls will also adversely affect the image quality if it leads to poor pad-wall contact.

Accelerometry and Magnetic Field Measurement

Three-component acceleration and magnetic field measurements were made with the General Purpose Inclinometer Tool (GPIT). The primary purpose of this tool, which incorporates a three-component accelerometer and a three-component magnetometer, is to determine the acceleration and orientation of the FMS-sonic tool string during logging. This provides a means of correcting the FMS images for irregular tool

motion, allowing the true dip and direction (azimuth) of structures to be determined.

Log Data Quality

The quality of the log data depends primarily on borehole conditions. Large-diameter or irregular boreholes can lead to problems with measurements requiring contact with the borehole wall (e.g., FMS, density, and porosity tools). Deep investigation measurements such as resistivity and sonic velocity, which do not require contact with the borehole wall, are generally less sensitive to borehole conditions. Very narrow (“bridged”) sections will also cause irregular log results. The quality of the borehole is improved by minimizing the circulation of drilling fluid while drilling, flushing the borehole to remove debris, and logging as soon as possible after drilling and hole conditioning are completed.

Log Depth Scales

The depth of the wireline-logged measurement is determined from the length of the logging cable played out at the winch on the ship. The seafloor is identified on the natural gamma log by the abrupt reduction in gamma ray count at the water/sediment boundary (mudline). Discrepancies between the driller’s depth and the wireline log depth occur because of incomplete heave compensation, tidal changes, and cable stretch (~1 m/km) in the case of log depth. The small differences between drill pipe depth and logging depth, and the even more significant discrepancy between ODP curation depth and logging depth, should be taken into account when using the logs for correlation between core and log data. Core measurements such as susceptibility and density can be correlated with the equivalent downhole logs using the Sagan program, which allows linear shifting of the core depths onto the log depth scale.

Data Processing

Data are transferred to the downhole measurements laboratory for preliminary interpretation. Basic processing is carried out postcruise to provide scientists with a comprehensive quality-controlled downhole logging data set that can be used for comparison, integration, and correlation with other data collected during Leg 202 and other ODP legs. The processing includes depth adjustments to remove depth offsets between data from different logging runs, corrections specific to certain tools and logs, documentation for the logs (with an assessment of log quality), and conversion of the data to a widely accessible format (ASCII for the conventional logs and GIF for the FMS images). Schlumberger GeoQuest’s GeoFrame software package is used for most of the processing.

Processed acoustic, caliper, density, gamma ray, magnetic, neutron porosity, resistivity, and temperature data are available in ASCII.

AGE MODELS AND MASS ACCUMULATION RATES

Biostratigraphic, paleomagnetic, and other data, if available, were used to construct age-depth models for Leg 202 sites. The models are tabulated in the site chapters and plotted along with all reliable age control points from which the models were derived. The mcd depths were used for each site (see “[Composite Section](#),” p. 4).

Linear sedimentation rates (LSRs) were calculated for regular time intervals, and corrected LSRs were computed to compensate for the growth rates inherent in the mcd depth scale. Dry density data were used to convert corrected LSRs to total MARs. Carbonate concentration data (and in one case TOC and biogenic opal concentrations) were used to estimate carbonate (and TOC and opal) MARs.

Plots of all age-depth models, LSRs, and MARs were prepared for each site that had sufficient age-depth control datums to allow construction of an age model (Sites 1233 and 1236–1242). The results were briefly discussed in the site chapters and in the leg summary.

Age-Depth Model

Shipboard age models are constructed under considerable time pressure and are afflicted with uncertainties that mainly result from a limited number of age control points, the quality and depth range of a datum, and the age itself. Each datum event has an age uncertainty that may vary from a few thousand years to several hundred thousands of years. The ages of individual datums calibrated elsewhere may not necessarily apply to a given site and this introduces an additional age uncertainty for some datums. Biostratigraphic sampling is often limited to one per core (i.e., a sample interval of ~10 m), which results in significant depth uncertainties for the datums. Reworking and dissolution may render some microfossil groups less reliable than others as a function of sediment composition and diagenesis. Thus, inconsistencies are frequent. Precise paleomagnetic datums were provided for some of the sites where chrons and polarity reversal boundaries could be clearly identified and calibrated with biostratigraphic datums.

The common biostratigraphic and polarity reversal approach provided no age control points for the upper Pleistocene to Holocene high-resolution records at Sites 1233–1235. However, Site 1233 provided an unprecedented record of centennial to millennial scale variability in paleomagnetic intensities, which are a powerful tool of global extent for stratigraphy. Additional Holocene age control points at Site 1233 were derived from correlation with a nearby sediment core, using magnetic susceptibility core logging data, and mapping of the ^{14}C datums obtained for that sediment core to Site 1233.

Given all these circumstances, the construction of age-depth models is to some degree a subjective process and represents a preliminary first approximation of the true age-depth relationship. We applied a procedure resulting in conservative shipboard age models that satisfy as many constraints as possible without introducing artificial or speculative features in the model. The starting point was a plot of all control points from biostratigraphy, paleomagnetism, or other sources if available. Age and depth uncertainties were presented with error bars. Age ranges are rarely reported for biostratigraphic datums, but depth ranges can be calculated from the samples that were analyzed. Obvious outliers

and conflicting datums were then masked until the line connecting the remaining control points was reasonably smooth. A smooth curve was fit to these points using locally weighted (10% of data) least-squares (Stineman function). The curve fit eliminates artificial kinks in the model that are functions of where a tie point was chosen within a depth range. A further step was used at some sites, including depth shifting of some control points to make the curve fit pass through more data points (their areas of uncertainty) or to constrain hiatuses. The final shipboard age model was as conservative as possible, preserving inflections in the age-depth curve that are supported by the data and smoothing those that are likely artifacts.

Paleomagnetic data, if available, were usually given first priority in constraining the age-depth model in case of conflicting datums, followed by calcareous nannofossils, planktonic foraminifers, and diatoms. In cases of conflicting microfossil datums we also took into account the reliability of individual datums as global dating tools, the stratigraphic reliability of fossil groups or specific datums, abundance, preservation, and reworking, if indicated, and the uncertainties associated with the first or last occurrence of a datum (first occurrence datums are generally preferred).

The age models were presented as plots of original datums with error bars overlain by the final shipboard age model, and tabulated as age-depth series, in each site chapter. These age models will undoubtedly be refined and replaced by detailed postcruise analysis.

Linear Sedimentation Rates and Mass Accumulation Rates

Once the final shipboard age model is defined, calculating and plotting LSRs and MARs is a process that involves a number of simple interpolations and computations. The only subjective part of this process is the initial selection of time intervals at which the smooth age model is sampled. Instead of calculating LSRs and MARs over intervals given by the original stratigraphic control points, we decided to choose regular and conservative time intervals. As a rule of thumb, a time interval should include and average at least three age control points. For Site 1236–1239 and 1241, a 1-m.y. window was used so the results could be compared conveniently between sites. A 0.4-m.y. window was used for the high-resolution Sites 1240 and 1242, and a 10-k.y. window was used for Site 1233, which has an extremely high sedimentation rate. It should be kept in mind that the time series is an arbitrary choice of an average sampling rate and does not reflect the resolution of the age model equally in all intervals. However, in conjunction with a smooth age model, it presents the most realistic and conservative trends in LSRs and MARs.

First, the smooth age model was sampled at the age series points to obtain interpolated depths in mcd for those ages. LSRs in meters per million years were then calculated as the first derivative of the age-depth series over the selected interval. The LSRs were subsequently corrected to compensate for the expansion of the recovered sediment sequence represented by the mcd scale (see “**Composite Section**,” p. 4). This correction was made by dividing the LSR by the appropriate growth factor for each depth interval.

In preparation for computing the MARs, dry density obtained from moisture and density measurements (see “**Physical Properties**,” p. 16) and carbonate concentration data (see “**Geochemistry**,” p. 32) were

plotted against mcd and outliers were removed. Ages were interpolated for each depth point using the shipboard age model. The dry density and carbonate values were averaged over the regular age intervals. This averaging step is important to avoid a commonly introduced bias that occurs when dry density data at relatively high age/depth resolution are multiplied by LSRs calculated at a much lower resolution. Such a bias gives the impression that we know the MAR variations at great age/time and amplitude resolution when, in fact, associated LSR variations may tend to compensate for the dry density variations (higher dry density typically results in lower LSR). The generally low resolution of LSRs determines the resolution of MAR variations, even if the available dry density record has a much higher resolution.

After correcting LSR values for the growth factor and averaging dry densities over the appropriate interval, MARs were calculated using the equation

$$\text{Bulk MAR (g/cm}^2\text{/k.y.)} = \text{LSR (m/m.y.)} \times \text{dry density (g/cm}^3\text{)}/10.$$

Component MARs were calculated by multiplying the bulk MAR by the concentration of the appropriate component (such as calcium carbonate).

Finally, a step plot of LSR, total MAR, and carbonate MAR summarizes the data. Although a smooth plot through the midpoints of the age intervals would convey the same information, we preferred the step plot because it illustrates clearly the selected age resolution that we considered to be reasonable and conservative.

REFERENCES

- Abrantes, F., 1988. Diatom assemblages as upwelling indicators in surface sediments off Portugal. *Mar. Geol.*, 85:15–39.
- , 2000. 200 ka diatom records from Atlantic upwelling sites reveal maximum productivity during LGM and a shift in phytoplankton community structure at 185 ka. *Earth Planet. Sci. Lett.*, 176:7–16.
- Abrantes, F., and Moita, T., 1999. Water column and recent sediment data on diatoms and coccolithophorids, off Portugal, confirm sediment record as a memory of upwelling events. *Oceanol. Acta*, 22:319–336.
- ASTM, 1985. Standard method for computing the colors of objects by using the CIE system. *Annual Book of ASTM Standards*: Philadelphia (Am. Soc. Testing and Mater.), E308.
- , 1990. Standard method for laboratory determination of water (moisture) content of soil and rock. *Annual Book of ASTM Standards* (Vol. 04.08): Philadelphia (Am. Soc. Testing and Mater.), D 2216–90 (revision of 2216–63, 2216–80).
- , 1993. Standard test method for determination of thermal conductivity of soil and soft rock by thermal needle probe procedure. *Annual Book of ASTM Standards*: Philadelphia (Am. Soc. Testing and Mater.), D5334–92.
- Backman, J., and Raffi, I., 1997. Calibration of Miocene nannofossil events to orbitally tuned cyclostratigraphies from Ceara Rise. In Shackleton, N.J., Curry, W.B., Richter, C., and Bralower, T.J. (Eds.), *Proc. ODP, Sci. Results*, 154: College Station, TX (Ocean Drilling Program), 83–99.
- Baldauf, J.G., 1984. Cenozoic diatom biostratigraphy and paleoceanography of the Rockall Plateau region, North Atlantic, Deep Sea Drilling Project Leg 81. In Roberts, D.G., Schnitker, D., et al., *Init. Repts. DSDP*, 81: Washington (U.S. Govt. Printing Office), 439–478.
- , 1985. A high resolution late Miocene–Pliocene diatom biostratigraphy for the eastern equatorial Pacific. In Mayer, L., Theyer, F., Thomas, E., et al., *Init. Repts. DSDP*, 85: Washington (U.S. Govt. Printing Office), 457–475.
- Baldauf, J.G., and Iwai, M., 1995. Neogene diatom biostratigraphy for the eastern equatorial Pacific Ocean, Leg 138. In Pisias, N.G., Mayer, L.A., Janecek, T.R., Palmer-Julson, A., and van Andel, T.H. (Eds.), *Proc. ODP, Sci. Results*, 138: College Station, TX (Ocean Drilling Program), 105–128.
- Balsam, W.L., and Damuth, J.E., 2000. Further investigations of shipboard vs. shore-based spectral data: implications for interpreting Leg 164 sediment composition. In Paull, C.K., Matsumoto, R., Wallace, P., and Dillon, W.P. (Eds.), *Proc. ODP, Sci. Results*, 164: College Station, TX (Ocean Drilling Program), 313–324.
- Balsam, W.L., Damuth, J.E., and Schneider, R.R., 1997. Comparison of shipboard vs. shore-based spectral data from Amazon-Fan cores: implications for interpreting sediment composition. In Flood, R.D., Piper, D.J.W., Klaus, A., and Peterson, L.C. (Eds.), *Proc. ODP, Sci. Results*, 155: College Station, TX (Ocean Drilling Program), 193–215.
- Balsam, W.L., and Deaton, B.C., 1996. Determining the composition of late Quaternary marine sediments from NUV, VIS, and NIR diffuse reflectance spectra. *Mar. Geol.*, 134:31–55.
- Balsam, W.L., Deaton, B.C., and Damuth, J.E., 1998. The effects of water content on diffuse reflectance measurements of deep-sea core samples: an example from ODP Leg 164 sediments. *Mar. Geol.*, 149:177–189.
- Balsam, W.L., Otto-Bliesner, B.L., and Deaton, B.C., 1995. Modern and last glacial maximum eolian sedimentation patterns in the Atlantic Ocean interpreted from sediment iron oxide content. *Paleoceanography*, 10:493–507.
- Balsam, W.L., and Wolhart, R., 1993. Sediment dispersal in the Argentine Basin: evidence from visible light spectra. *Deep-Sea Res. Part A*, 40:1001–1031.

- Barron, J.A., 1980. Upper Pliocene and Quaternary diatom biostratigraphy of Deep Sea Drilling Project Leg 54, tropical eastern Pacific. *In* Rosendahl, B.R., Hekinian, R., et al., *Init. Repts. DSDP*, 54: Washington (U.S. Govt. Printing Office), 455–485.
- , 1981. Late Cenozoic diatom biostratigraphy and paleoceanography of the middle-latitude eastern North Pacific, Deep Sea Drilling Project Leg 63. *In* Yeats, R.S., Haq, B.U., et al., *Init. Repts. DSDP*, 63: Washington (U.S. Govt. Printing Office), 507–538.
- , 1983. Latest Oligocene through early middle Miocene diatom biostratigraphy of the eastern tropical Pacific. *Mar. Micropaleontol.*, 7:487–515.
- , 1985a. Late Eocene to Holocene diatom biostratigraphy of the equatorial Pacific Ocean, Deep Sea Drilling Project Leg 85. *In* Mayer, L., Theyer, F., Thomas, E., et al., *Init. Repts. DSDP*, 85: Washington (U.S. Govt. Printing Office), 413–456.
- , 1985b. Miocene to Holocene planktic diatoms. *In* Bolli, H.M., Saunders, J.B., and Perch-Nielsen, K. (Eds.), *Plankton Stratigraphy*: Cambridge (Cambridge Univ. Press), 763–809.
- , 1992. Neogene diatom datum levels in the equatorial and North Pacific. *In* Ishizaki, K., and Saito, T. (Eds.), *The Centenary of Japanese Micropaleontology*: Tokyo (Terra Sci. Publ.), 413–425.
- Berelson, W.M., Hammond, D.E., and Johnson, K.S., 1987. Benthic fluxes and the cycling of biogenic silica and carbon in two southern California borderland basins. *Geochim. Cosmochim. Acta*, 51:1345–1363.
- Berggren, W.A., Hilgen, F.J., Langereis, C.G., Kent, D.V., Obradovich, J.D., Raffi, I., Raymo, M.E., and Shackleton, N.J., 1995a. Late Neogene chronology: new perspectives in high-resolution stratigraphy. *Geol. Soc. Am. Bull.*, 107:1272–1287.
- Berggren, W.A., Kent, D.V., Swisher, C.C., III, and Aubry, M.-P., 1995b. A revised Cenozoic geochronology and chronostratigraphy. *In* Berggren, W.A., Kent, D.V., Aubry, M.-P., and Hardenbol, J. (Eds.), *Geochronology, Time Scales and Global Stratigraphic Correlation*. Spec. Publ.—SEPM, 54:129–212.
- Blackwell, J.M., 1954. A transient flow method for determination of thermal constants of insulating material in bulk. *J. Appl. Phys.*, 25:137.
- Blum, P., 1997. Physical properties handbook: a guide to the shipboard measurement of physical properties of deep-sea cores. *ODP Tech. Note*, 26 [Online]. Available from World Wide Web: <<http://www-odp.tamu.edu/publications/tnotes/tn26/INDEX.HTM>>. [Cited 2002-03-25]
- Bolli, H.M., and Saunders, J.B., 1985. Oligocene to Holocene low latitude planktic foraminifera. *In* Bolli, H.M., Saunders, J.B., and Perch-Nielsen, K. (Eds.), *Plankton Stratigraphy*: Cambridge (Cambridge Univ. Press), 155–262.
- Bukry, D., 1973. Low-latitude coccolith biostratigraphic zonation. *In* Edgar, N.T., Saunders, J.B., et al., *Init. Repts. DSDP*, 15: Washington (U.S. Govt. Printing Office), 685–703.
- , 1975. New Miocene to Holocene stages in the ocean basins based on calcareous nannoplankton zones. *In* Kulm, L.D., von Huene, R., et al. (Eds.), *Late Neogene Epoch Boundaries*: New York (Am. Mus. Nat. Hist., Micropaleontology Press), 162–166.
- Bukry, D., and Foster, J.H., 1973. Silicoflagellate and diatom stratigraphy, Leg 16, Deep Sea Drilling Project. *In* van Andel, T.H., Heath, G.R., et al., *Init. Repts. DSDP*, 16: Washington (U.S. Govt. Printing Office), 815–871.
- Burckle, L.H., 1972. Late Cenozoic planktonic diatom zones from the eastern equatorial Pacific. *In* Simonsen, R. (Ed.), *First Symposium on Recent and Fossil Marine Diatoms*. Nova Hedwegia Beih., 39:217–246.
- , 1977a. Neogene diatom correlations in the Circum-Pacific. *Proc. 1st Int. Congress Pacific Neogene Stratigraphy*, 36–39.
- , 1977b. Pliocene and Pleistocene diatom datum levels from the equatorial Pacific. *Quat. Res.*, 7:330–340.

- , 1978. Early Miocene to Pliocene diatom datum level for the equatorial Pacific. *Proc. Second Working Group Mtg. Biostratigraphic Datum Planes, Pacific Neogene, IGCP Proj. 114*. Spec. Publ.—Geol. Res. Dev. Ctr., 1:25–44.
- Burckle, L.H., and Trainer, J., 1979. Middle and late Pliocene diatom datum levels from the central Pacific. *Micropaleontology*, 25:281–293.
- Cande, S.C., and Kent, D.V., 1995. Revised calibration of the geomagnetic polarity timescale for the Late Cretaceous and Cenozoic. *J. Geophys. Res.*, 100:6093–6095.
- Chaisson, W.P., and Pearson, P.N., 1997. Planktonic foraminifer biostratigraphy at Site 925: middle Miocene–Pleistocene. In Shackleton, N.J., Curry, W.B., Richter, C., and Bralower, T.J. (Eds.), *Proc. ODP, Sci. Results*, 154: College Station, TX (Ocean Drilling Program), 3–31.
- Curry, W.B., Shackleton, N.J., Richter, C., et al., 1995. *Proc. ODP, Init. Repts.*, 154: College Station, TX (Ocean Drilling Program).
- Deaton, B.C., and Balsam, W.L., 1991. Visible spectroscopy: a rapid method for determining hematite and goethite concentrations in geological materials. *J. Sediment. Petrol.*, 61:628–632.
- DeVries, D.A., and Peck, A.J., 1958. On the cylindrical probe method of measuring thermal conductivity with special reference to soils. *Aust. J. Phys.*, 11:255–271.
- Droser, M.L., and Bottjer, D.J., 1986. A semiquantitative field classification of ichnofabric. *J. Sediment. Petrol.*, 56:558–559.
- Dugdale, R.C., and Goering, J.J., 1967. Uptake of new and regenerated forms of nitrogen in primary productivity. *Limnol. Oceanogr.*, 12:196–206.
- Dunham, R.J., 1962. Classification of carbonate rocks according to depositional texture. In Ham, W.E. (Ed.), *Classification of Carbonate Rocks: AAPG Mem.*, 108–121.
- Ellis, D.V., 1987. *Well Logging for Earth Scientists*: New York (Elsevier).
- Embry, A.F., and Klovan, J.E., 1971. A late Devonian reef tract on northeastern Banks Island, Northwest Territories. *Bull. Can. Pet. Geol.*, 19:730–781.
- Espitalié, J., Deroo, G., and Marquis, F., 1986. La pyrolyse Rock-Eval et ses applications, Partie III. *Rev. Inst. Fr. Pet.*, 41:73–89.
- Evans, H.B., 1965. GRAPE—a device for continuous determination of material density and porosity. *Trans. SPWLA 6th Ann. Logging Symp.*: Dallas, 2:B1–B25.
- Gealy, E.L., 1971. Saturated bulk density, grain density, and porosity of sediment cores from the western Equatorial Pacific: Leg 7, *Glomar Challenger*. In Winterer, E.L., Riedel, W.R., et al., *Init. Repts. DSDP*, 7 (Pt. 2), Washington (U.S. Govt. Printing Office), 1081–1104.
- Gersonde, R., Hodell, D.A., Blum, P., et al., 1999. *Proc. ODP, Init. Repts.*, 177 [CD-ROM]. Available from: Ocean Drilling Program, Texas A&M University, College Station, TX 77845-9547, U.S.A.
- Gieskes, J., Gamo, T., and Brumsack, H.-J., 1991. Chemical methods for interstitial water analysis aboard *JOIDES Resolution*. *ODP Tech. Note*, 15.
- Giosan, L., 2001. The use of sediment color in paleoceanography: Pliocene–Pleistocene sedimentation in the western North Atlantic [Ph.D. dissert.]. State Univ. of New York, Stony Brook.
- Goldberg, D., 1990. Test performance of the Ocean Drilling Program wireline heave motion compensator. *Sci. Drill.*, 1:206–209.
- , 1997. The role of downhole measurements in marine geology and geophysics. *Rev. Geophys.*, 35:315–342.
- Hagelberg, T., Shackleton, N., Pisias, N., and Shipboard Scientific Party, 1992. Development of composite depth sections for Sites 844 through 854. In Mayer, L., Pisias, N., Janecek, T., et al., *Proc. ODP, Init. Repts.*, 138 (Pt. 1): College Station, TX (Ocean Drilling Program), 79–85.
- Hagelberg, T.K., Pisias, N.G., Shackleton, N.J., Mix, A.C., and Harris, S., 1995. Refinement of a high-resolution, continuous sedimentary section for studying equatorial Pacific Ocean paleoceanography, Leg 138. In Pisias, N.G., Mayer, L.A., Janecek, T.R., Palmer-Julson, A., and van Andel, T.H. (Eds.), *Proc. ODP, Sci Results*, 138: College Station, TX (Ocean Drilling Program), 31–46.

- Harms, J.C., and Choquette, P.W., 1965. Geologic evaluation of a gamma-ray porosity device. *Trans. SPWLA 6th Ann. Logging Symp.*: Dallas, C1–C37.
- Hayward, B.W., 2001. Global deep-sea extinctions during the Pleistocene ice-ages. *Geology*, 29:599–602.
- Holbourn, A.E., and Henderson, A., 2002. Re-illustration and revised taxonomy for selected deep-sea benthic foraminifers. *Paleontol. Electron.*, 4 [Online] Available from World Wide Web: <http://www.palaeo-electronica.org/2001_2/foram/issue2_01.htm>. [Cited 2002-01-31]
- Hutchings, L., Pitcher, G., Probyn, T., and Bailey, G., 1995. The chemical and biological consequences of coastal upwelling. In Summerhayes, C., Emeis, K.-C., Angel, M., Smith, R., and Zeitzschel, B. (Eds.), *Upwelling in the Ocean: Modern Processes and Ancient Records*: Berlin (John Wiley and Sons), 65–83.
- Jansen, E., Raymo, M.E., Blum, P., et al., 1996. *Proc. ODP, Init. Repts.*, 162: College Station, TX (Ocean Drilling Program).
- Jorissen, F.J., and Rohling, E.J., 2000 (Eds.). Foraminiferal proxies of paleoproductivity. *Spec. Issue Mar. Micropaleontol.*, 40:131–344.
- José, A.P., 1973. Diatoms in the Oligocene–Miocene biostratigraphic zones of the tropical areas of the Pacific Ocean. *Nova Hedwigia Beih.*, 45:333–357.
- Kanaya, T., 1971. Some aspects of pre-Quaternary diatoms in the Oceans. In Funnel, B., and Riedel, W. (Eds.), *The Micropaleontology of Oceans*: New York (Cambridge Univ. Press), 545–565.
- Katz, M.E., and Miller, K.G., 1991. Early Paleogene benthic foraminiferal assemblages and stable isotopes in the Southern Ocean. In Ciesielski, P.F., Kristoffersen, Y., et al., *Proc. ODP, Sci. Results*, 114: College Station, TX (Ocean Drilling Program), 481–512.
- Kennett, J.P., and Srinivasan, M.S., 1983. *Neogene Planktonic Foraminifera: A Phylogenetic Atlas*: Stroudsburg, PA (Hutchinson Ross).
- Kuhnt, W., Holbourn, A., and Zhao, Q., 2002. The early history of the South China Sea: evolution of Oligocene–Miocene deep water environments. *Rev. Micropaleontol.*, 45:99–159.
- Li, B., 1997. Paleooceanography of the Nansha Area, southern South China Sea since the last 700,000 years [Ph.D. dissert.]. Nanjing Inst. Geol. Paleontol., Academic Sinica, Nanjing, China.
- Loeblich, A.R., Jr., and Tappan, H., 1988. *Foraminiferal Genera and Their Classification*: New York (Van Nostrand Reinhold).
- Lovell, M.A., Harvey, P.K., Brewer, T.S., Williams, C., Jackson, P.D., and Williamson, G., 1998. Application of FMS images in the Ocean Drilling Program: an overview. In Cramp, A., MacLeod, C.J., Lee, S.V., and Jones, E.J.W. (Eds.), *Geological Evolution of Ocean Basins: Results from the Ocean Drilling Program*. Spec. Publ.—Geol. Soc. London, 131:287–303.
- Luthi, S.M., 1990. Sedimentary structures of clastic rocks identified from electrical borehole images. In Hurst, A., Lovell, M.A., and Morton, A.C. (Eds.), *Geological Applications of Wireline Logs*. Spec. Publ.—Geol. Soc. London, 48:3–10.
- Lyle, M., Koizumi, I., Richter, C., et al., 1997. *Proc. ODP, Init. Repts.*, 167: College Station, TX (Ocean Drilling Program).
- Margalef, R., 1978. Life-forms of phytoplankton as survival alternatives in an unstable environment. *Oceanol. Acta*, 1:493–509.
- Martini, E., 1971. Standard Tertiary and Quaternary calcareous nannoplankton zonation. In Farinacci, A. (Ed.), *Proc. 2nd Int. Conf. Planktonic Microfossils Roma*: Rome (Ed. Tecnosci.), 2:739–785.
- Mazzullo, J.M., Meyer, A., and Kidd, R.B., 1988. New sediment classification scheme for the Ocean Drilling Program. In Mazzullo, J., and Graham, A.G. (Eds.), *Handbook for Shipboard Sedimentologists*. ODP Tech. Note, 8:45–67.
- McKee, E.D., and Weir, G.W., 1953. Terminology for stratification and cross-stratification in sedimentary rocks. *Geol. Soc. Am. Bull.*, 64:381–390.
- Meyers, P.A., 1997. Organic geochemical proxies of paleoceanographic, paleolimnologic, and paleoclimatic processes. *Org. Geochem.*, 27:213–250.

- Meyers, P.A., and Silliman, J.E., 1996. Organic matter in Pleistocene to Quaternary turbidites from Sites 897, 898, 899, and 900, Iberia Abyssal Plain. *In* Whitmarsh, R.B., Sawyer, D.S., Klaus, A., and Masson, D.G. (Eds.), *Proc. ODP, Sci. Results*, 149: College Station, TX (Ocean Drilling Program), 305–313.
- Miller, K.G., and Katz, M.E., 1987. Oligocene to Miocene benthic foraminiferal and abyssal circulation changes in the North Atlantic. *Micropaleontology*, 33:97–149.
- Moran, K., 1997. Elastic property corrections applied to Leg 154 sediment, Ceara Rise. *In* Shackleton, N.J., Curry, W.B., Richter, C., and Bralower, T.J. (Eds.), *Proc. ODP, Sci. Results*, 154: College Station, TX (Ocean Drilling Program), 151–155.
- Muchina, V.V., 1971. Problems of diatom and silicoflagellate Quaternary stratigraphy in the equatorial Pacific Ocean. *In* Funnel, B.M., and Riedel, W.R. (Eds.), *The Micropalaeontology of Oceans*: Cambridge (Cambridge Univ. Press), 423–431.
- Munsell Color Company, Inc., 1994. *Munsell Soil Color Chart* (Revised ed.): Newburgh, MD (Munsell Color).
- Murray, R.W., Miller, D.J., and Kryc, K.A., 2000. Analysis of major and trace elements in rocks, sediments, and interstitial waters by inductively coupled plasma–atomic emission spectrometry (ICP-AES). *ODP Tech. Note*, 29 [Online]. Available from World Wide Web: <<http://www-odp.tamu.edu/publications/tnotes/tn29/INDEX.HTM>>. [Cited 2002-03-25]
- Okada, H., and Bukry, D., 1980. Supplementary modification and introduction of code numbers to the low-latitude coccolith biostratigraphic zonation (Bukry, 1973; 1975). *Mar. Micropaleontol.*, 5:321–325.
- Pearson, P.N., and Chaisson, W.P., 1997. Late Paleocene to middle Miocene planktonic foraminifer biostratigraphy of the Ceara Rise. *In* Shackleton, N.J., Curry, W.B., Richter, C., and Bralower, T.J. (Eds.), *Proc. ODP, Sci. Results*, 154: College Station, TX (Ocean Drilling Program), 33–68.
- Perch-Nielsen, K., 1985. Cenozoic calcareous nannofossils. *In* Bolli, H.M., Saunders, J.B., and Perch-Nielsen, K. (Eds.), *Plankton Stratigraphy*: Cambridge (Cambridge Univ. Press), 427–554.
- Peters, K.E., 1986. Guidelines for evaluating petroleum source rock using programmed pyrolysis. *AAPG Bull.*, 70:318–329.
- Pimmel, A., and Claypool, G., 2001. Introduction to shipboard organic geochemistry on the *JOIDES Resolution*. *ODP Tech. Note*, 30 [Online]. Available from World Wide Web: <<http://www-odp.tamu.edu/publications/tnotes/tn30/INDEX.HTM>>. [Cited 2002-01-31]
- Pujos, A., 1988. Spatio-temporal distribution of some Quaternary coccoliths. *Oceanol. Acta*, 11:65–77.
- Raffi, I., Backman, J., Rio, D., and Shackleton, N.J., 1993. Plio-Pleistocene nannofossil biostratigraphy and calibration to oxygen isotopes stratigraphies from Deep Sea Drilling Project Site 607 and Ocean Drilling Program Site 677. *Paleoceanography*, 8:387–408.
- Raffi, I., and Flores, J.-A., 1995. Pleistocene through Miocene calcareous nannofossils from eastern equatorial Pacific Ocean. *In* Pisias, N.G., Mayer, L.A., Janecek, T.R., Palmer-Julson, A., and van Andel, T.H. (Eds.), *Proc. ODP, Sci. Results*, 138: College Station, TX (Ocean Drilling Program), 233–286.
- Rider, M.H., 1996. *The Geological Interpretation of Well Logs* (2nd ed.): Caithness (Whittles Publishing).
- Rock-Color Chart Committee, 1991. *Rock Color Charts*. Geol. Soc. Am.
- Ruddiman, W.F., Cameron, D., and Clement, B.M., 1987. Sediment disturbance and correlation of offset holes drilled with the hydraulic piston corer: Leg 94. *In* Ruddiman, W.F., Kidd, R.B., Thomas, E., et al., *Init. Repts. DSDP*, 94 (Pt. 2): Washington (U.S. Govt. Printing Office), 615–634.
- Salimullah, A.R.M., and Stow, D.A.V., 1992. Application of FMS images in poorly recovered coring intervals: examples from ODP Leg 129. *In* Hurst, A., Griffiths, C.M., and Worthington, P.F. (Eds.), *Geological Application of Wireline Logs II*. Spec. Publ.—Geol. Soc. London, 65:71–86.

- Sancetta, C.A., 1983. Biostratigraphic and paleoceanographic events in the eastern equatorial Pacific: results of Deep Sea Drilling Project Leg 69. *In* Cann, J.R., Langseth, M.G., Honnorez, J., Von Herzen, R.P., White, S.M., et al., *Init. Repts. DSDP*, 69: Washington (U.S. Govt. Printing Office), 311–320.
- Schlager, W., and James, N.P., 1978. Low-magnesian calcite limestones forming at the deep-sea floor, Tongue of the Ocean, Bahamas. *Sedimentology*, 25:675–702.
- Schlumberger, 1989. *Log Interpretation Principles/Applications*: Houston (Schlumberger Educ. Services), SMP-7017.
- , 1994. *IPL Integrated Porosity Lithology*: Houston (Schlumberger Wireline and Testing), SMP-9270.
- Schrader, H., and Sorknes, R., 1990. Spatial and temporal variation of Peruvian coastal upwelling during the latest Quaternary. *In* Suess, E., von Huene, R., et al., *Proc. ODP, Sci. Results*, 112: College Station, TX (Ocean Drilling Program), 391–406.
- Schuette, G., 1980. Recent marine diatom taphocoenoses off Peru and off southwest Africa: reflection of coastal upwelling [dissert.]. Oregon State Univ., Corvallis.
- Schultheiss, P.J., and McPhail, S.D., 1989. An automated P-wave logger for recording fine-scale compressional wave velocity structures in sediments. *In* Ruddiman, W., Sarthein, M., et al., *Proc. ODP, Sci. Results*, 108: College Station, TX (Ocean Drilling Program), 407–413.
- Serra, O., 1984. *Fundamentals of Well-Log Interpretation* (Vol. 1): *The Acquisition of Logging Data*: Dev. Pet. Sci., 15A.
- , 1986. *Fundamentals of Well-Log Interpretation* (Vol. 2): *The Interpretation of Logging Data*. Dev. Pet. Sci., 15B.
- , 1989. *Formation MicroScanner Image Interpretation*: Houston (Schlumberger Educ. Services), SMP-7028.
- Shackleton, N.J., Baldauf, J.G., Flores, J.-A., Iwai, M., Moore, T.C., Jr., Raffi, I., and Vincent, E., 1995. Biostratigraphic summary for Leg 138. *In* Pias, N.G., Mayer, L.A., Janecek, T.R., Palmer-Julson, A., and van Andel, T.H. (Eds.), *Proc. ODP, Sci. Results*, 138: College Station, TX (Ocean Drilling Program), 517–536.
- Terry, R.D., and Chilingar, G.V., 1955. Summary of “Concerning some additional aids in studying sedimentary formations” by M.S. Shvetsov. *J. Sediment. Petrol.*, 25:229–234.
- Thierstein, H.R., Geitzenauer, K., Molfino, B., and Shackleton, N.J., 1977. Global synchronicity of late Quaternary coccolith datum levels: validation by oxygen isotopes. *Geology*, 5:400–404.
- Thomas, E., 1990. Late Cretaceous through Neogene deep-sea benthic foraminifers (Maud Rise, Weddell Sea, Antarctica). *In* Barker, P.F., Kennett, J.P., et al., *Proc. ODP, Sci. Results*, 113: College Station, TX (Ocean Drilling Program), 571–594.
- Thompson, P.R., Bé, A.W.H., Duplessy, J.-C., and Shackleton, N.J., 1979. Disappearance of pink-pigmented *Globigerinoides ruber* at 120,000 yr BP in the Indian and Pacific Oceans. *Nature*, 280:554–558.
- Thompson, R., and Oldfield, F., 1986. *Environmental Magnetism*: London (Allen and Unwin).
- Tjalsma, R.C., and Lohmann, G.P., 1983. *Paleocene–Eocene Bathyal and Abyssal Benthic Foraminifera from the Atlantic Ocean*. Spec. Publ.—Micropaleontology, 4.
- Toumarkine, M., and Luterbacher, H., 1985. Paleocene and Eocene planktic foraminifera. *In* Bolli, H.M., Saunders, J.B., and Perch-Nielsen, K. (Eds.), *Plankton Stratigraphy*: Cambridge (Cambridge Univ. Press), 87–154.
- Vacquier, V., 1985. The measurement of thermal conductivity of solids with a transient linear heat source on the plane surface of a poorly conducting body. *Earth Planet. Sci. Lett.*, 74:275–279.
- van Morkhoven, F.P.C.M., Berggren, W.A., and Edwards, A.S., 1986. *Cenozoic Cosmopolitan Deep-Water Benthic Foraminifera*. Bull. Cent. Rech. Explor.—Prod. Elf-Aquitaine, 11.
- Von Herzen, R.P., and Maxwell, A.E., 1959. The measurement of thermal conductivity of deep-sea sediments by a needle-probe method. *J. Geophys. Res.*, 64:1557–1563.

- Wang, P., Prell, W.L., Blum, P., et al., 2000. *Proc. ODP, Init. Repts.*, 184 [CD-ROM]. Available from: Ocean Drilling Program, Texas A&M University, College Station TX 77845-9547, USA.
- Wei, W., 1993. Calibration of upper Pliocene–lower Pleistocene nannofossil events with oxygen isotope stratigraphy. *Paleoceanography*, 8:85–99.
- Wentworth, C.K., 1922. A scale of grade and class terms of clastic sediments. *J. Geol.*, 30:377–392.
- Young, J.R., 1998. Neogene. In Bown, P.R. (Ed.), *Calcareous Nannofossil Biostratigraphy* (Vol. 8): Dordrecht (Kluwer Academic), 225–265.

Figure F1. Diagram showing nomenclature for principal components of whole-rock composition. Note that “-y” or “-ey” would be added after “sand,” “silt,” or “clay” when siliciclastics are a secondary component. Numbers indicate percentages.

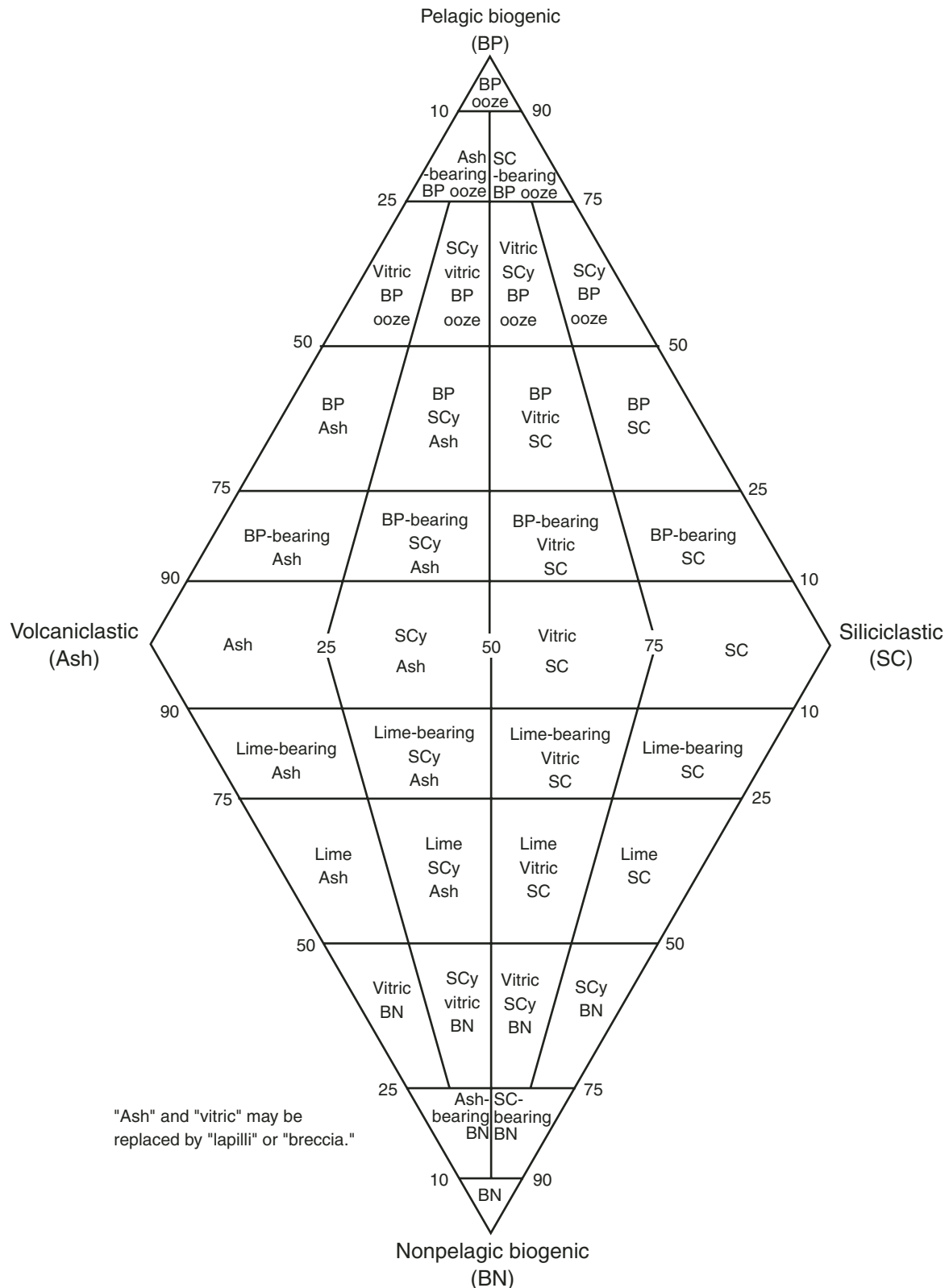


Figure F2. Grain size divisions for sedimentary rocks (adapted from Wentworth, 1922).

Millimeters (mm)	Micrometers (μm)	Phi (ϕ)	Wentworth size class		Rock type
4096		-12.0	Boulder		Conglomerate/ Breccia
256		-8.0	Cobble	Gravel	
64		-6.0	Pebble		
4		-2.0	Granule		
2.00		-1.0	Very coarse sand		
1.00		0.0	Coarse sand		
1/2	0.50	1.0	Medium sand	Sand	
1/4	0.25	2.0	Fine sand		
1/8	0.125	3.0	Very fine sand		
1/16	0.0625	4.0	Coarse silt	Silt	Siltstone
1/32	0.031	5.0	Medium silt		
1/64	0.0156	6.0	Fine silt		
1/128	0.0078	7.0	Very fine silt		
1/256	0.0039	8.0	Clay	Mud	Claystone
	0.00006	14.0			

Figure F3. Limestone classification (after Dunham, 1962, and Embry and Klovan, 1971).

Allocthonous limestones: Original components not organically bound during deposition					
Less than 10% grains >2 mm				More than 10% grains >2 mm	
Contains lime mud (<30 μm)			No lime mud		
Mud supported		Grain supported		Matrix supported	Grain (>2 mm) supported
>10% grains 0.03–2.0 mm	<10% grains 0.03–2.0 mm				
Mudstone	Wackestone	Packstone	Grainstone	Floatstone	Rudstone

Figure F4. Ternary diagram for siliciclastic textural classification. Numbers indicate percentages.

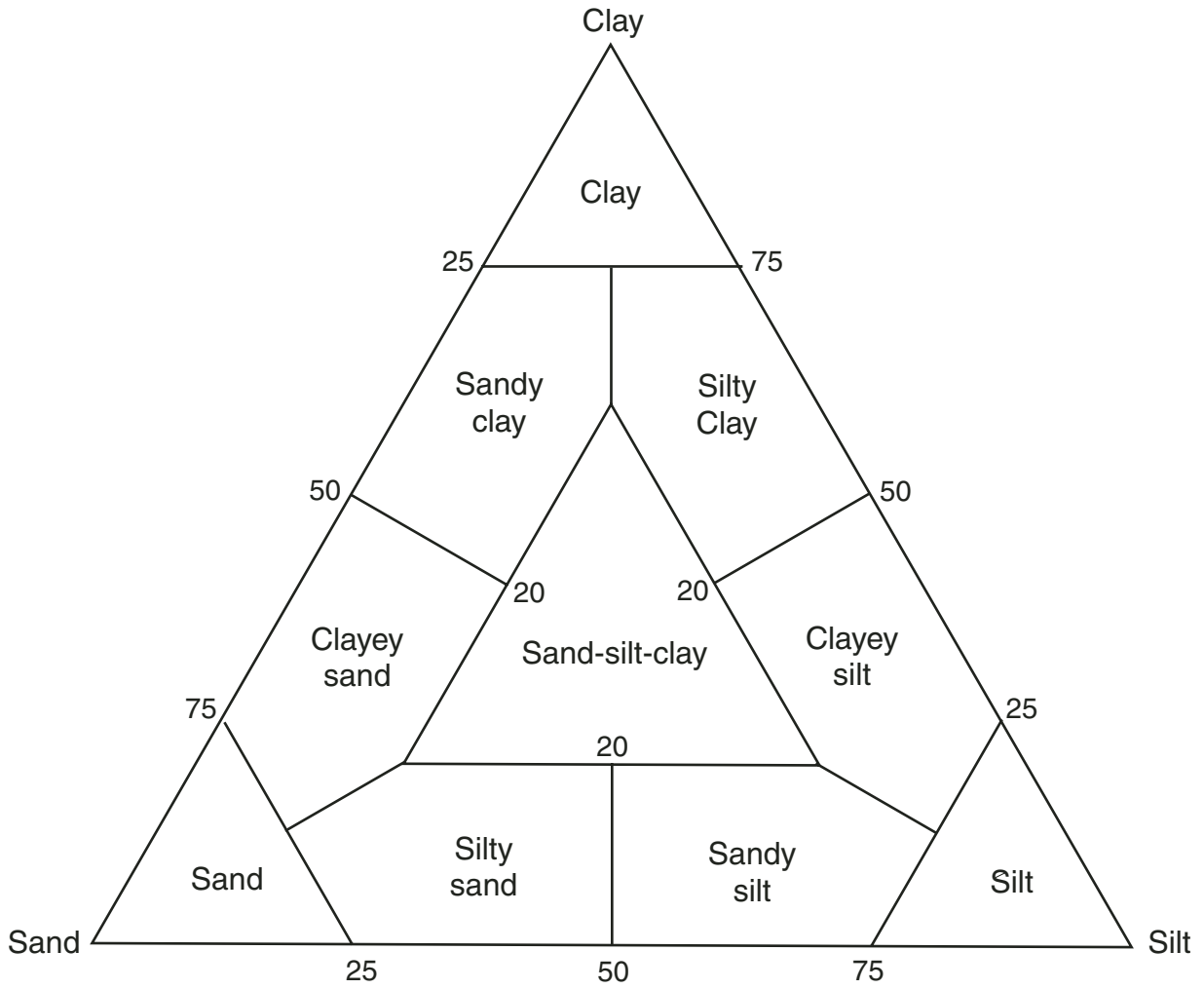


Figure F5. Example of an AppleCORE summary barrel sheet. Lith. = lithology, bioturb. = bioturbation, ichno. = ichnofossils, disturb. = core disturbance.

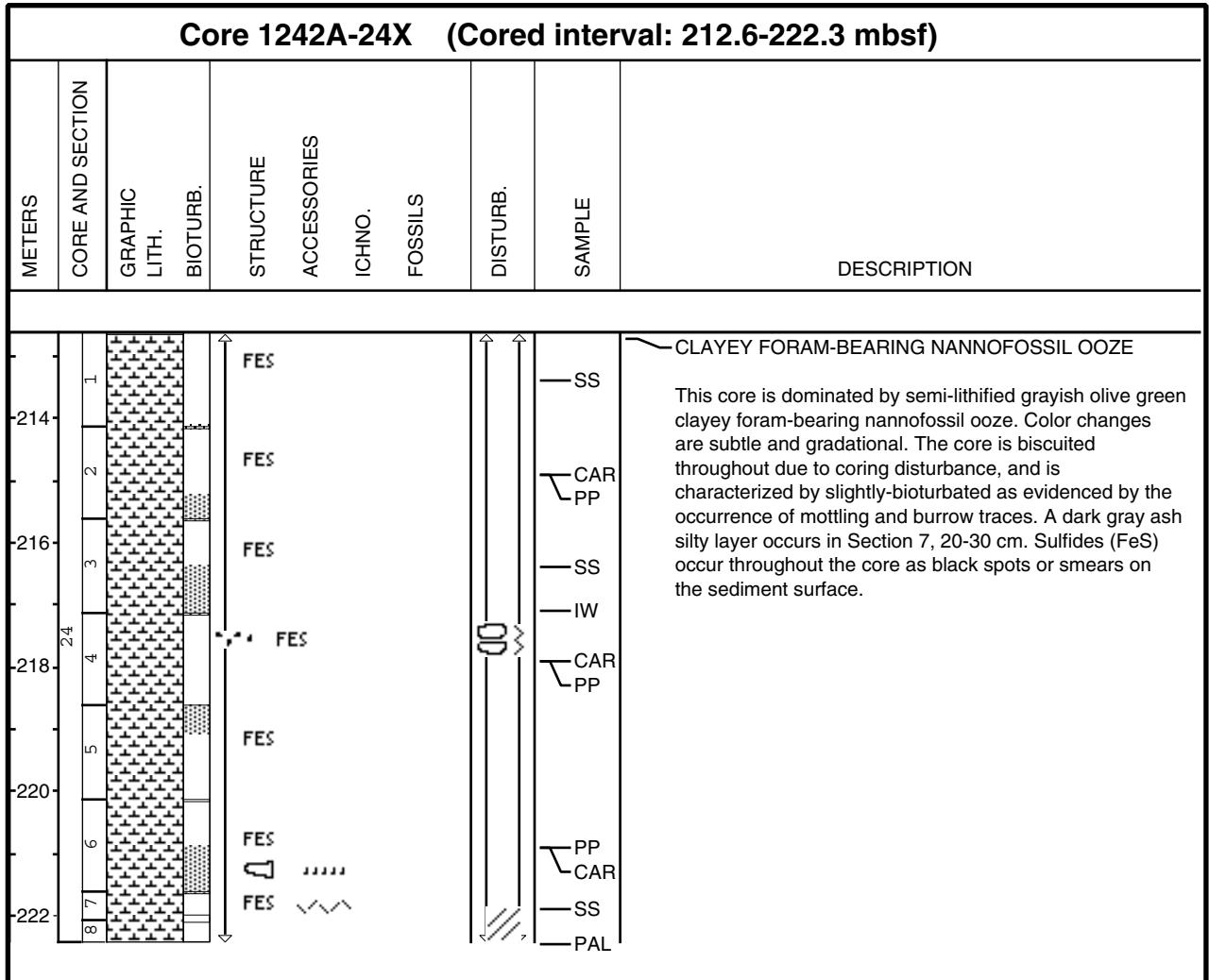
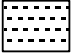

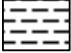



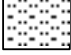

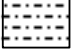
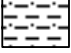
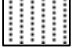



Figure F6. Key to symbols used for contacts, physical structures, lithologic accessories, ichnofossils, fossils, core disturbance, and bioturbation on the computer barrel sheet. (Continued on next page.)

Structure/Accessories	Contacts	Disturbance log
Sedimentary components	Sharp contact	Fractured
Silty lamina	Scoured contact	Disturbed
Sandy lamina	Bioturbated contact	Soupy
Isolated lamina	Uncertain contact	Flow-in
Planar lamina	Undulating contact	Gas expansion
Green clay	Faulted contact	Biscuit
Ash layer	Inclined contact	
Mud clast		
Patch	Bioturbation	Sample log
Nodule/Concretion	Abundant	SS Smear slide
Mottling	Common	CAR Carbonate
Upward fining	Moderate	PP Physical properties
Upward coarsening	Rare	IW Interstitial water
Fractured		PAL Micropaleontology
Biogenic components	Ichnofossils	XRD X-ray diffraction
Shell fragments	Burrow	THS Thin section
Coral fragments	<i>Zoophycos</i>	
Bivalve/mollusk		
Gastropod	Authigenics	
Spicule	FE _s Iron sulfide	
Serpulid	Py Pyrite	
Barnacle	GI Glaucinite	
Bryozoan		
Pteropod		
Vertebrate		
Benthic foraminifer		
Planktonic foraminifer		
Diatom		
Radiolarian		
		Abundance
		Rare
		Moderate
		Common
		Abundant
		Pervasive

Figure F6 (continued).

Graphic Lithologies
Siliciclastic sediment

	Clay/claystone		Volcanic or ash tuff
	Silty clay		Volcanic lapilli
	Clayey silt		Basalt
	Silt/Siltstone		Breccia
	Sand-silt-clay		
	Sandy clay		
	Clayey sand		
	Sand/sandstone		

Biogenic sediment


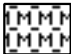
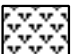

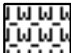
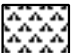
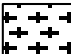
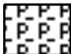

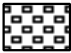
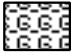

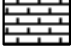

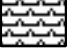
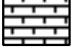

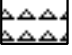
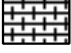
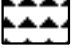
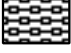

	Nannofossil ooze		Mudstone		Diatom ooze
	Foraminifer ooze		Wackestone		Radiolarian ooze
	Nannofossil-foraminifer/ Foraminifer-nannofossil ooze		Packstone		Diatom-radiolarian siliceous ooze
	Calcareous ooze		Grainstone		Diatomite
	Nannofossil chalk		Floatstone		Radiolarite
	Foraminiferal chalk		Rudstone		Porcellanite
	Foraminifer-nannofossil chalk				Chert
	Calcareous chalk				
	Limestone				

Figure F7. Comparison chart for volume percentage estimation (after Terry and Chilingar, 1955).

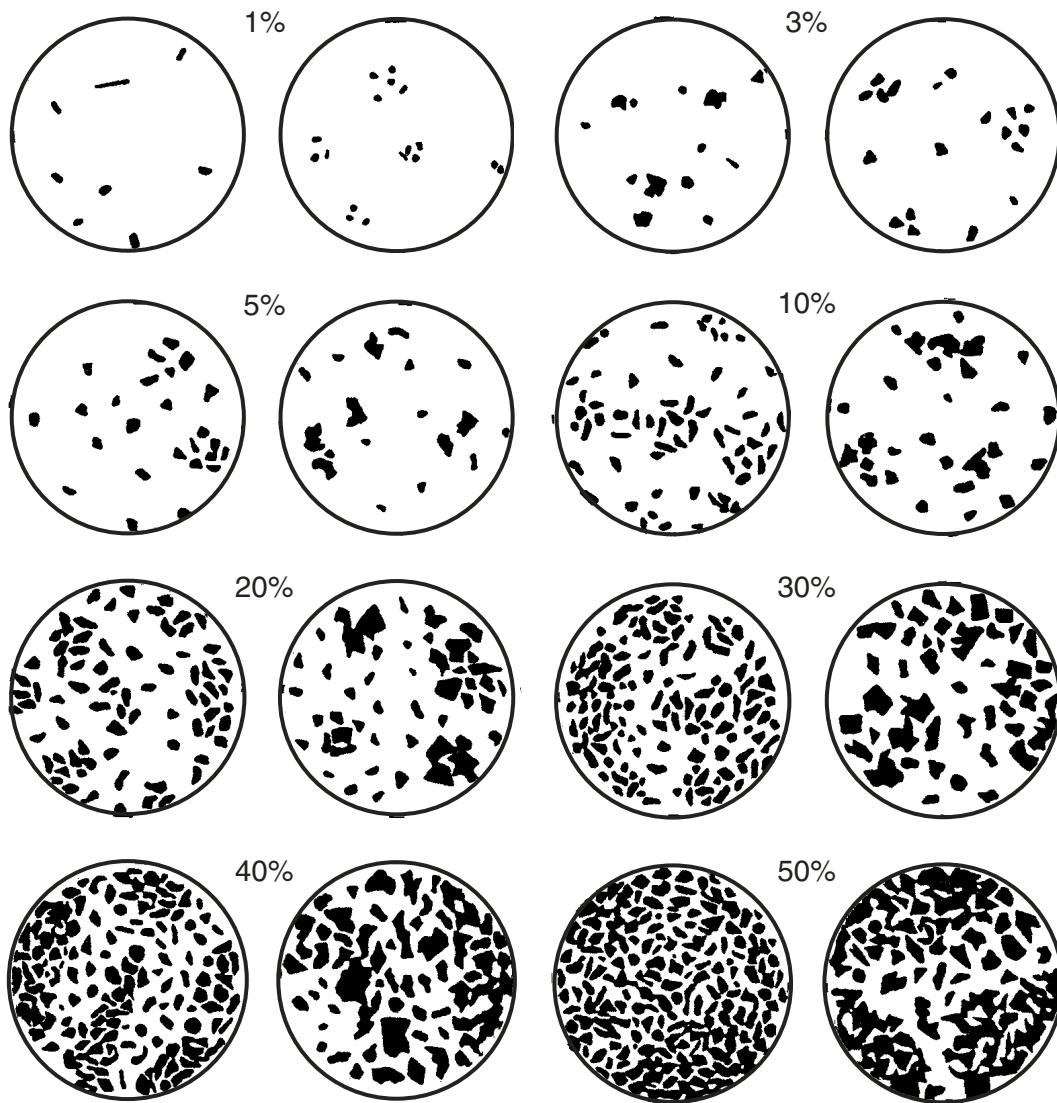


Figure F8. Response curves and full width at half maximum (FWHM) of the gamma ray attenuation (GRA) bulk density sensor, magnetic susceptibility loop (MSL), and natural gamma radiation (NGR) detector mounted on the whole-core multisensor track (MST).

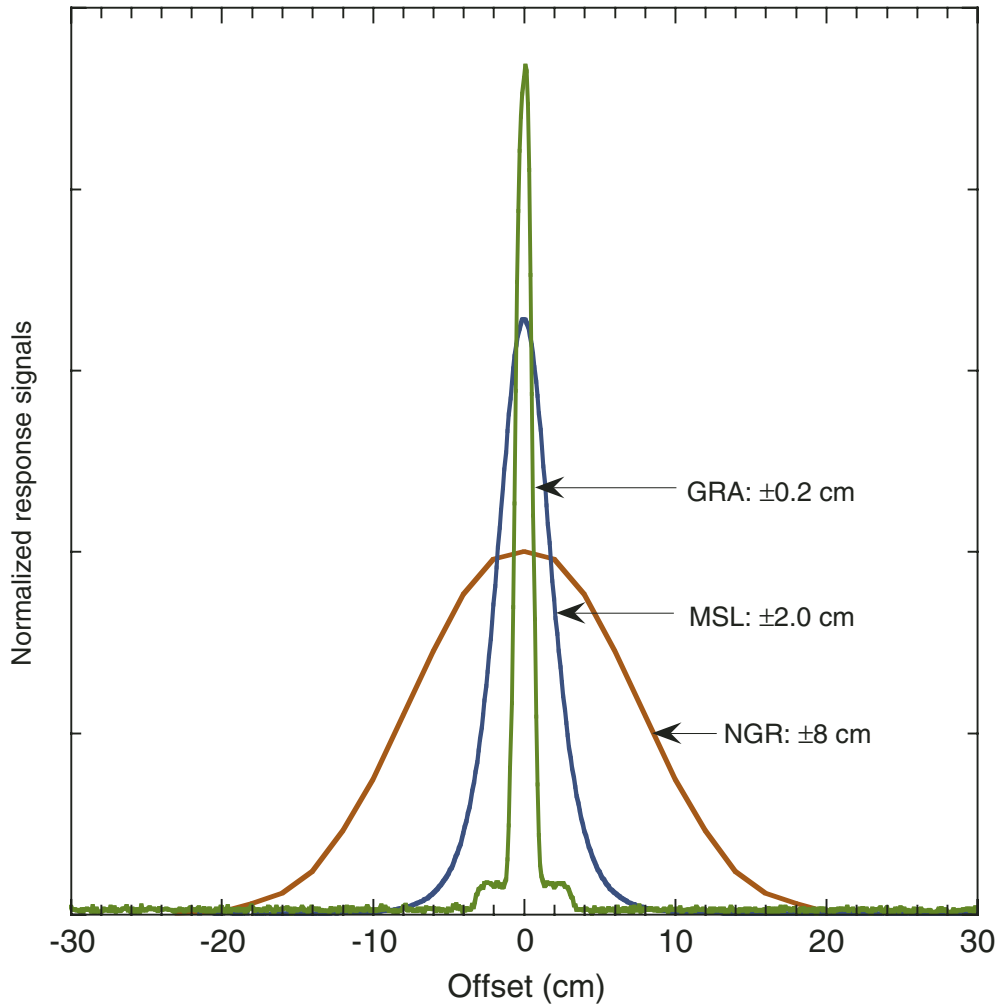


Figure F9. Comparison of response curves for two magnetic susceptibility sensor loops used during Leg 202. ODP multisensor track (ODP-MST; 8-cm loop); Oregon State University Fast Track magnetic susceptibility raw data (OSUS-MS; 10-cm loop); and OSUS-MS data corrected to match ODP-MST scale (integrated over peak area).

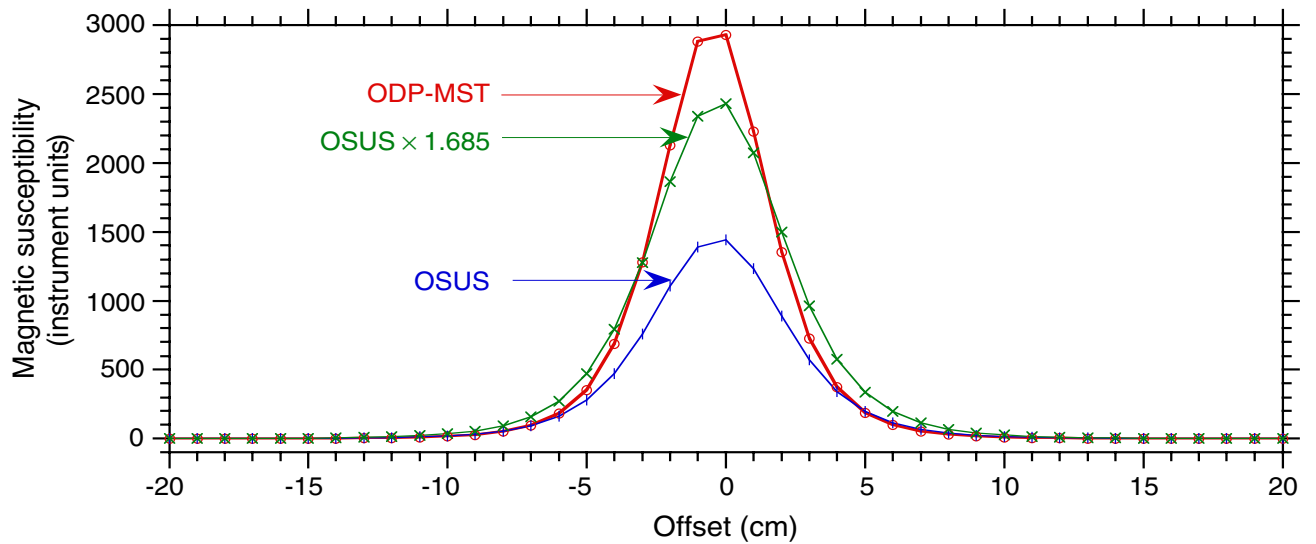


Figure F10. Overall spectral response of the Geotek DIS system. Reproduced with permission of Geotek, Ltd.

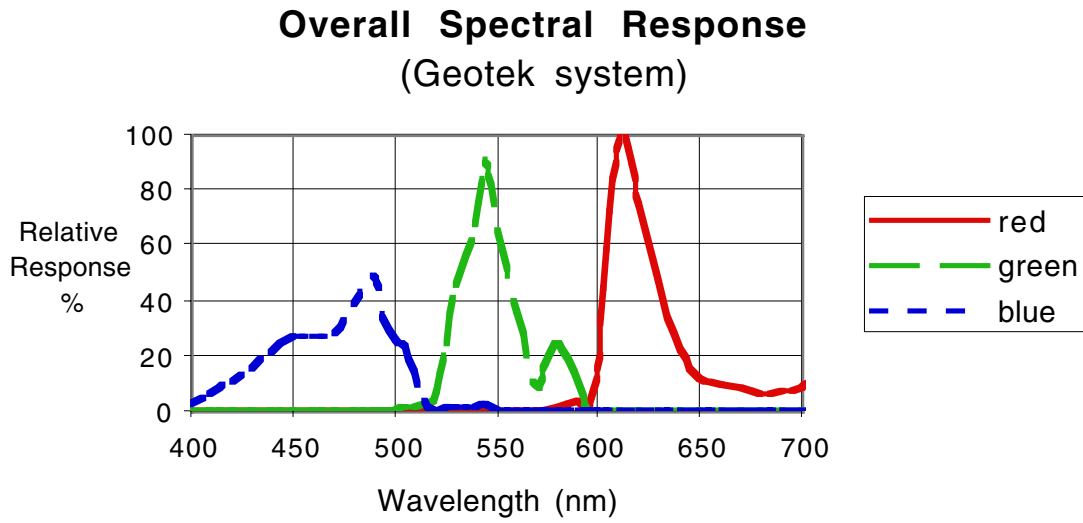


Figure F11. Data products produced from the Geotek DIS system during Leg 202.

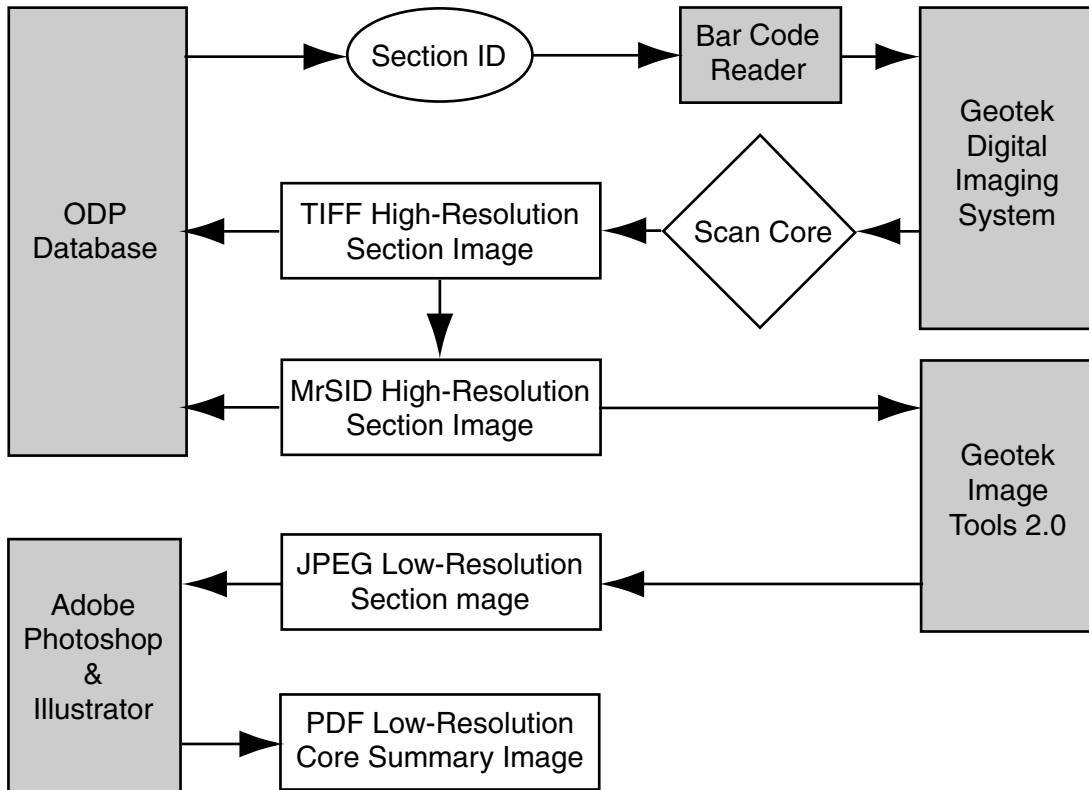


Figure F12. Correlation of geomagnetic polarity timescale (Berggren et al., 1995a) and biostratigraphic zonation used during Leg 202: calcareous nannofossils (Martini, 1971; Okada and Bukry, 1980), planktonic foraminifers (Berggren et al., 1995b), and diatoms (Barron, 1985a, 1985b; Baldauf and Iwai, 1995).

Ma	Age	Chron Cande & Kent, 1995	Calcareous nannofossils		Foraminifers Berggren et al. 1995	Diatom Barron, 1985a, b Baldauf & Iwai, 1995
			Okada & Bukry 1980	Martini 1971		
1	Pleistocene	C1	CN14	NN19	PT1b	<i>P. doliolus</i>
2			CN13	NN19	PT1a	<i>N. reinholdii</i> B
3	Pliocene	C2	CN12	NN18	PL6	<i>N. marina</i> A
4			CN12	NN17	PL5	
5	early	C2A	CN11	NN16	PL3	<i>N. jouseae</i>
6			CN11	NN15 - NN14	PL2	
7	late	C3	CN10	NN13	PL1b	<i>T. convexa</i> C
8			CN10	NN12	PL1a	
9	middle	C3A	CN9	NN11	M14	<i>N. miocenica</i> B
10			CN9	NN11	M13b	<i>N. porteri</i> B
11	late	C3B	CN8	NN10	M13a	<i>T. yabei</i> A
12			CN8	NN10	M13a	<i>A. moronensis</i>
13	middle	C4	CN7	NN9	M12	<i>C. coccinodiscus</i>
14			CN7	NN9	M11	<i>C. gigas</i>
15	early	C4A	CN6	NN8	M9b	<i>V. chlorama</i>
16			CN6	NN8	M9a	<i>C. lewisianus</i>
17	middle	C5	CN5	NN7	M7	<i>C. peplum</i> B
18			CN5	NN7	M6	<i>C. peplum</i> A
19	late	C5A	CN4	NN5	M5b	<i>C. nicobarica</i> B
20			CN4	NN5	M5a	<i>C. nicobarica</i> A
21	early	C5B	CN3	NN4	M4a	<i>T. pileus</i>
22			CN3	NN4	M3	<i>C. elegans</i>
23	middle	C5C	CN2	NN3	M2	<i>R. paleacea</i> C
24			CN2	NN3	M1	<i>R. paleacea</i> B
25	late	C5D	CN1	NN2	M1	<i>R. gelida</i> A
26			CN1	NN2	M1	<i>B. veniamini</i> B
27	early	C5E	CP19	NP25	P22	<i>R. vigilans</i> B
28			CP19	NP25	P21a	
29	middle	C6	CP19	NP25	P21b	<i>R. vigilans</i> A
30			CP19	NP25	P20	
31	late	6A	CP18 + CP17	NP23	P19	<i>C. excavatus</i>
32			CP18 + CP17	NP23	P18	
33	early	6AA	CP16	NP22	P17	unzoned
34			CP16	NP22	P16	
35	middle	6B	CP15	NP20 + NP19	P15	unzoned
36			CP15	NP20 + NP19	P14	
37	late	6C	CP15	NP18	P13	unzoned
38			CP15	NP18	P12	
39	early	6AA	CP14	NP17	P11	unzoned
40			CP14	NP17	P10	
41	middle	6B	CP14	NP16	P10	unzoned
42			CP14	NP16	P10	
43	late	6C	CP13	NP15	P10	unzoned
44			CP13	NP15	P10	
45	early	6B	CP12	NP14	P10	unzoned
46			CP12	NP14	P10	
47	middle	6C	CP12	NP14	P10	unzoned
48			CP12	NP14	P10	

Figure F13. Schematic illustration of the configurations of tool strings run during Leg 202 (see Table T10, p. 76, for explanations of the acronyms). Triple combo = triple combination tool.

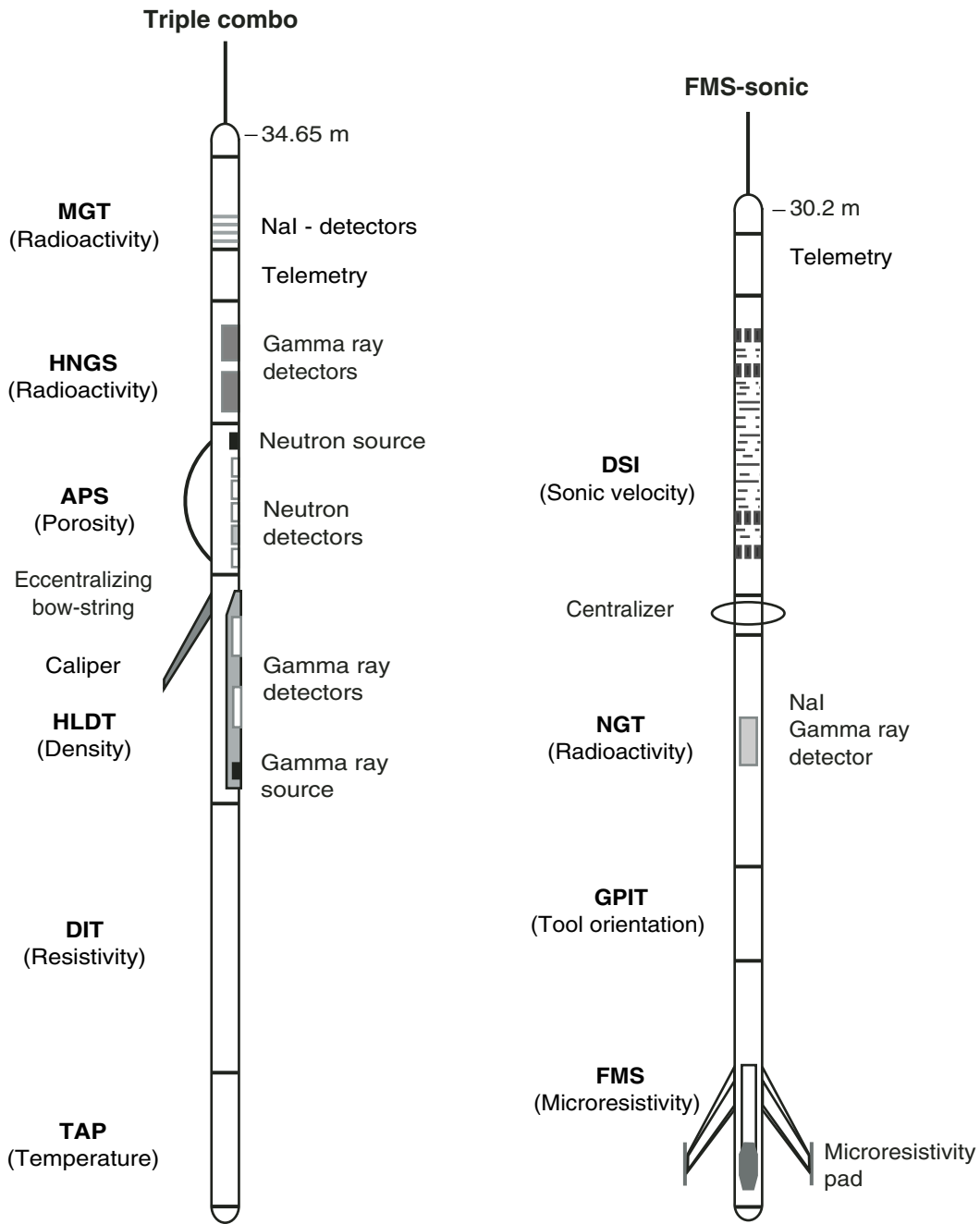


Table T1. Summary of depth scales used in constructing the composite sections.

Depth scale	Acronym	Definition
Meters below sea floor*	mbsf	The mbsf scale is defined by the wireline length when a core is drilled.
Meters composite depth*	mcd	The mcd scale is derived from correlation of physical properties measurements between holes and represents the depth in the composite sedimentary sequence.
Corrected meters composite depth†	cmcd	The cmcd scale is constructed by dividing the mcd scale by the amount that the mcd scale grew relative to the mbsf scale (the growth factor).
Meters logging depth‡	mld	The mld scale is determined by estimating depths based on the rate at which the logging tool is raised through the hole and the time at which it senses the sediment/water interface.
Estimated logging depth‡	eld	The eld scale is constructed by correlation of whole-core physical properties data with logging data.

Notes: * = for a detailed explanation, see [“Composite Depth Scale,”](#) p. 4, in “Composite Section.” † = For a detailed explanation, see [“Corrected Composite Depth,”](#) p. 6, in “Composite Section.” ‡ = For a detailed explanation, see [“Core-Log Integration,”](#) p. 6, in “Composite Section.”

Table T2. Sediment nomenclature, Leg 202.

Major lithologic names are defined as combinations of the following four major modifiers (grain types), using Figure F1, p. 51:

Siliciclastics:

Crystalline grains and detrital aggregates

Quartz, feldspars, clay minerals, heavy minerals, rock fragments, opaque minerals, and glauconite

Modifier definition: Siliciclastic grains are classified in their size such as sand (2 mm–63 μm), silt (63 μm–4 μm), and clay (<4 μm) according to Wentworth (1922). Siliciclastic modifiers are defined using Figure F2, p. 52.

Volcaniclastics:

Amorphous grains of volcanic origin and their altered products

Glass shards, pumice, scoria, and palagonite

Modifier definition: Volcaniclastic grains are classified in three grain-size classes as ash (<2 mm), lapilli (2–64 mm), and breccia (>64 mm). Volcaniclastic modifiers are defined using the most abundant size class.

Biogenics:

Remains of organisms with siliceous and calcareous hard parts. Microcrystalline carbonate and aggregates of unknown origin are also included.

Group 1 (siliceous) diatom, radiolarians, silicoflagellates, and sponge spicules

Group 1 (calcareous pelagic) foraminifers, and nannofossils

Group 2 (calcareous unknown) micrite

Group 2 (calcareous nonpelagic) some benthic foraminifers, bioclasts, and peloids

Modifier definition:

1. Normalize each biogenic component to 100%.

2. If the total of Group 1 grains is >50%, define a pelagic modifier with the >25% components of Group 1 in order of increasing abundance. If two or more components have equal amounts, then use a hyphen between the names rather than a space. Components of 10%–25% in Group 1 are treated as biogenic minor modifiers, while those of 10%–50% in Group 2 are treated as diagenetic minor modifiers.

3. If the total of Group 2 grains is >50%, define a nonpelagic modifier using limestone classification scheme (Fig. F3, p. 53, after Dunham [1962]). Components of 10%–50% in Group 1 are treated as biogenic minor modifiers. If two or more components in biogenic minor modifier have equal amounts, then use a hyphen between the names rather than a space.

Other minor modifiers (diagenetic):

Grains formed during postdepositional process.

Pyrite, dolomite, and zeolites. Microcrystalline carbonate and aggregates of unknown origin are included.

Modifier definition: Diagenetic grains are treated as a diagenetic minor modifier.

Diagenetic grains are treated as a diagenetic minor modifier.

Treatment of minor modifiers:

Biogenic minor modifiers and diagenetic minor modifiers <10% in bulk sediment are ignored.

Remaining biogenic minor modifiers are placed in order of increasing abundance just before pelagic modifier or nonpelagic modifier using X-, Y-, Z-bearing style (see Fig. F4, p. 54, for example). If two or more components in biogenic minor modifiers have equal amounts, then use a hyphen between the names rather than a space.

Diagenetic minor modifiers are placed in order of decreasing abundance after major lithologic name using Z, Y, and X style. If two or more components with diagenetic minor modifiers have equal amounts, then use a hyphen between the names rather than a space

If “-bearing” occurs twice in the lithologic name, the first one is removed, such as X Y-bearing Z; X-bearing Y-bearing Z style is never used.

Table T3. Magnetic susceptibility signal response for ODP-MST and OSUS instruments.

Distance from loop (cm)	ODP MST (instrument units)	OSUS (instrument units)	OSU x 1.686
-20	0.4	0.0	0.0
-19	0.2	0.0	0.0
-18	0.8	1.0	1.7
-17	0.6	1.0	1.7
-16	1.4	1.7	2.8
-15	1.6	2.0	3.4
-14	2.6	3.3	5.6
-13	4.0	5.7	9.6
-12	6.6	8.0	13.5
-11	10.6	13.3	22.5
-10	17.2	20.7	34.8
-9	29.8	33.3	56.2
-8	53.0	55.7	93.8
-7	96.8	94.3	159.0
-6	183.0	161.7	272.5
-5	354.6	279.3	470.8
-4	689.0	471.7	795.0
-3	1,282.6	758.3	1,278.2
-2	2,130.8	1,106.3	1,864.7
-1	2,880.6	1,388.3	2,340.1
0	2,930.8	1,441.3	2,429.4
1	2,229.4	1,230.3	2,073.7
2	1,356.0	888.7	1,497.9
3	727.8	570.7	961.9
4	373.4	342.3	577.0
5	191.6	199.0	335.4
6	101.2	116.0	195.5
7	55.2	68.0	114.6
8	31.2	40.7	68.5
9	18.2	25.0	42.1
10	11.4	15.7	26.4
11	7.0	9.7	16.3
12	4.6	5.7	9.6
13	3.0	4.3	7.3
14	1.8	2.7	4.5
15	1.4	2.0	3.4
16	1.2	1.0	1.7
17	1.0	1.0	1.7
18	0.4	0.3	0.6
19	0.4	0.0	0.0
20	0.6	0.3	0.6
Integrated area:	15,794.0	9,370.3	15,794.0

Notes: OSUS = Oregon State University Fast Track system, ODP = Ocean Drilling Program, MST = multisensor track, OSU = Oregon State University.

Table T4. Calcareous nannofossil datums, Leg 202.

Event	Age (Ma)	Age references	Zone/subzone base	
			Martini (1971)	Okada and Bukry (1980)
FCO acme <i>Emiliana huxleyi</i>	0.085–0.073	1	NN21b	
FO <i>Emiliana huxleyi</i>	0.26	1	NN21a	CN15
LO <i>Pseudoemiliana lacunosa</i>	0.46	1	NN20	CN14b
LO <i>Reticulofenestra asanoi</i>	0.88	2		
RE medium <i>Gephyrocapsa</i> spp.	1.02	3		CN14a?
FO <i>Reticulofenestra asanoi</i>	1.08	2		
LO large <i>Gephyrocapsa</i> spp.	1.24	2		
FO large <i>Gephyrocapsa</i> spp.	1.45	3		
LO <i>Calcidiscus macintyreii</i>	1.59	3		
FO medium <i>Gephyrocapsa</i>	1.67	3		
LO <i>Discoaster brouweri</i>	1.96	4	NN19	CN13a
LO <i>Discoaster pentaradiatus</i>	2.44	4	NN18	CN12d
LO <i>Discoaster surculus</i>	2.61	4	NN17	CN12c
LO <i>Discoaster tamalis</i>	2.76	4		CN12b
LO <i>Sphenolithus</i> spp.	3.65	4		
LO <i>Reticulofenestra pseudoumbilicus</i>	3.8	4	NN16	CN12a
FO <i>Ceratolithus rugosus</i>	5.04	4		
FO <i>Ceratolithus acutus</i>	5.34	4		
LO <i>Triquetrorhabdulus rugosus</i>	5.35	4		
LO <i>Discoaster quinqueringus</i>	5.56	4	NN12	CN10a
LO <i>Amaurolithus amplificus</i>	5.88	4		
FO <i>Amaurolithus amplificus</i>	6.5	4		
RE absence interval <i>Reticulofenestra pseudoumbilicus</i>	6.8	4		
FO <i>Amaurolithus primus</i>	7.24	4		CN9b
FO <i>Discoaster berggrenii</i>	8.35	4	NN11?	CN9a
FO <i>Discoaster loeblichii</i>	8.43	4		
LCO absence interval <i>Reticulofenestra pseudoumbilicus</i>	8.85	4		
FO <i>Minylitha convallis</i>	9.37	4		
LO <i>Discoaster hamatus</i>	9.4	4	NN10	CN8a
FO <i>Discoaster neohamatus</i>	9.56	4	NN9	CN7
FO <i>Discoaster hamatus</i>	10.38	4		
LO <i>Coccolithus miopelagicus</i>	10.48	4		
FO <i>Catinaster coalitus</i>	10.73	4	NN8	CN6
LCO <i>Discoaster kugleri</i>	11.36	4		
FCO <i>Discoaster kugleri</i>	11.74	4		
FO <i>Calcidiscus macintyreii</i>	12.14	4		
FO <i>Discoaster kugleri</i>	12.2	4	NN7	CN5b
LO <i>Coronocyclus nitescens</i>	12.43	4		
FO <i>Triquetrorhabdulus rugosus</i>	12.62	4		
LO <i>Calcidiscus premacintyreii</i>	12.65	4		
FO <i>Discoaster signus</i>	13.08	4		
LO <i>Cyclicargolithus floridanus</i>	13.19	4		
LO <i>Sphenolithus heteromorphus</i>	13.57	4	NN6	CN5a
LO <i>Helicosphaera ampliaptera</i>	15.87	4	NN5	CN4
FO <i>Discoaster signus</i>	16.2	4		
LCO acme <i>Discoaster deflandrei</i>	16.22	4		
FO <i>Calcidiscus premacintyreii</i>	17.4	5		
FO <i>Sphenolithus heteromorphus</i>	18.2	5		CN3
LO <i>Sphenolithus belemnus</i>	18.3	5	NN4	
FO <i>Sphenolithus belemnus</i>	19.2	5	NN3	
FO <i>Discoaster druggii</i>	23.2	5	NN2	CN1c
LO <i>Reticulofenestra bisecta</i>	23.90	5	NP25	CP19
LO <i>Zygrhablithus bijugatus</i>	24.50	5	NP25	CP19
LO <i>Sphenolithus ciperoensis</i>	24.75	5	NP25	CP19
LO <i>Sphenolithus distentus</i>	27.5	5	NP25/24	CP19a/19b
LO <i>Sphenolithus pseudoradians</i>	29.1	5	NP24	CP19
FO <i>Sphenolithus ciperoensis</i>	29.9	5	NP24/23	CP19/18

Notes: FO = first occurrence, FCO = first common occurrence, LO = last occurrence, LCO = last common occurrence. RE = reappearance. Zonal codes are those of Martini (1971) and Okada and Bukry (1980). Age references: 1 = Thierstein et al. (1977); 2 = Wei (1993); 3 = Raffi et al. (1993); 4 = Raffi and Flores (1995); 5 = Berggren et al., 1995b.

Table T5. Planktonic foraminifer datums, Leg 202. (See table notes. Continued on next two pages.)

Event	Zone (base)	Age (Ma)	Source*
LO <i>Globorotalia flexuosa</i>		0.068	Berggren et al., 1995a
LO <i>Globigerinoides ruber</i>		0.12	Thompson, P.R., 1979
LO <i>Globoquadrina pseudofoliata</i>		0.22	Berggren et al., 1995a
FO <i>Bolliella calida</i>		0.22	Berggren et al., 1995a
FO <i>Globigerinoides ruber</i>		0.40	Li, B., 1997
FO <i>Globorotalia flexuosa</i>		0.401	Berggren et al., 1995a
FO <i>Globorotalia hirsuta</i>		0.45	Berggren et al., 1995a
LO <i>Globorotalia tosaensis</i>	Pt1b	0.65	Berggren et al., 1995a
LO <i>Globorotalia crassaformis hessi</i>		0.75	Berggren et al., 1995a
FO <i>Globorotalia truncatulinoides excelsa</i>		1.00	Berggren et al., 1995a
LO <i>Globigerinoides obliquus</i>		1.30	C&P97, P&C97, CSR95
LO <i>Pulleniatina finalis</i>		1.40	Berggren et al., 1995a
LO <i>Neogloboquadrina acostaensis</i>		1.58	C&P97, P&C97, CSR95
LO <i>Globoturborotalita apertura</i>		1.64	Berggren et al., 1995a
LO <i>Globigerinoides fistulosus</i>	Pt1a	1.77	Berggren et al., 1995a
LO <i>Globigerinoides extremus</i>		1.77	Berggren et al., 1995a
FO <i>Globorotalia (Truncorotalia) truncatulinoides</i>		2.00	Berggren et al., 1995a
FO <i>Pulleniatina finalis</i>		2.04	C&P97, P&C97, CSR95
FO <i>Globorotalia inflata</i>		2.09	Berggren et al., 1995a
LO <i>Globorotalia (Menardella) exilis</i>		2.15	Berggren et al., 1995a
Reappearance of <i>Pulleniatina</i> (Atlantic)		2.26	C&P97, P&C97, CSR95
LO <i>Globoturborotalia woodi</i>		2.33	C&P97, P&C97, CSR95
LO <i>Globorotalia (Menardella) miocenica</i> (Atlantic)	PI6	2.30	Berggren et al., 1995a
LO <i>Globorotalia (Menardella) pseudomiocenica</i> (Pacific)	PI6	2.30	Berggren et al., 1995a
LO <i>Globorotalia puncticulata</i>		2.41	Berggren et al., 1995a
LO <i>Neogloboquadrina atlantica</i>		2.41	Berggren et al., 1995a
LO <i>Globorotalia (Menardella) limbata</i>		2.38	C&P97, P&C97, CSR95
LO <i>Globorotalia (Menardella) pertenuis</i>		2.60	Berggren et al., 1995a
LO <i>Globoturborotalia decoraperta</i>		2.75	C&P97, P&C97, CSR95
LO <i>Globorotalia (Menardella) multicamerata</i>		3.09	Berggren et al., 1995a
LO <i>Dentoglobigerina altispira</i>	PI5	3.09	Berggren et al., 1995a
LO <i>Sphaeroidinellopsis seminulina</i>	PI4	3.12	Berggren et al., 1995a
LO <i>Globorotalia (Hirsutella) cibaoensis</i>		3.22	C&P97, P&C97, CSR95
LO <i>Globoquadrina baroemoensis</i>		3.22	C&P97, P&C97, CSR95
FO <i>Sphaeroidinella dehiscens</i> s.s.		3.25	Berggren et al., 1995a
FO <i>Globigerinoides fistulosus</i>		3.33	Berggren et al., 1995a
FO <i>Globorotalia (Truncorotalia) tosaensis</i>		3.35	Berggren et al., 1995a
LO <i>Pulleniatina</i> (Atlantic)		3.45	Berggren et al., 1995a
FO <i>Globorotalia (Menardella) pertenuis</i>		3.45	Berggren et al., 1995a
LO <i>Globorotalia plesiotumida</i>		3.77	C&P97, P&C97, CSR95
FO <i>Globorotalia (Menardella) miocenica</i>		3.55	Berggren et al., 1995a
LO <i>Globorotalia (Hirsutella) margaritae</i>	PI3	3.58	Berggren et al., 1995a
LO <i>Pulleniatina primalis</i>		3.65	Berggren et al., 1995a
<i>Pulleniatina</i> (S to D coiling change)		3.95	Berggren et al., 1995a
LO common <i>Globorotalia margaritae</i>		3.96	Berggren et al., 1995a
LO <i>Globoturborotalita nepenthes</i>	PI2	4.18	Berggren et al., 1995a
LO <i>Pulleniatina spectabilis</i>		4.20	Berggren et al., 1995a
FO <i>Globorotalia (Menardella) exilis</i>		4.45	C&P97, P&C97, CSR95
FO <i>Globorotalia puncticulata</i>		4.50	Berggren et al., 1995a
FO <i>Globorotalia (Truncorotalia) crassaformis</i> s.l.		4.5	Berggren et al., 1995a
LO <i>Sphaeroidinellopsis kochi</i>		4.53	C&P97, P&C97, CSR95
LO <i>Globorotalia cibaoensis</i>	PI1b	4.6	Berggren et al., 1995a
LO <i>Globigerinoides seiglei</i>		4.70	Berggren et al., 1995a
FO common <i>Globorotalia margaritae</i>		5.07	Berggren et al., 1995a
FO <i>Sphaeroidinella dehiscens</i> s.l.		5.54	C&P97, P&C97, CSR95
FO <i>Globorotalia pliozea</i>		5.60	Berggren et al., 1995b
FO <i>Globorotalia sphericomiozea</i>		5.60	Berggren et al., 1995b
FO <i>Globorotalia tumida</i>	PI1a	5.82	C&P97, P&C97, CSR95
LO <i>Globoquadrina dehiscens</i>		5.49	Shackleton et al., 1995
FO <i>Turborotalia humilis</i>		5.84	C&P97, P&C97, CSR95
LO <i>Globorotalia linguaensis</i>	M14	6.0	Berggren et al., 1995b
FO <i>Globorotalia (Hirsutella) margaritae</i>		6.09	C&P97, P&C97, CSR95
FO <i>Pulleniatina primalis</i>		6.4	Berggren et al., 1995b
FO <i>Globigerinoides conglobatus</i>		6.20	C&P97, P&C97, CSR95
<i>Neogloboquadrina acostaensis</i> (D to S coiling change)		6.6	Berggren et al., 1995b
FO <i>Globorotalia conomiozea</i>		7.12	Berggren et al., 1995b
FO <i>Globorotalia (Hirsutella) cibaoensis</i>		9.44	C&P97, P&C97, CSR95
FO <i>Candeina nitida</i>		8.44	C&P97, P&C97, CSR95

Table T5 (continued).

Event	Zone (base)	Age (Ma)	Source*
FO <i>Globorotalia (Hirsutella) juanai</i>		9.76	C&P97, P&C97, CSR95
FO <i>Globigerinoides extremus</i>		8.58	C&P97, P&C97, CSR95
FO <i>Globorotalia plesiotumida</i>		8.58	C&P97, P&C97, CSR95
FO <i>Neogloboquadrina humerosa</i>		8.5	Berggren et al., 1995b
LO <i>Neogloboquadrina nympa</i>		10.1	Berggren et al., 1995b
FO <i>Neogloboquadrina acostansis</i>	M13	9.82	C&P97, P&C97, CSR95
LO <i>Paragloborotalia mayeri</i>	M12	10.49	C&P97, P&C97, CSR95
FO <i>Globorotalia (Menardella) limbata</i>		10.57	C&P97, P&C97, CSR95
FO <i>Globoturborotalita apertura</i>		11.19	C&P97, P&C97, CSR95
FO <i>Globoturborotalita decoraperta</i>		11.46	C&P97, P&C97, CSR95
FO <i>Sphaeroidinellopsis subdehiscens</i>		11.74	Berggren et al., 1995b
FO <i>Globoturborotalita nepenthes</i>	M11	11.19	C&P97, P&C97, CSR95
LO <i>Globorotalia panda</i>		11.8	Berggren et al., 1995b
LO <i>Globorotalia praescitula</i>		11.9	Berggren et al., 1995b
LO <i>Fohsella fohsi</i> s.l. (incl. <i>fohsi lobata</i> and <i>fohsi robusta</i>)	M10	11.68	C&P97, P&C97, CSR95
FO <i>Globorotalia linguaensis</i>		12.85	C&P97, P&C97, CSR95
FO <i>Fohsella fohsi robusta</i>	M9b	13.18	C&P97, P&C97, CSR95
FO <i>Fohsella fohsi</i> s.l.	M9a	13.42	C&P97, P&C97, CSR95
FO <i>Fohsella praefohsi</i>	M8	12.7	Berggren et al., 1995b
FO <i>Neogloboquadrina nympa</i>		13.4	Berggren et al., 1995b
LO <i>Clavatorella bermudezi</i>		14.2	C&P97, P&C97, CSR95
LO <i>Globorotalia archeomenardii</i>		14.2	C&P97, P&C97, CSR95
LO <i>Fohsella peripheroronda</i>		14.6	Berggren et al., 1995b
FO <i>Fohsella peripheroacuta</i>	M7	14.8	Berggren et al., 1995b
LO <i>Praeorbulina sicana</i>		14.8	Berggren et al., 1995b
LO <i>Praeorbulina glomerosa</i>		14.8	Berggren et al., 1995b
FO <i>Globorotalia (Menardella) praemenardii</i>		14.9	C&P97, P&C97, CSR95
LO <i>Globigerinatella insueta</i>		15.0	C&P97, P&C97, CSR95
FO <i>Orbulina</i> spp.	M6	15.1	Berggren et al., 1995b
FO <i>Globorotalia (Menardella) archeomenardii</i>		15.5	C&P97, P&C97, CSR95
FO <i>Clavatorella bermudezi</i>		15.8	C&P97, P&C97, CSR95
LO <i>Globorotalia miozea</i>		15.9	Berggren et al., 1995b
FO <i>Praeorbulina circularis</i>		16.0	Berggren et al., 1995b
FO <i>Praeorbulina glomerosa</i>	M5b	16.10	Berggren et al., 1995b
FO <i>Globigerinoides diminutus</i>		16.1	Berggren et al., 1995b
FO <i>Praeorbulina curva</i>		16.3	Berggren et al., 1995b
FO <i>Praeorbulina sicana</i>	M5b	16.4	Berggren et al., 1995b
LO <i>Globorotalia incognita</i>		16.4	Berggren et al., 1995b
FO <i>Globorotalia miozea</i>		16.7	Berggren et al., 1995b
FO <i>Globorotalia birnageae</i>	M4b	16.7	Berggren et al., 1995b
LO <i>Catapsydrax dissimilis</i>	M4	17.3	Berggren et al., 1995b
LO <i>Globorotalia zealandica</i>		17.3	Berggren et al., 1995b
LO <i>Globorotalia semivera</i>		17.3	Berggren et al., 1995b
FO <i>Globorotalia praescitula</i>		18.5	Berggren et al., 1995b
FO <i>Globigerinatella insueta</i>	M3	18.8	Berggren et al., 1995b
LO <i>Globoquadrina binaiensis</i>		19.1	C&P97, P&C97, CSR95
FO <i>Globigerinoides altiapertura</i>		20.5	Berggren et al., 1995b
LO <i>Tenuitella munda</i>		21.4	Berggren et al., 1995b
LO <i>Paragloborotalia kugleri</i>	M2	21.5	Berggren et al., 1995b
FO <i>Globorotalia incognita</i>		21.6	Berggren et al., 1995b
LO <i>Globoturborotalita angulisuturalis</i>		21.6	Berggren et al., 1995b
LO <i>Paragloborotalia pseudokugleri</i>		21.6	Berggren et al., 1995b
FO <i>Globoquadrina binaiensis</i>		22.1	Berggren et al., 1995b
FO <i>Globoquadrina dehiscens</i>	M1b	23.2	Berggren et al., 1995b
LO <i>Globigerina ciperoensis</i>		23.3	C&P97, P&C97, CSR95
FO <i>Globigerinoides trilobus</i> s.l.		23.4	C&P97, P&C97, CSR95
FO <i>Paragloborotalia kugleri</i>	M1	23.8	Berggren et al., 1995b
LO <i>Globigerina euapertura</i>		23.8	Berggren et al., 1995b
FO <i>Globigerinoides primordius</i> (common)		24.3	Berggren et al., 1995b
LO <i>Tenuitella gemma</i>		24.3	Berggren et al., 1995b
FO <i>Paragloborotalia pseudokugleri</i>		25.9	Berggren et al., 1995b
FO <i>Globigerinoides primordius</i>		26.7	Berggren et al., 1995b
LO <i>Paragloborotalia opima</i>	P22	27.1	Berggren et al., 1995b
LO <i>Globigerina labiacrassata</i>		27.1	Berggren et al., 1995b
LO <i>Chiloguembelina cubensis</i> (common)	P21b	28.5	Berggren et al., 1995b
FO <i>Globoturborotalita angulisuturalis</i>	P21a	29.4	Berggren et al., 1995b
LO <i>Subbotina angiporoides</i>		30.0	Berggren et al., 1995b
LO <i>Turborotalia ampliapertura</i>	P20	30.3	Berggren et al., 1995b
FO <i>Paragloborotalia opima</i>		30.6	Berggren et al., 1995b

Table T5 (continued).

Event	Zone (base)	Age (Ma)	Source*
LO <i>Pseudohastigerina</i> spp.	P19	32.0	Berggren et al., 1995b
FO <i>Cassigerinella chipolensis</i>		33.65	Berggren et al., 1995b
LO <i>Hantkenina</i> spp.		33.7	Berggren et al., 1995b
LO <i>Turborotalia cerroazulensis</i>	P18	33.8	Berggren et al., 1995b
LO <i>Cribohantkenina inflata</i>	P17	34.0	Berggren et al., 1995b
LO <i>Clavigerinella oceanica</i>		34.0	C&P97, P&C97, CSR95
LO <i>Globigerapsis index</i>		34.3	Berggren et al., 1995b
FO <i>Turborotalia cunialensis</i>	P16	35.2	Berggren et al., 1995b
LO <i>Turborotalia pomeroli</i>		35.3	Berggren et al., 1995b
LO <i>Porticulasphaera semiinvoluta</i>		35.3	Berggren et al., 1995b
FO <i>Cribohantkenina inflata</i>		35.5	Berggren et al., 1995b
FO <i>Cribohantkenina inflata</i>		35.5	Berggren et al., 1995b
LO <i>Acarinina collactea</i>		37.7	Berggren et al., 1995b
LO <i>Subbotina linaperta</i>		37.7	Berggren et al., 1995b
LO <i>Morozovella spinulosa</i>		38.1	Berggren et al., 1995b
FO <i>Porticulasphaera semiinvoluta</i>	P15	38.4	Berggren et al., 1995b
LO <i>Planorotalites</i>		38.5	Berggren et al., 1995b
LO <i>Acarinina</i> spp.		37.5–38.5	Berggren et al., 1995b
LO <i>Acarinina primitiva</i>		39.0	Berggren et al., 1995b
LO <i>Subbotina frontosa</i>		39.3	Berggren et al., 1995b
LO <i>Globigerapsis beckmanni</i>	P14	40.1	Berggren et al., 1995b
FO <i>Globigerapsis beckmanni</i>	P13	40.5	Berggren et al., 1995b
LO <i>Acarinina bullbrooki</i>		40.5	Berggren et al., 1995b
FO <i>Turborotalia pomeroli</i>		42.4	Berggren et al., 1995b
FO <i>Globigerapsis index</i>		42.9	Berggren et al., 1995b
FO <i>Morozovella lehneri</i>		43.5	Berggren et al., 1995b
LO <i>Morozovella aragonensis</i>	P12	43.6	Berggren et al., 1995b
FO <i>Globigerapsis kugleri</i>	P11	45.8	Berggren et al., 1995b
FO <i>Turborotalia possagnoensis</i>		46.0	Berggren et al., 1995b
FO <i>Hantkenina nuttali</i>	P10	49.0	Berggren et al., 1995b

Notes: FO = first occurrence, LO = last occurrence. Source: 1 = Berggren et al. (1995a, 1995b), 2 = Chaisson and Pearson (1997), Pearson and Chaisson (1997), and Curry, Shackleton, Richter, et al. (1995). Sources: C&P97 = Chaisson and Pearson (1997), P&C97 = Pearson and Chaisson (1997), CSR95 = Curry, Shackleton, Richter, et al. (1995). Astrochronologically tuned biostratigraphic datums are shown in bold.

Table T6. Diatom datums, Leg 202.

Zonal boundary*	Event	CK95 GPTS age (Ma)	Chron	Reference
<i>P. doliolus/N. reinholdii</i>	LO <i>Nitzschia reinholdii</i>	0.62	C1n	Shackleton et al., 1995
A/B of <i>N. reinholdii</i>	LO <i>Rhizosolenia praebergonii</i> v. <i>robusta</i>	1.73	C1r	Shackleton et al., 1995
<i>N. reinholdii/N. marina</i>	FO <i>Fragilariopsis doliolus</i>	2.00	C2r.1r	Shackleton et al., 1995
A/B of <i>N. marina</i>	LO <i>Thalassiosira convexa</i> s.l.	2.41	C2n	Shackleton et al., 1995
<i>N. marina/N. jouseae</i>	LO <i>Nitzschia jouseae</i>	2.77	C2An.1n	Shackleton et al., 1995
<i>N. jouseae/T. convexa</i>	FO <i>Nitzschia jouseae</i>	5.12	C3n.4n	Shackleton et al., 1995
B/C of <i>T. convexa</i>	LO <i>Thalassiosira miocenica</i>	5.84		Shackleton et al., 1995
A/B of <i>T. convexa</i>	LO <i>Thalassiosira praeconvexa</i>	6.18	C3An.2n	Shackleton et al., 1995
<i>T. convexa/N. miocenica</i>	FO <i>Thalassiosira convexa</i> v. <i>aspinosa</i>	6.57	C3An.2n	Shackleton et al., 1995
A/B of <i>N. miocenica</i>	FO <i>Thalassiosira praeconvexa</i>	6.71	C3An.2n	Shackleton et al., 1995
<i>N. miocenica/N. porteri</i>	FO <i>Nitzschia miocenica</i> s.l.	7.30		Shackleton et al., 1995
A/B of <i>N. porteri</i>	LO <i>Thalassiosira burckliana</i>	7.85	C4n.2n	Shackleton et al., 1995
<i>N. porteri/T. yabei</i>	LO <i>Thalassiosira yabei</i>	8.23	C4r.1n	Shackleton et al., 1995
A/B of <i>T. yabei</i>	FO <i>Thalassiosira burckliana</i>	8.91	C4An	Shackleton et al., 1995
<i>T. yabei/A. moronensis</i>	LO <i>Actinocyclus moronensis</i>	9.76		Shackleton et al., 1995
<i>A. moronensis/C. coscinodiscus</i>	LO <i>Craspedodiscus coscinodiscus</i>	11.44		Shackleton et al., 1995
<i>C. coscinodiscus/C. gigas</i> v. <i>diorama</i>	LO <i>Actinocyclus ingens</i>	12.18		Shackleton et al., 1995
<i>C. gigas</i> v. <i>diorama/C. lewisianus</i>	LO <i>Coscinodiscus lewisianus</i>	12.93		Shackleton et al., 1995
<i>C. lewisianus/C. peplum</i>	LO <i>Cestodiscus peplum</i>	14.06	C5ACn	Shackleton et al., 1995
A/B of <i>C. peplum</i>	LO <i>Annellus californicus</i>	14.99		Shackleton et al., 1995
<i>C. peplum/C. nicobarica</i>	FO <i>Cestodiscus peplum</i>	16.37	C5Cn.1n	Shackleton et al., 1995
A/B of <i>C. nicobarica</i>	LO <i>Thalassiosira burkryi</i>	16.74	C5Cr	Barron, 1985; Barron, 1992
<i>C. nicobarica/T. pileus</i>	FO <i>Crucidentacula nicobarica</i> s.l.	17.77		Shackleton et al., 1995
<i>T. pileus/C. elegans</i>	LO <i>Craspedodiscus elegans</i>	18.41		Barron, 1985; Barron, 1992
<i>C. elegans/R. paleacea</i>	LO <i>Bogorovia veniamini</i>	19.59		Barron, 1985; Barron, 1992
B/C of <i>R. paleacea</i>	LO <i>Azpeitia oligocenica</i>	20.27		Barron, 1985; Barron, 1992
A/B of <i>R. paleacea</i>	LO <i>Thalassiosira primalabiate</i>	21.31		Barron, 1985; Barron, 1992
<i>R. paleacea/R. gelida</i>	FO <i>Rossiella paleacea</i>	22.64		Barron, 1985; Barron, 1992
<i>R. gelida/B. veniamini</i>	FO <i>Rocella gelida</i>	24.26		Barron, 1985
<i>B. veniamini /R. vigilans</i>	FO <i>Bogorovia veniamini</i>	25.60		Barron, 1985
A/B of <i>R. vigilans</i>	LO <i>Cestodiscus mukhiniae</i>	27.34		Barron, 1985
<i>R. vigilans/C. excavatus</i>	LO <i>Coscinodiscus excavatus</i>	31.91		Barron, 1985
bottom of <i>C. excavatus</i> Zone	FO <i>Coscinodiscus excavatus</i>	34.04		Barron, 1985

Notes: * = zonal schemes are based on those of Barron (1985a, 1985b) with modification of Baldauf and Iwai (1995). Bold type = major zonal limits. FO= first occurrence, LO = last occurrence. One exception is the zonal boundary datum of *Craspedodiscus coscinodiscus/Coscinodiscus gigas* v. *diorama* zones. We substituted the last common occurrence of *Actinocyclus ingens* for the FO of *Coscinodiscus temperei* v. *delicata* because the species is rare and sporadic. Age values were updated from the literature (Barron, 1985a, 1992; Shackleton et al., 1995) and given in the geomagnetic polarity timescale (GPTS) of Cande and Kent (1995).

Table T7. Techniques, standards, typical ratios of measured/expected values, and typical reproducibility for interstitial water geochemical analyses.

Analysis	Technique	Standard	Measured/expected range	Reproducibility (% rsd, 1 σ)
Alkalinity	AT	Sodium carbonate solutions	*	1–5
		IAPSO (low alkalinity sites)	—	—
Cl ⁻	T	IAPSO	†	Up to 0.5
SO ₄ ²⁻	IC	IAPSO	0.96–1.03	Up to 4
H ₄ SiO ₄	S	Solution, weighed	—	1–3
HPO ₄ ²⁻	S	Solution, weighed	—	Up to 4
NH ₄ ⁺	S	Solution, weighed	—	2–4
Na ⁺	IC (1 232), ICP-AES	IAPSO	0.96–1.02	Up to 3
Mg ²⁺	IC (1 232), ICP-AES	IAPSO	0.97–1.02	Up to 3
Ca ²⁺	IC (1 232), ICP-AES	IAPSO	0.95–1.02	Up to 3
K ⁺	IC (1 232), ICP-AES	IAPSO	0.95–1.04	Up to 3
Mn ²⁺	ICP-AES	Dilutions of reference solutions in acidified NaCl matrix	0.94–1.04	Up to 4
Fe ²⁺	ICP-AES	Dilutions of reference solutions in acidified NaCl matrix	0.97–1.11	Up to 4
B	ICP-AES	Dilutions of reference solutions in acidified NaCl matrix	0.95–1.04	Up to 4
Sr ²⁺	ICP-AES	Dilutions of reference solutions in acidified NaCl matrix	0.99–1.04	Up to 4
Ba ²⁺	ICP-AES	Dilutions of reference solutions in acidified NaCl matrix	0.96–1.02	Up to 4
Li ⁺	ICP-AES	Dilutions of reference solutions in acidified NaCl matrix	0.91–1.17	Up to 4

Notes: AT = autotitration, T = titration, IC = ion chromatography, S = spectrophotometry, ICP-AES = inductively coupled plasma–atomic emission spectrophotometry. rsd = relative standard deviation. IAPSO = International Association for the Physical Sciences of the Ocean. * = range 0.88–0.96 observed; samples corrected to IAPSO and/or other standards. — = no comparison made. † = calibrated directly to IAPSO standards.

Table T8. Calcium carbonate replicate analyses,
Sample 202-1236A-3H-3, 74–75 cm.

Replicate	CaCO ₃ (wt%)	Mean (wt%)	Standard deviation
1	95.84	95.78	0.15
2	95.70	—	—
3	95.78	—	—
4	95.75	—	—
5	96.08	—	—
6	95.85	—	—
7	95.74	—	—
8	95.68	—	—
9	95.49	—	—
10	95.86	—	—

Table T9. Measurements made by wireline tool strings.

Tool string	Tool*	Measurement	Sampling interval (cm)	Approximate vertical resolution (cm)
Triple combination	HNGS	Spectral gamma ray	15	51
	APS	Porosity	5 and 15	43
	HLDS/HLDT	Bulk density	2.5 and 15	38/46
	DIT	Resistivity	15	200/150/76
	TAP	Temperature	1 per s	NA
		Tool acceleration	4 per s	NA
		Pressure	1 per s	NA
		Gamma ray		15
MGT†				
Formation MicroScanner	NGT	Spectral gamma ray	15	
FMS-sonic combination	GPIT	Tool orientation	0.25 and 15	NA
	FMS	Microresistivity	0.25	0.5
	DSI/SDT/LSS/BHC	Acoustic velocity	15	107/120/61/61

Notes: All tool and tool string names (except the TAP and MGT tools) are trademarks of Schlumberger. For additional information about tool physics and use, consult ODP Logging Services at <http://www.ldeo.columbia.edu/BRG/ODP>. * = See Table T10, p. 76, for explanations of acronyms used to describe tool strings and tools. † = not included in each logging run. NA = not applicable.

Table T10. Acronyms and units used for wireline logging tools.

Tool	Output	Explanation	Unit
APS		Accelerator Porosity Sonde	
	APLC	Near array porosity (limestone calibrated)	%
	SIGF	Formation capture cross section (Σf)	Capture units
	STOF	Tool standoff (computed distance from borehole wall)	in
DIT		Dual Induction Tool	
	IDPH	Deep induction resistivity	Ωm
	IMPH	Medium induction resistivity	Ωm
	SFLU	Spherically focused resistivity	Ωm
DSI		Dipole Sonic Imager	
	DTCO	Compressional wave delay time (Δt)	ms/ft
	DTSM	Shear wave delay time (Δt)	ms/ft
	DTST	Stoneley wave delay time (Δt)	ms/ft
FMS		Formation MicroScanner	
	C1, C2	Orthogonal hole diameters	in
	P1AZ	Pad 1 azimuth	Degrees
		Spatially oriented resistivity images of borehole wall	
GPIT		General Purpose Inclinometer Tool	
	DEVI	Hole deviation	Degrees
	HAZI	Hole azimuth	Degrees
	F_x, F_y, F_z	Earth's magnetic field (three orthogonal components)	Degrees
	A_x, A_y, A_z	Acceleration (three orthogonal components)	m/s^2
HLDT		Hostile Environment Litho-density Sonde	
	RHOM	Bulk density	g/cm^3
	PEFL	Photoelectric effect	b/e-
	LCAL	Caliper (measure of borehole diameter)	in
	DRH	Bulk density correction	g/cm^3
HNGS		Hostile Environment Gamma Ray Sonde	
	HSGR	Standard (total) gamma ray	gAPI
	HCGR	Computed gamma ray (HSGR minus uranium contribution)	gAPI
	HFK	Potassium	wt%
	HTHO	Thorium	ppm
	HURA	Uranium	ppm
MGT		Multi-Sensor Spectral Gamma Ray Tool	
	GR	Total gamma ray	gAPI
NGT		Natural Gamma Ray Spectrometry Tool	
	SGR	Standard total gamma ray	gAPI
	CGR	Computed gamma ray (SGR minus uranium contribution)	gAPI
	POTA	Potassium	wt%
	THOR	Thorium	ppm
	URAN	Uranium	ppm
TAP		Temperature/Acceleration/Pressure Tool	$^{\circ}C, m/s^2, psi$

Note: gAPI = American Petroleum Institute gamma units.